Tohoku University
Graduate School of Engineering

Elucidation of Deposition Mechanisms of Cold-Gas-Dynamic-Sprayed MCrAlY Coatings Focused on Nano-Structure

(ナノ組織に着目したコールドガスダイナミックスプレー MCrAlY 皮膜の
付着メカニズム解明)

A dissertation submitted for the degree of Doctor of Philosophy (Engineering)

Department of Mechanical Systems and Design

by

Yuji ICHIKAWA

16th January 2007

CONTENTS

1 Introduction

1.1 Background

In recent years, the average temperatures of the Earth's atmosphere and oceans have rapidly been increasing. The average near-surface atmospheric temperature of Earth rose by 0.6 ± 0.2 °C in the 20th century [1-1]. Increasing global temperatures are expected to cause a broad range of changes. Sea levels are expected to rise due to thermal expansion of the ocean, in addition to melting of land ice. Amounts and patterns of precipitation will probably change. Prediction of global warming requires enormous amounts of calculation and there is some uncertainty. Therefore, many researchers endeavor to improve the accuracy of predictions. On the other hand, there are the contrary opinions that criticize the uncertainty. Even allowing for the uncertainty, however, the scale of the predicted influence and future risks are enormous. Therefore, measure to combat warming is a most important task of pressing urgency on a global scale.

The scientific consensus identifies greenhouse gases (GHGs) as the primary cause of the recent warming. GHGs are gaseous components of the atmosphere that contribute to the greenhouse effect. Some GHGs occur naturally in the atmosphere, while others result from human activities. Naturally occurring greenhouse gases include water vapor, carbon dioxide, methane, nitrous oxide, and ozone. Certain human activities add to the levels of most of these naturally occurring gases

The Kyoto Protocol of the United Nations Framework Convention on Climate Change (Kyoto Protocol) is an agreement made under the United Nations Framework Convention on Climate Change (UNFCCC) at the third session of the Conference of Parties (COP3) to the UNFCCC on 11th December 1997 in Kyoto, Japan. Countries that ratify this protocol commit to reduce their emissions of carbon dioxide and five other greenhouse gases, such as Dinitrogen monoxide (N_2O), Hydrofluorocarbon (HFCs), Perfluorocarbon (PFCs) and Sulfur Hexafluoride (SF6). The Kyoto Protocol is an agreement under which industrialized countries will reduce their collective emissions of greenhouse gases by 5.2% compared to the year 1990 (but note that, compared to the emissions levels that would be expected by 2010 without the Protocol, this target represents a 29% cut). Table 1-1 shows a comparison of estimates made in 1996 and 2001 of global warming potential over 100 years.

Table 1-1 Global warming potential comparison of 100-Year GWP estimates from the IPCC's second (1996) and Third (2001) assessment reports

Gas	1996 IPCC GWP [1-2]	2001 IPCC GWP [1-3]
Carbon dioxide (CO_2)	1	1
Methane (CH_4)	21	23
Dinitrogen monoxide (N_2O)	310	296
Hydrofluorocarbon (HFCs)		
HFC-23	11,700	12,000
HFC-125	2,800	3,400
HFC-134a	1,300	1,300
HFC-143a	3,800	4,300
HFC-152a	140	120
HFC-227ea	2,900	3,500
HFC-236fa	6,300	9,400
Perfluorocarbon (PFCs)		
Perfluoromethane (CF_4)	6,500	5,700
Perfluoroethane (C_2F_6)	9,200	11,900
Sulfur Hexafluoride (SF_6)	23,900	22,200

From the table, the global warming potential of CO_2 is much lower than that of the other GHGs. However, Fig.1-1 shows the trend in the amount of emission of GHGs. The GHGs emitted predominantly consist of CO_2. Since the Industrial Revolution, circa1800, the burning of fossil fuels has caused a dramatic increase of CO_2 in the atmosphere, reaching levels unprecedented in the last 400 thousand years. This increase has been implicated as a primary cause of global warming. A worldwide trend towards reduction in CO_2 emissions is an important measure against global warming.

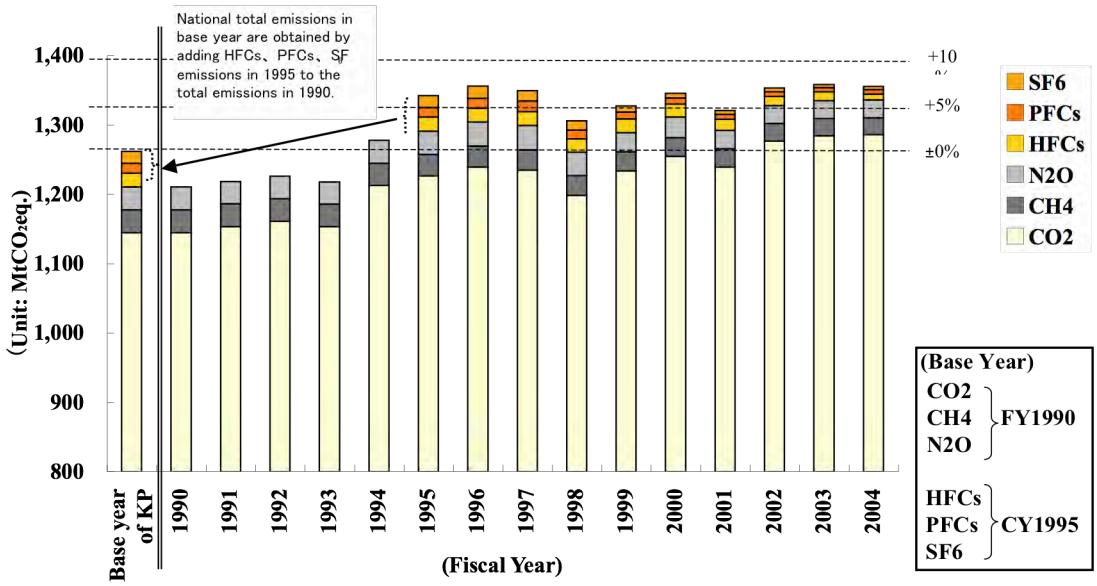

Fig.1-1 Trend in GHGs emissions [1-4].

The Kyoto protocol required certain conditions to be fulfilled before coming into force, such as being concluded by more than 55, and a total CO_2 emission to at least 55% of the CO_2 emissions in 1990 by UNFCCC Annex I parties. Annex I Parties include the industrialized countries that were members of the OECD (Organization for Economic Co-operation and Development) in 1992, plus countries with economies in transition (the EIT Parties), including the Russian Federation, the Baltic States, and several Central and Eastern European States. However, some industrialized countries, such as USA, the Russian Federation and Australia have not accepted the Kyoto protocol and it could not come into force for a few years from COP3. The agreement came into force on 16th February 2005 following ratification by Russia on 18th November 2004. As of December 2006, a total of 169 countries and other governmental entities have ratified the agreement (representing over 61.6% of emissions from Annex I countries). As a result, the reduction rate was decided based on emissions in 1990 in each advanced country, and those countries are obliged to accomplish the reduction in emissions. National targets range from 8% reductions for the European Union and some others to 7% for the US, 6% for Japan, 0% for Russia, and permitted increases of 8% for Australia and 10% for Iceland. However, the United States has not yet to sign the protocol.

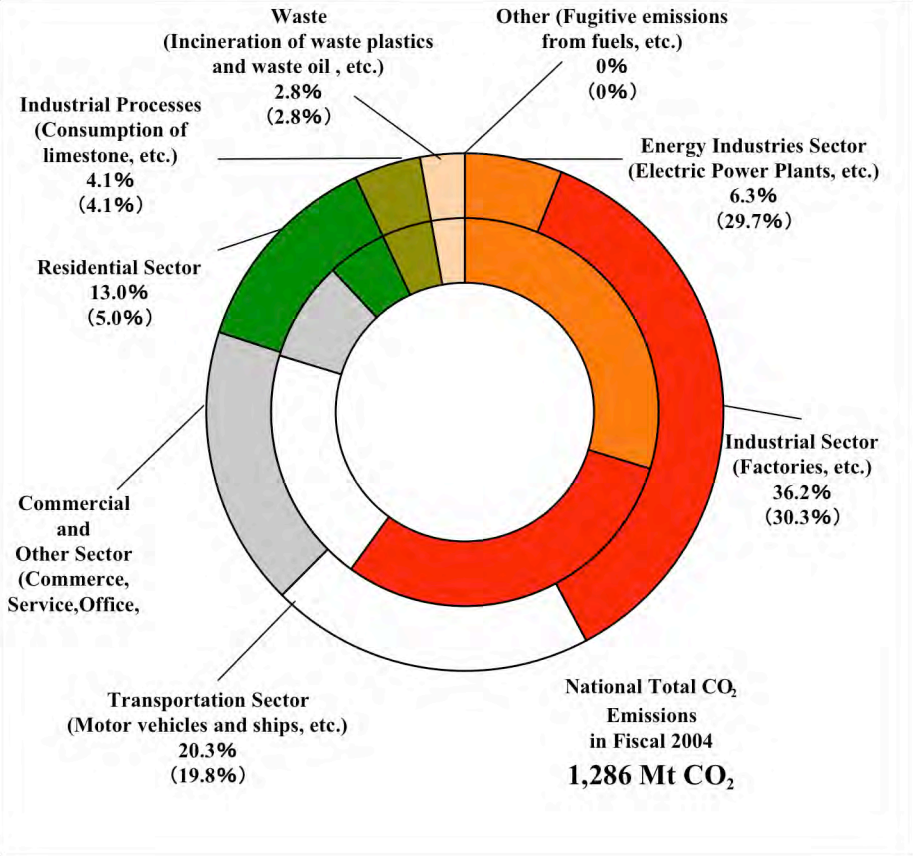

Fig. 1-2 *CO_2 emission in Japan (2004) [1-4] Inner circle graph: direct emissions, outer circle graph: indirect emissions. Indirect emissions: The proportion of the emissions from power generation by electric utilities.*

Figure 1-2 shows the CO_2 emission in Japan. One third of direct CO_2 emission was produced by electric power generation. Therefore, reduction of CO_2 emission reduction from electric power generation is very important. In particular, the thermal electric power generation exhausts most CO_2. The candidate measures for reduction of CO_2 emission from power generation are the improvement of efficiency, transition to nuclear power generation (nuclear power generation does not exhaust CO_2 directly), and the development and utilization of new power generation methods such as wind power, solar power, waste-to-energy and fuel cells. However, a sudden transition to nuclear power generation is difficult. Also, rapid development of new power generation methods is quite unlikely. Hence, thermal power generation will remain one of the most important power generation systems for some time in the future. Improvement of the efficiency of thermal generation plants is an important practical solution for the reduction of CO_2 emissions. The carbon based fossil energy sources such as oil, natural gas, and coal are reserves in the ground. There is a limit to the amount of fossil fuel. The number of years of production left in the ground, using the most optimistic reserve estimates, are 32 years for oil, 72 years for natural gas , and 252 years for coal. This estimate assumes that the product can be produced at a constant level for that number of years and that all of the reserves can be recovered. In fact,

consumption of all three resources has been increasing along with increase in the usage of energy. This suggests that the resources will be used up more quickly. Efficiency improvements of thermal power generation plants are urgently needed from the viewpoint of energy resource conservation.

From the viewpoints of energy resource conservation and CO_2 emission reduction, many heavy industries and researchers have been studying positive efforts to develop higher efficiency thermal power generators for a long period of time.

Figure 1-3 [1-5] shows the improvements in power generation efficiency of thermal power generation plants in Japan. Using regenerative cycle reheat turbines and high-capacity units enabled an increase in the power generation efficiency of steam turbines to 40 % since 1975. Since this period, however, the power generation efficiency has not drastically changed because of the restrictions imposed by the strength of the metallic material that is used for the boilers and the turbines in high temperature environments [1-6].

The next generation advanced gas turbine plants have some advantages. The advantages are as follows: (1) due to the use of liquefied natural gas (LNG), which has only a small carbon content for each unit calorie, CO_2 emission reduction is expected, (2) due to easy increase in the easer working gas temperature, an improvement in efficiency is expected, (3) the construction cost is less than that of nuclear power plant and conventional thermal power plant, (4) due to easier start-stop and the possibility of wide range load management, a flexible response to electricity demand is possible. Gas-turbine thermal power generation plants have drawn attention as one of the best power generation systems that can most flexibly respond to recent requirements for thermal power generation.

The turbine inlet gas temperature (TIT) of early gas turbines was approximately 800 ºC. The efficiency of these plants was lower than that of steam turbine generators. Subsequently, rising TIT has allowed higher efficiency and higher reliability with the development of high temperature materials, as shown in Fig. 1-4 [1-9]. Acceptance of combined cycle gas turbines promotes the worldwide development and the introduction of the gas turbines. Combined cycle gas turbines use high temperature heat waste, which is exhausted by the gas turbine as a heat source and operates a steam turbine. The use of combined cycle gas reduces the limitations of higher working temperature operation and also improves the efficiency. The most advanced 1500 ºC-class combined cycle gas turbine power generators have over 50 % thermal efficiency. Commercial operation began at the Tohoku Electric Power Co., Inc. Higashi-Niigata 4-2 thermal power generation plant in 1999 [1-7, 8].

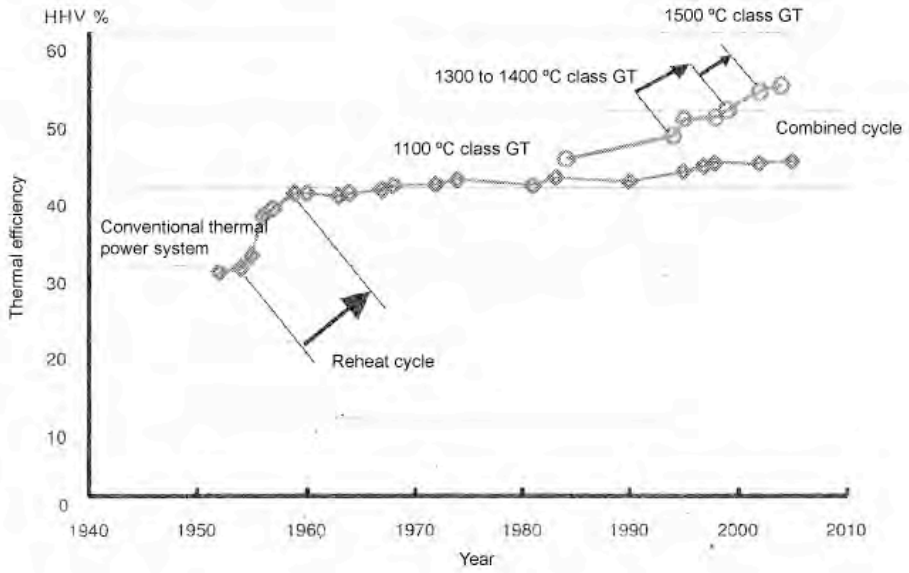

Fig. 1-3 Changes in power generation efficiency of thermal power generation plant [1-5].

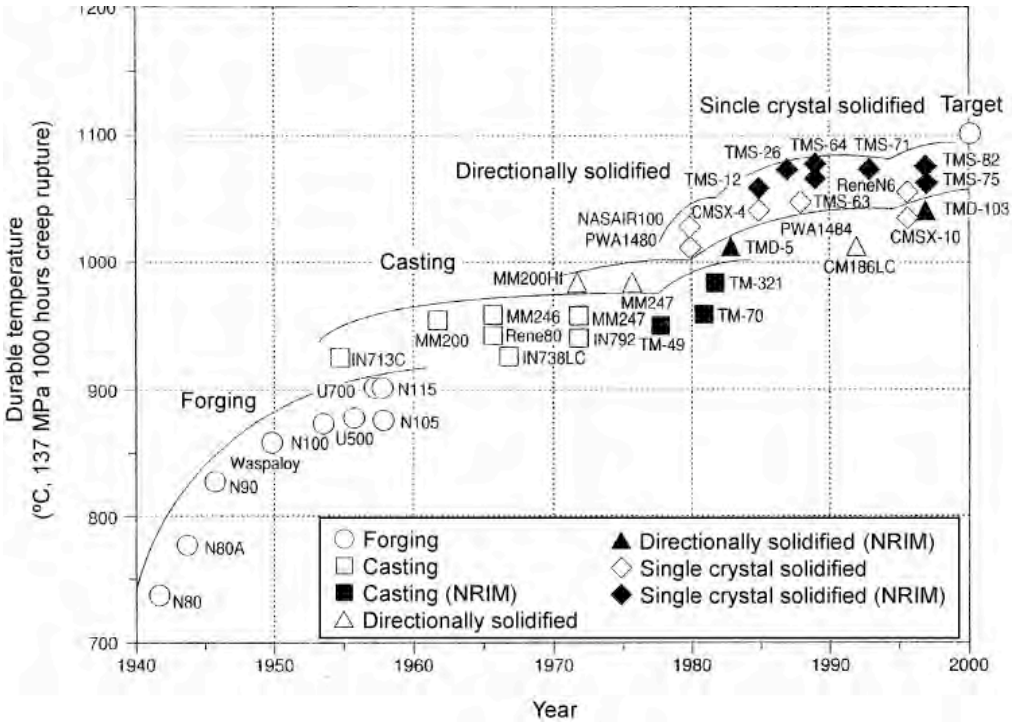

Fig. 1-4 Changes in temperature resistance of Ni-base superalloys [1-9].

1.2 MCrAlY Coatings for Turbine Blades

As mentioned above, over the past 20 to 30 years, improvement of alloys, such as directional solidification and single-crystal, have contributed significantly to the improvement of temperature resistance of blade materials. These improved materials have good mechanical properties in high temperature environments. However, these materials do not have a greatly improved corrosion resistance in high temperature environments. As a result, higher temperature environments induce severe high-temperature oxidation or corrosion problems, and to make things worse, the improvement in mechanical properties of the base alloys is obtained at the expense of environmental resistance. The first type of overlay coatings was therefore developed to palliate for the poor oxidation resistance of the base alloy (aluminide, Pt-aluminide, MCrAlY). Second types of coatings applied to high-temperature parts are known as thermal barrier coatings (TBC). These are ceramic coatings with very low thermal conductivity. Despite being typically several hundred μm thick, these coatings allow for a drop of 100-300 °C between the gas and metal surface temperatures. Such coatings are oxygen transparent and do not prevent oxidation of the underlying substrate. Therefore, TBC systems have a double-layered structure such as a ceramic thermal barrier coating and a MCrAlY bond coating for high temperature oxidation-corrosion resistance.

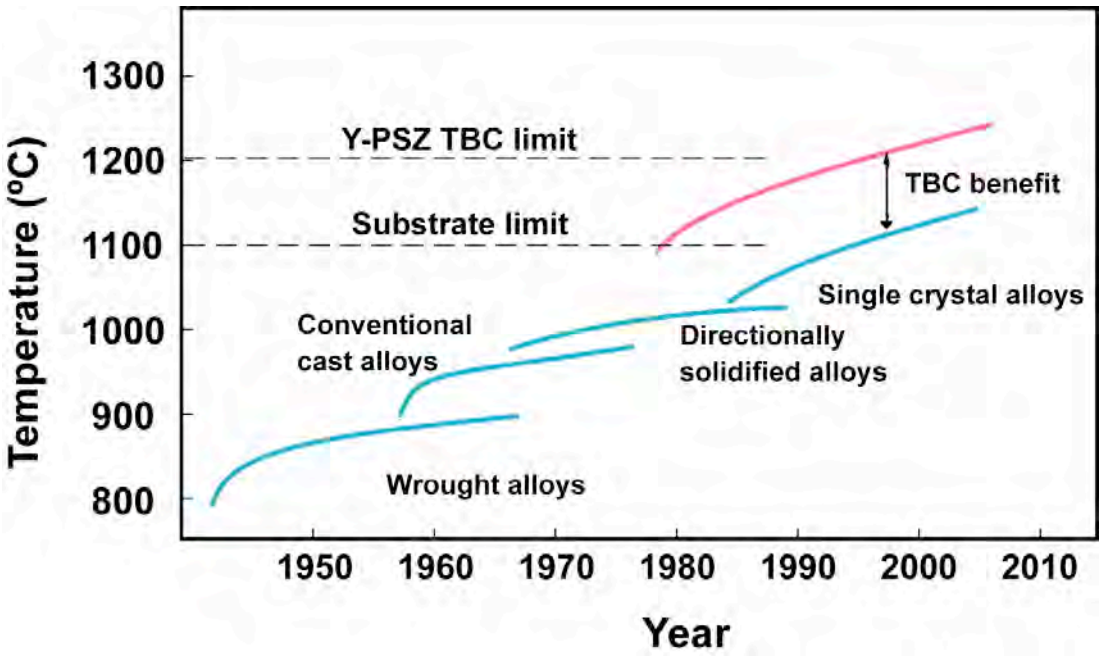

Fig. 1-5 Increase in operational temperature of turbine components [1-10].

Generally, the TBC coatings are deposited using the thermal spray technique. The top coat is obtained by atmospheric plasma spray (APS) or EB-PVD (electron beam physical vapor deposition) techniques. Bond coats were deposited by APS; however, this technique cannot prevent oxidation during the spraying process. Therefore, the low-pressure plasma spray (LPPS) technique has been developed and

applied to obtain bond coatings without oxidation. Recently, the high velocity oxygen fuel (HVOF) spray technique has been applied to produce bond coatings.

Recent generations of Ni base superalloys for single-crystal turbine blades contain relatively high percentages of refractory elements such as Ta, W or Re, which enhance the high-temperature mechanical properties. This is made possible by the removal of Cr and Al. Given the severe environmental conditions in which the blades operate, the removal of these elements (beneficial for oxidation resistance) implies even greater degradation problems. To palliate for this lack of appropriate oxidation and corrosion resistance, overlay coatings are applied to the blades. The purpose of these is to allow the growth of a protective oxide film. Especially, α- Al_2O_3 have excellent protection properties and low growth rates. The composition of the coatings must therefore be chosen carefully so as to ensure growth of α- Al_2O_3. The two most widely used coatings are aluminides (NiAl or Ni_2Al_3) and MCrAlY coatings. The former are obtained by surface enrichment by diffusion, the latter by plasma spray or EBPVD.

MCrAlY coatings typically consist of a two-phase microstructure $\beta+\gamma$. The presence of γ increases the ductility of the coating, thereby improving thermal fatigue resistance. As regards β -NiAl coatings, high temperature exposure results in depletion of the Al both to the TGO (thermally grown oxide) and to the substrate by inter-diffusion as shown in Fig. 1-6. As the amount of Al decreases, the β phase tends to dissolve. For this reason, it is often described as an aluminum reservoir, and coating life is often measured in terms of depletion of β -NiAl phase (Fig. 1-7).

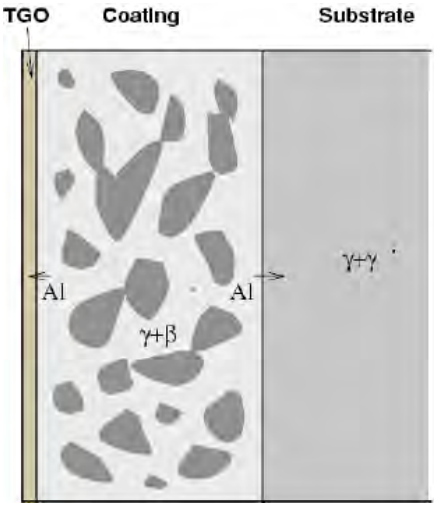

Fig. 1-6 Schematic illustration of MCrAlY coating microstructure.

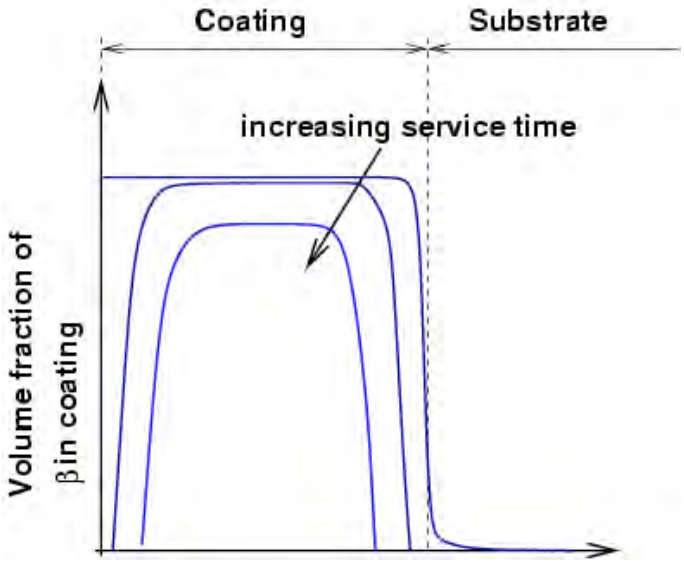

Fig. 1-7 Al diffusion to the oxide layer and the substrate result in depletion of beta from both sides.

The M of MCrAlY stands for either Ni or Co, or a combination of both. Co-based alloys appear to have superior resistance to corrosion, but Ni-base alloys have good ductility. The chemical composition of the base metal is selected to optimize the high temperature corrosion behavior and ductility (Fig. 1-8). Cr and Al provide protective oxide films. In high temperature environments, Al forms a Al_2O_3 protective oxide film, but Al has poor sulfuration resistance. Hence, Cr, providing hot-corrosion resistance, is required. MCrAlY also typically contains 0.1 to 1 wt% yttrium (Y), which enhances the adherence of the oxide film. It was initially thought that yttrium helped the formation of oxide pegs, which helped anchor the oxide layer to the coating. Additions of hafnium (Hf) play a similar role to Y. The effect of other additions has also been investigated by Nicoll et al. [1-13]. It was found that silicon (Si) significantly improved cyclic oxidation resistance. However, it also decreases the melting point of the coating. 5 wt.% addition is enough to lower the melting temperature to about 1140 $^{\circ}$C. There is also evidence that it affects phase stability. For cyclic oxidation at 1000 $^{\circ}$C, 2.5 wt.% was found to be the optimum content. Additions of rhenium (Re) have been shown to improve isothermal or cyclic oxidation resistance, and thermal cycle fatigue was reported by Czech et al [1-14]. Additions of tantalum (Ta) can also increase the oxidation resistance.

Excessive addition of Al, Cr, Y or infinitesimal additional elements induces a reduction in ductility. Therefore it is important to determine the optimum amount of these elements to be added. The chemical composition of MCrAlY alloy was chosen by consideration of high temperature oxidation, hot corrosion, matching with substrate material and ductility. M-$Cr_{15\text{-}30}$-$Al_{5\text{-}16}$-$Y_{0.1\text{-}1}$ (subscript number indicating wt% of the element) is a representative composition.

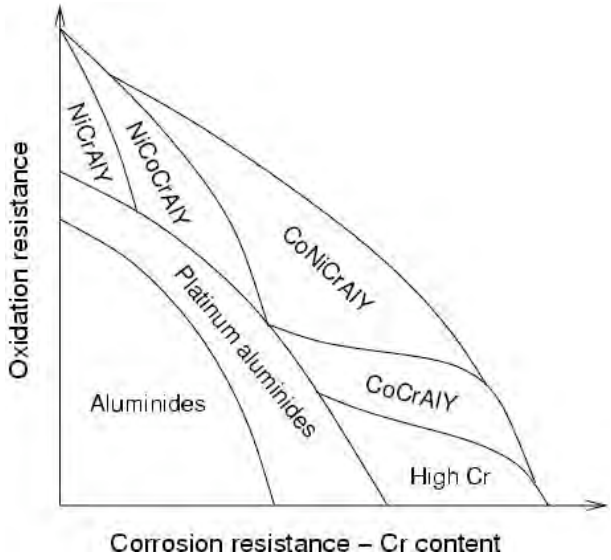

Fig. 1-8 Optimum coating composition in relation to oxidation and hot-corrosion [1-15].

1.3 Thermal Spray

Thermal spraying is a surface modification technique that consists of melting a material and projecting it as molten particles onto the substrate to deposit a coating.

In 1909, Schoop developed the origin of thermal spraying. The history of thermal spraying is indicated in Table 1-2. Currently used thermal spray techniques are categorized by heat sources and materials in Fig. 1-9. This figure shows the major methods and examples are drawn reference [1-18].

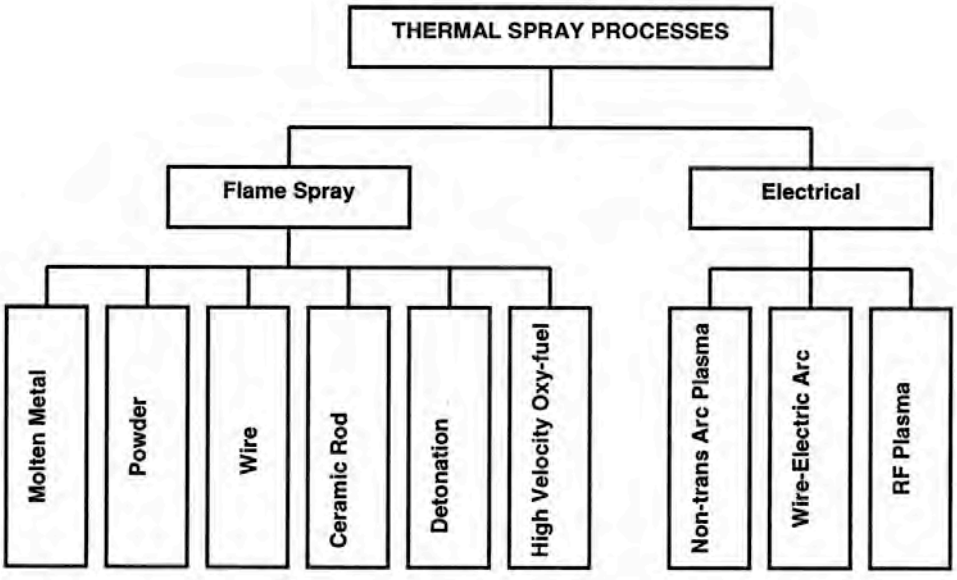

Fig. 1-9 Thermal spray application methods by heat source schematic [1-18].

Table 1-2 History of thermal spray

1909	Dr.M.U.Schoop developed the thermal spray technique and apply of a patent
1914	Dr.M.U.Schoop developed arc spray
1937	Schorit ype powder thermal spray gun was developed
After WW II	Self-fluxing alloy was developed
1950	Meteco (Powder type), Norton (Lod type) succeed at Ceramics flame spray
1952	Linde Air Products developed the detonation spray
1957	Union Carbide (USA) apply for the patent of plasma spray gun
1970	Prof. Fukuda developed wire explosion spray
1973	E. Muehlber announced low pressure plasmas spray at 7th ITSC
1982	J.A.Browning developed (HVOF) Jet Kote
1989	Meteco developed (HVOF) DJ gun
1989	J.A.Browning developed (Hig pressure type HVOF) J gun
1991	J.A.Browning developed (HVAF) Aero jet gun
1994	Northwest Mettech developed axial injection plasma spray system
1994	A.P.Alkimovet al. developed Cold Spayand and patnent endorsed in USA

Thermal spraying processes can be divided into three parts, i.e. 1) pretreatment (degreasing of substrate surface, surface roughing and removing the oxide film by shot blasting), 2) spraying and 3) after-treatment (heat treatment, machining). Thermal spray techniques allow the use of a wide range of materials: metals, ceramics, plastics, glass etc. Hence, the thermal spray technique is capable of wide applications such as corrosion resistance, heat resistance, abrasion resistance, overlay and maintenance. The optimal spray technique and material are chosen from a variety of techniques and materials. Figures 1-10 to 14 show schematic illustrations of various types of thermal spraying. In each case of thermal spraying, the principle of deposition is that molten material is injected from a nozzle and impinges on

the substrate, developing the coating. In many cases, the acceleration gases selected are air, or inert gases such as nitrogen, argon or helium.

An outline of plasma spraying is shown in Fig. 1-14. The plasma spraying process involves the latent heat of an ionized inert gas "Plasma" being used to provide the heat source. A plasma is an ionized gaseous cloud composed of free electrons, positive ions, neutral atoms and molecules. Plasma is generated whenever sufficient energy is imparted to a gas to cause some of it to ionize. Ar, He, H_2, N_2 or a mixture of these gases is used to create the plasma. Gas flows between the electrode and nozzle. A high frequency or high voltage alternating electric arc is struck between the nozzle and the electrode, which ionizes the gas stream. This has the effect of increasing the power and the velocity of gas stream, due to the expansion of the gas. Once the appropriate gas stream has been established for the material being sprayed, the feed stocked material is fed into the gas stream and the molten material impinging on the substrate deposits the coating. This technique is classified by working environment, namely APS, LPPS etc. Because the APS involves deposition in an atmospheric environment, oxidation cannot be prevented. The LPPS involves deposition under low pressure (2 to 30 kPa) and inert gas environments. Accordingly, it is possible to prevent the oxidation problem during the spray process and obtain dense metallic coatings [1-17]. Thermal spraying is a process of molten material impingement. Therefore, processes occurring due to the influence of heating, such as residual stress caused by the different thermal expansion ratio, cannot be prevented. Therefore, it is hoped that a surface modification technique can be developed which solves the problem of thermal influence during the coating process.

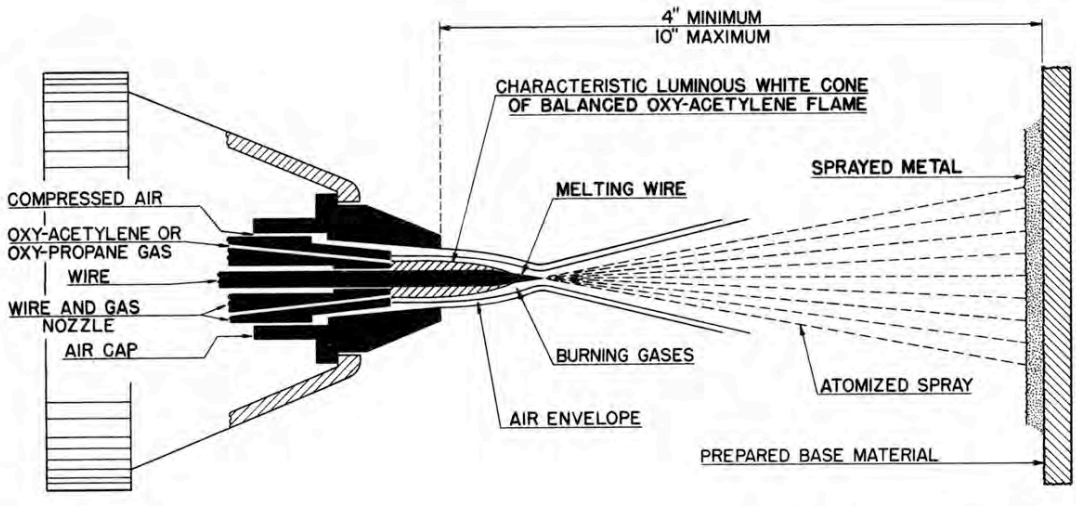

Fig. 1-10 Wire flame-spray [1-19].

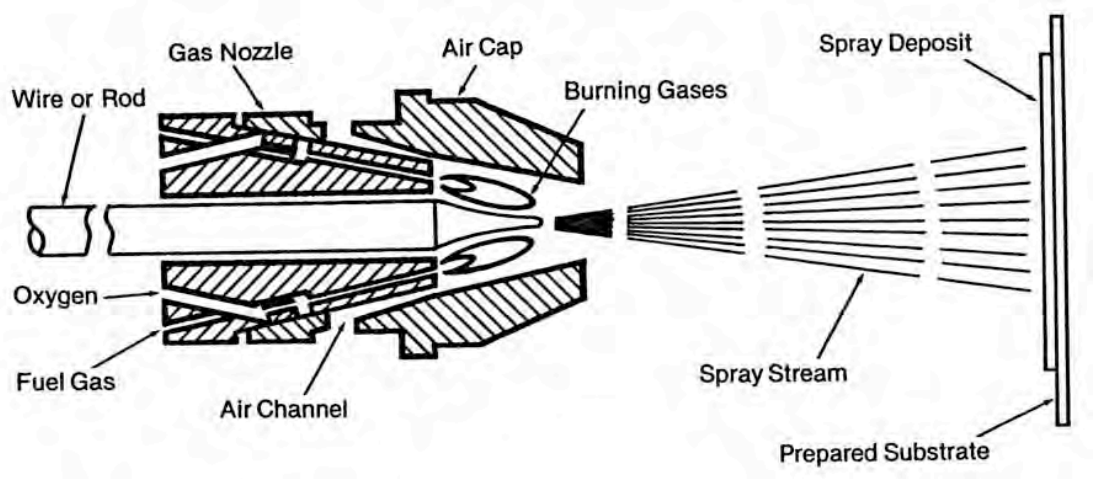

Fig. 1-11 Ceramic Rod, flame spray gun [1-20].

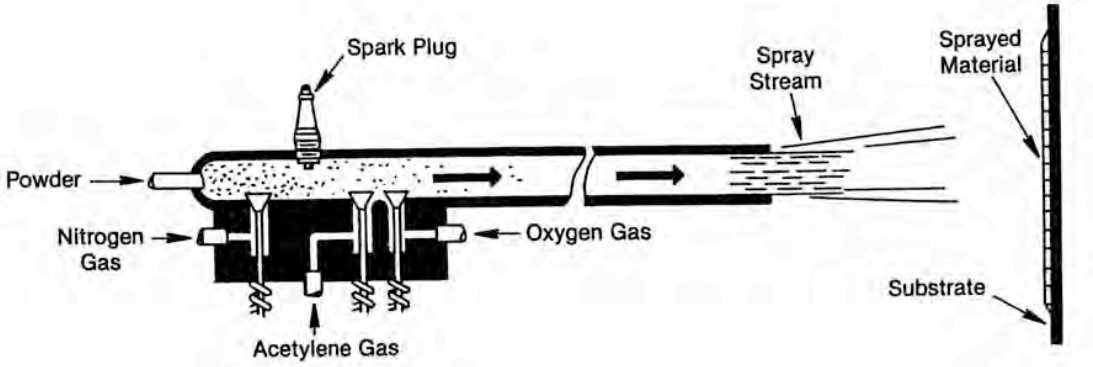

Fig. 1-12 Cross-section view of a detonation gun [1-20]

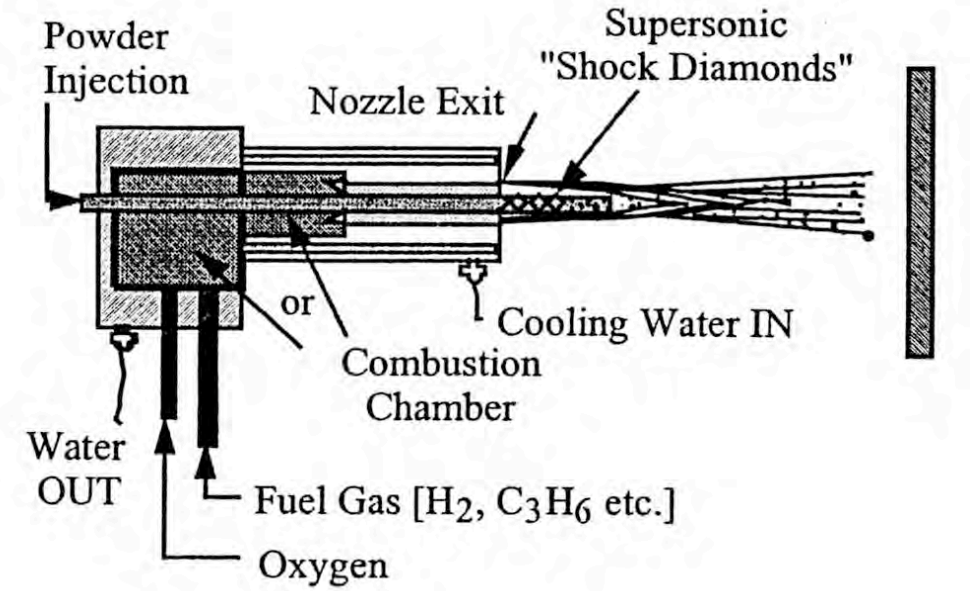

Fig. 1-13 HVOF combustion spray [1-20].

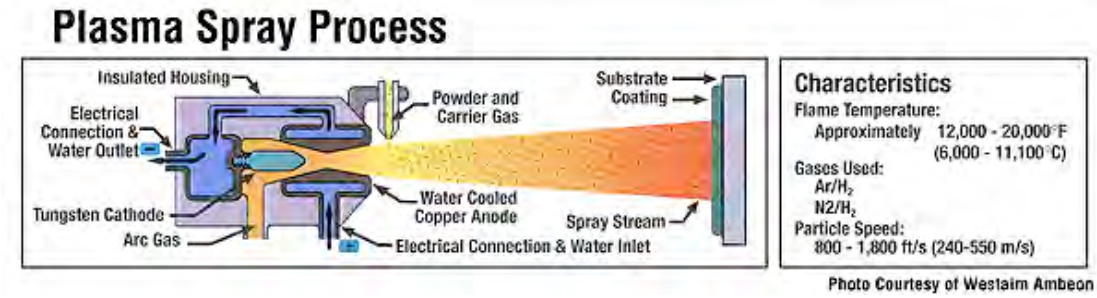

Fig. 1-14 Plasma spray [1-20].

1.4 Cold Spray

The cold gas dynamic spray technique, for brevity called "cold spray", a new coating technology, was initially developed by Alkimov, Papyrin et al. in the mid-1980s at the Institute for Theoretical and Applied Mechanics of the Siberian Division of the Russian Academy of Science in Novosibirsk [1-21 to 26]. When they performed wind tunnel experiments using particles, they observed particle deposition and conceived the cold spray principle to watch it [1-27]. They reported that the most important factor in the cold spray process is a critical velocity [1-22]. The critical velocity determines whether deposition of the particle or erosion of the substrate occurs on impact of a spray particle. For a given material, there generally exists a critical particle velocity resulting in a transition from erosion of the substrate to deposition of particle. This report described the impact of iron, copper, nickel and aluminum particles on a copper substrate and determined that the deposition transition velocity was over 550-600 m/s. When the copper particle velocity was approximately 800 m/s, the deposition efficiency was more than 70 %. Alkimov, Papyrin et al. applied for a patent for the fundamental principles of cold spray, and the Union of Soviet Socialist Republics accepted the patent in 1990 [1-23], the United States in 1994 [1-24, 25], and the European Union in 1995 [1-26]. The claims of Papryin's patent [1-22, 24] are the following:

1. *A gas-dynamic spraying method for applying a coating to an article, the method comprising: introducing into a gas particles of a powder of at least one first material selected from the group consisting of a metal, alloy, polymer and mechanical mixture of a metal and an alloy, the particles having a particle size of from about 1 to 50 μm; forming the gas and particles into a supersonic jet having a temperature sufficiently low to prevent thermal softening of the first material and a velocity of from about 300 to about 1200 m/sec.; and directing the jet against an article of a second material selected from the group consisting of a metal, alloy and dielectric, thereby coating the article with the particles.*
2. *The method of claim 1, wherein the gas is selected from the group consisting of air, helium and a mixture of air and helium.*
3. *The method of claim 1, wherein the temperature of the jet is room temperature, the gas is air, the first material is aluminum and zinc and a flow rate of the particles in the jet is at least 0.05 g/sec. cm^2.*

4. *The method of claim 1, wherein the temperature of the jet is from about 30 ° C to about 400 ℃.*
5. *The method of claim 2, wherein the temperature of the jet is from about 30 ° C to about 400 ℃.*
6. *The method of claim 1, wherein forming the jet comprises forming the jet with a cross section having one maximum dimension bigger than a perpendicular maximum dimension.*

The most important feature of the cold spraying process is that a solid-state material impacts on the substrate and makes a deposit, and hence this process allows the influence of heating to be avoided. The setup of a cold spray system is simple, as shown in Fig. 1-15. It is possible to use many kinds of materials for cold spraying. These include Zn, Sn, Ag, Cu, Al, Ti, Nb, Mo, NiCr, Cu-Al, nickel alloys and MCrAlYs, polymers, blends of >50 vol.% ductile materials with brittle metals or ceramics, etc.

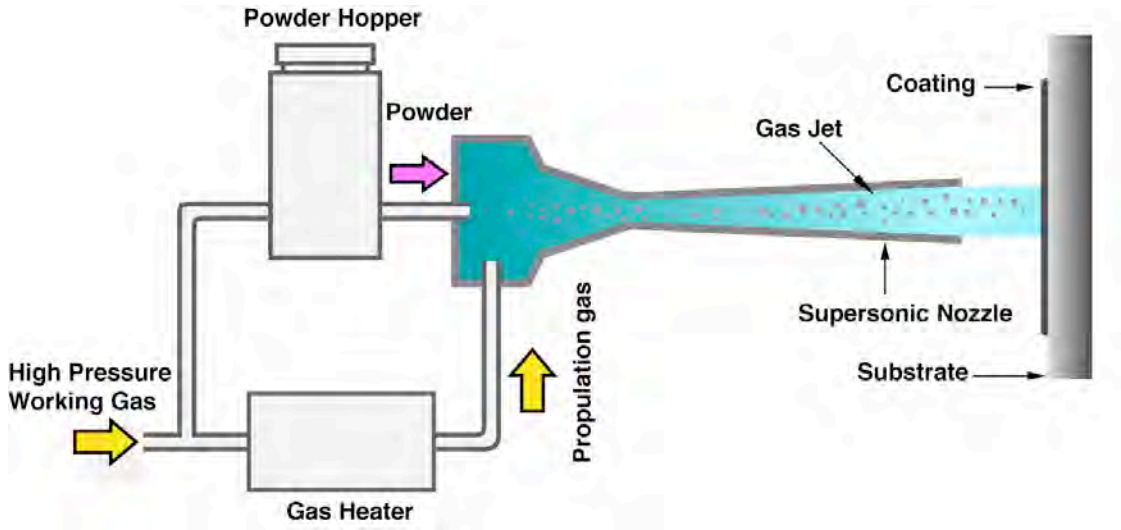

Fig. 1-15 Schematic illustration of cold spray system.

Generally, propellant gases are selected from helium, nitrogen or air. In particular, helium, which has a large gas constant, is able to attain a higher gas velocity than argon or air. However, the cost of helium is much more higher than that of the others. Therefore, the development of a helium recycling system is currently attracting attention from industries and many researchers.

When metallic coatings are produced using the conventional plasma spray technique, in order to prevent the oxidation, the spray should be performed in low pressure or an inert environment using LPPS technique. LPPS facilities require a vacuum chamber, which necessitates large equipment and time for attainment of the vacuum. The cold spray technique allows the production of metallic coatings in an atmospheric environment, and hence a reduction in cost. Moreover, since the cold-sprayed coating has compressive residual stress, it is possible to make coatings of thicknesses from a few μm to several

dozen mm. It is expected that the process can be used in molding applications. The characteristics of the cold spray technique can be summarized as follows:

[Advantages]

- Avoids phase transformation of materials
- Possible to gather non-deposited particles and to reuse them
- Possible to reduce the heating effect on the substrate
- Short working distance allows fine pattern construction.
- Simple equipment

[Disadvantage]

- Requires a large amount of gases
- Short lifetime of the facility due to abrasive wear problems in the facility.

1.5 Research Trends in Cold Spraying

The numbers of presentations on cold spraying at the International Thermal Spray Conference (ITSC) are shown in Fig. 1-16. At the ITSC 2000 in Montreal, a cold spray session was offered for the first time. Since 2000, the number of presentations and articles have increased with fluctuations depending on the venue for the conference. In 2000, the two companies Ktech (USA) [1-28] and CGT – Cold Gas Technology GmbH (Germany [1-29 to 31], commercialized a cold spraying system. This is one of the reasons for the attraction of cold spraying. Thus, the cold spraying was originally developed in Russia, but subsequently the USA and Germany have been at the head of the cold spray research and development. Recently, many countries, such as France, Australia, Canada, China, Korea and Japan etc., have become interested in the cold spray technique. The scale and popularity of research on this technique has been increasing every year.

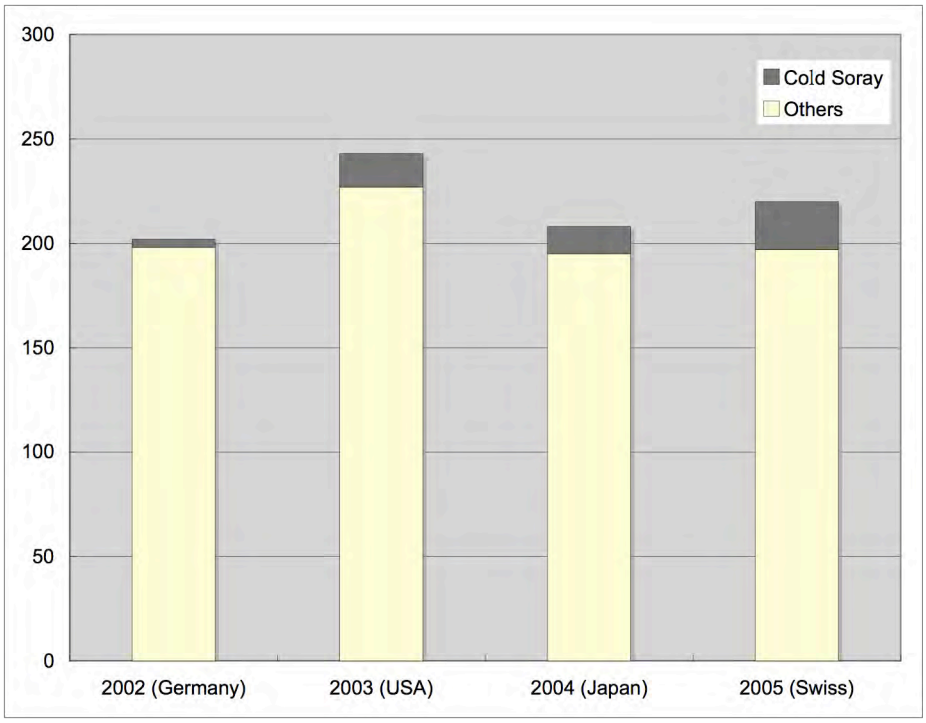

Fig. 1-16 Transition of presentation number and cold spray presentation number of International Thermal Spray Conference.

1.6 Knowledge of Deposition Mechanisms of Cold Spray

The deposition mechanisms of cold spraying are not completely understood. Summarizing the knowledge obtained from present research results, it is possible to consider the cold spray process as divided into the following three processes:

1. Process of particle acceleration by working gas
2. Process of deformation by particle impingement
3. Process of deposition.

In order to elucidate the deposition mechanism, this study has focused on the "particle impingement", "deformation process" and "particle deposition and coating process". One of the most important mechanisms is the critical velocity as described previously. Smith et al. have reported that the following factors have an effect on the critical velocity [1-34, 35].

1. Density and elastic modulus of particle and substrate
2. Strength, ductility and hardness of particle and substrate

3. Oxide film formation behavior and adhesion strength between oxide film and them
4. Particle size
5. Pretreatment of substrate

Figure 1-17 shows the results of FEM simulation of an aluminum particle impinging on a copper substrate as reported by Grujicica et al. [1-36]. The simulation results are for the collision between a single 20 mm-diameter aluminum particle with an incident velocity of 650 m/s and a flat semi-infinite copper substrate at four times (5, 20, 35 and 50 ns) following the initial particle/substrate contact. The results displayed in Fig. 1-17 (a)–(d) show that as the particle/substrate contact time increases, the particle (height-to-width) aspect ratio decreases while the substrate-crater depth and width increase. At the same time, a material jet, such as an enormous plastic deformed zone composed of both the particle material and the substrate material, is formed at the particle/substrate contact surface, therewithal the temperature increased. When this material jet reaches the free surface, it forms a lip, which points away from the flattened particle. The free surfaces contact and high pressure causes strong adhesion between substrate and particles [1-34, 35]. These mechanisms may be considered to be similar to those in the explosion bonding method [1-38].

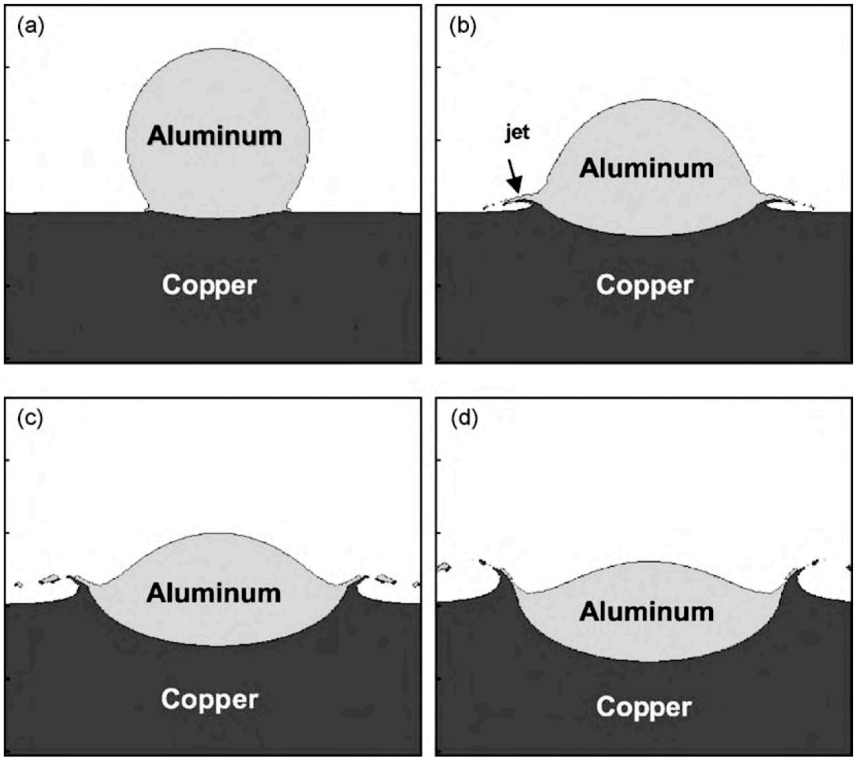

Fig. 1-17 Example of particle impact and material jet, 20 mm-diameter aluminum particle with the incident velocity of 650 m/s and a flat semi-infinite copper substrate at four times a) 5 ns, b) 20 ns, c) 35 ns and d) 50 ns, following the initial particle/substrate contact [1-36].

One interesting interpretation of the critical velocity has been reported by Assadi et al. [1-39]. They have tried to understand the critical velocity and bonding mechanism by experimental and computational approaches. When plastic deformation of the particle and substrate occurs, high-speed friction causes shear stress and an increase in temperature. They consider that the bonding phenomena were caused by a local increase in temperature above the melting point. Their experimental and computational results are summarized in the equation:

$$V_{critical} = 667 - 14\rho_P + 0.08T_{MP} + 0.1\sigma_u - 0.4T_{pi} \quad (1\text{-}1)$$

ρ_p: Density of particle (g/cm^3)

T_{MP}: Melting point of particle (ºC)

σ_u: Ultimate strength of particle (MPa)

T_{pi}: Initial temperature (ºC)

Recent cold spray apparatus has been equipped with gas heating systems, because a higher gas temperature allows the gas velocity to be increased. From Eq. (1-1), a higher initial temperature decreases the critical velocity, and hence higher-temperature operation improves the deposition efficiency. Against this background, increasing the working temperature is the latest research trend.

Vlceket al [1-40] carried out experiments in which Al, Cu and 316 stainless steel particle collided into mirror polished Al alloy and steel substrates, and theoretically calculated the contact pressure. From the results of these experiments, the product of particle weight and impingement velocity, in other words the impulse, is the key parameter of the deposition. When the impulse is not sufficient, the particle sticks out of the substrate. Therefore, when using a low-density material such as Al, in order to obtain enough impulse, the critical velocity should be higher than that for heavy materials. In addition, they determined combinations of particle and substrate leading to easy deposition. These combinations were affected by the hardness of materials. When the substrate hardness was similar or less than that of the particle, impact energy was absorbed and deposition was difficult.

Papryin et al. suggested that the deposition/abrasive threshold was determined by the relationships between the magnitudes of elastic energy (E_{EL}) and adhesion energy (E_{ad}). If $E_{EL} < E_{ad}$, the particle can be deposited. On the other hand, if $E_{EL} > E_{ad}$, the particle cannot be deposited.

In the case of spraying copper particles under low-pressure and low-temperature conditions (3MPa, 200ºC) on a steel substrate, a rough substrate can give a good deposition. On the other hand, with a polished substrate, depositions cannot be obtained. Sakaki et al. [1-41] reported that the dominant factor for adhesion under these spraying conditions was a mechanical anchor effect.

Many researchers have suggested many interpretations of the critical velocity and bonding mechanisms. However, these are not completely understood yet.

Moreover, the cold spray deposition is controlled not only by a single isolated factor, but by multiple factors, such as impact velocity, gas temperature, material system etc. Therefore, understanding of the cold spray deposition mechanisms allow improvement of the deposition efficiency and quality of the spray deposits.

1.7 Aim of Research Work

The final goal of this research is to obtain commercially viable to cold-sprayed MCrAlY coatings for land-based gas turbine applications. Recently, the production of MCrAlY coating deposited by the cold spray process has been demonstrated [1-42, 43]. Both works are in the early stages; they do not mention the cold spray deposition mechanism for MCrAlY coatings or high-temperature performances. Therefore, focusing on the nano-structure of the cold-sprayed coating, this research work elucidates the deposition mechanism of cold-sprayed MCrAlY coatings. The results of this work contribute to the commercial viability of cold-sprayed MCrAlY coating.

Figure 1-18 shows the constitution flow chart of this thesis. This thesis consists of 8 chapters in total. Chapter 1 describes the introduction of this work. Chapter 2 deals with the MCrAlY cold spraying procedure. Chapter 3 studies the mechanical properties and high-temperature oxidation behavior of cold spraying. Chapters 4 to 7 discuss the cold spray deposition mechanisms from two different approaches; one is the experimental approach in 4 and 5, and the other is simulation experiments and a computational approach in chapters 6 and 7. Chapter 4 focuses on the interface between an individual particle and the substrate. Chapter 5 describes high-magnification observations carried out using transmission electric microscopy. Chapter 6 reports experiments performed using the LASER-FLEX, which used laser shock accelerated MCrAlY foil to impact on the substrate and simulate the deposition phenomenon. Chapter 7 describes FEM simulations of cold spray impact and summarizes the deposition mechanism of cold-sprayed MCrAlY coating. Chapter 8 gives the final conclusions of this thesis.

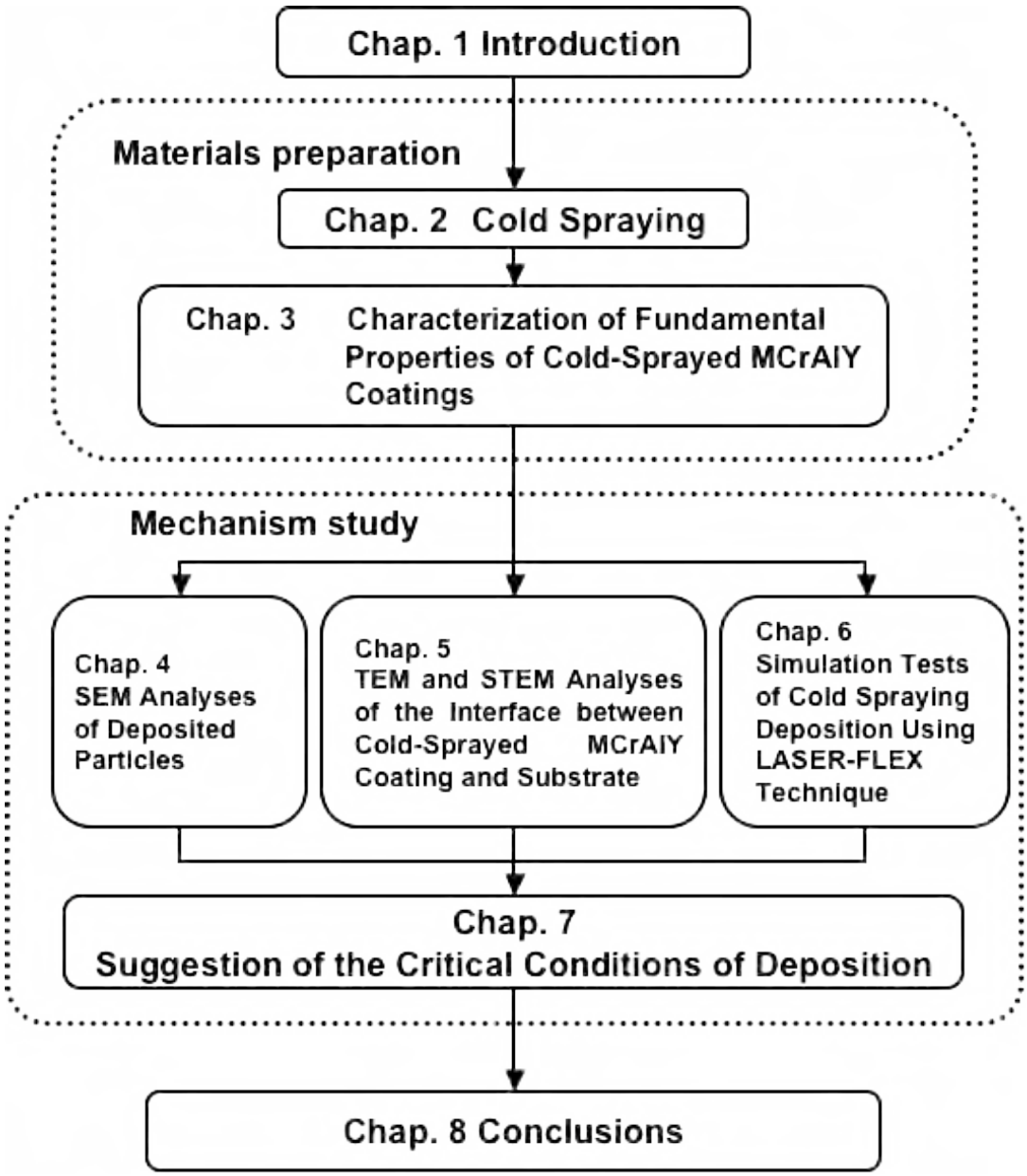

Fig. 1-18 Flow chart of the organization of this thesis.

References

[1-1] J.T. Houghton et all.: Climate Change 2001: The Scientific Basis of the most comprehensive and up-to-date scientific assessment of past, present and future climate change. The report assessment of the IPCC (Intergovernmental Panel on Climate Change)

[1-2] Intergovernmental Panel on Climate Change, Climate Change 1995: The Science of Climate Change (Cambridge, UK: Cambridge University Press, 1996).

[1-3] Intergovernmental Panel on Climate Change, Climate Change 2001: The Scientific Basis (Cambridge, UK: Cambridge University Press, 2001)

[1-4] Greenhouse Gas Inventory Office of Japan, "The GHGs Emissions Data of Japan (2004)"). (website; http://www-gio.nies.go.jp/index.html)

[1-5] Y. Fukushima, K. Kitayama, M. Machida, M. Yamazaki, T. Hori, H. Hosoi, T. Suto, and T. Kimura: Gas Turbine, The Thermal and Nuclear Power, 54 (10) (2003) pp. 1176-1197. (in Japanese)

[1-6] S. Miyake: Journal of Gas Turbine society of Japan, 25(97) (1997) pp. 47-51. (in Japanese)

[1-7] T. Mimaki: Introduction, The Thermal and Nuclear Power, 54 (10) (2003) pp.1118-1138. (in Japanese)

[1-8] Y. Fukushima, H. Sionari, H. Arimura, and R. Umagoe: "Latest Technology Development of Large Frame Gas Turbine", Mitsubishi Heavy Industries, Ltd. Technical Review, 40 (4) (2003) pp.194-199. (in Japanese)

[1-9] H Harada: Development of high heat-resistance superalloy for highly effective gas turbine Engineering material, 46 (7) (1998) pp.114-117. (in Japanese)

[1-10] Schulz et al, Aero. Sci. Techn. 7 (2003) p73-80.

[1-11] F.S. Pettit and G. W. Goward, Coatings for High Temperature Applications, Applied Science Publishers, 1983

[1-12] Smeggil J. L.: Some comments on the role of yttrium in protective oxide scale adherence, Mater. Sci. Eng., 87 (1987) pp.261-265.

[1-13] Nicoll A. R. et al: The effect of alloying additions on M-Cr-Al-Y systems - An experimental study Thin Solid Films, 95 (1992) pp.21-34.

[1-14] Czech et al.: Improvement of MCrAlY coatings by additions of rhenium, Surf. Coat. Techn., 68 (1994) pp.17-21.

[1-15] M. Schütze, Corrosion and Environmental Degradation Vol. II, Wiley-VCH, 2000

[1-16] Richard C. S. et al.: The influences of heat-treatments and interdiffusion on the adhesion of plasma-sprayed NiCrAlY coatings, Surf. Coat. Techn., 82 (1996) pp. 99-109.

[1-17] A. Hasui: "Yo-sha Kogaku (Thermal Spray Technology)" Sanpo publications, (1996), pp.48-49. (in Japanese)

[1-18] B: W. E. Ballard, Metal Spraying and the Flame Deposition of Ceramics and Plastics, Fourth Revised, Edition, 1963, Charles Griffin and Company Limited, London, England

[1-19] Flame Spray Handbook, Vol. 1 Wire Process, "Wire Nozzle and Air Cap Cross Section - METCO Metallizing Gun", page A-64, copyright 1969 located in International Thermal Spray Association Historical Collection

[1-20] Frank J. Hermanek, Thermal Spray Terminology and Company Origins, First Printing, 2001, ASM International, Materials Park, OH

[1-21] K. Sakaki: "New thermal spray process, Cold Spray: Yosha-gijutsu, 20 (3) (2002) pp. 32-41. (in Japanese)

[1-22] A. P. Alkhimov, V. F. Kosarev, and A. N. Papyrin: A Method of Cold Gas-Dynamic Deposition, Sov. Phys. Dokl., 35 (1990), pp. 1047-1049, Transl. American Inst. of Phys., (1991).

[1-23] A.P. Alkimov, V.F. Kosarev, N.I. Nesterovich, and A.N.Papyrin: Method of Applying Coatings, Russian Patent No.1618778, 8 Sept 1990 4.

[1-24] A.P. Alkhimov, A.N. Papyrin, V.F. Kosarev, N.I. Nesterovich, and M.M. Shushpanov: Gas-dynamic spray method for applying a coating. U.S. Patent No. 5,302,414; April 12, 1994.

[1-25] A.P. Alkimov, A.N. Papyrin, V.F. Kosarev, N.I. Nesterovich, et al.: Gas Dynamic Spraying Method for Applying a Coating,"U.S. Patent No. 5,302,414; April 12, 1994, Re-examination Certificate, Feb. 25.

[1-26] A.P. Alkhimov, A.N. Papyrin, V.F. Kosarev, N.I. Nesterovich, and M.M. Shushpanov: Method and device for coating. European Patent No. 0 484 533 B1; Janu. 25, 1995.

[1-27] A. N. Papryin: Cold Spray Technology, Advanced Materials & Processes, 159 (9) (2001) p. 49.

[1-28] R.E. Bloses, T.J. Roemer, A.J. Mayer, D.E. Beatty, and A.N. Papyrin: Automated Cold Spray System: Description of Equipment and Performance Data, Proceedings International Thermal Spray Conference (ITSC-2003).

[1-29] P. Richer, D. W. Krömmer, P. Heinrich, "Equipment and Engineering and Process Control for Cold Spraying", Proceedings International Thermal Spray Conference (ITSC-2002, Essen, Germany, March 2002)

[1-30] W. Kroemmer, P. Heinrich, P. Richter: "Cold Spraying – Equipment and Application Trends" Proceedings International Thermal Spray Conference (ITSC-2003).

[1-31] Otto Cheng: "Equipment engineering and process control for Cold Spraying" Proceedings International Thermal Spray Conference (ITSC-2004).

[1-32] R.C. Dykhuizen, and M.F. Smith: Gas Dynamic Principles of cold Gas, J. of Thermal Spray Tech, 7 (2) (1999) p.205

[1-33] R.C. Dykhuizen, M.F. Smith, D.L. Gilmore, R.A. Neiser, X. Jiang, and S. Smapth: Impact of High Velocity Cold Spray Particle, J. Therm. Spray Tech. 8 (4) (1999) p.599

[1-34] D.L. Gilmore, R.C. Dykhuizen, R.A. Neiser, T.J. Romer, and S. Smapth: Particle Velocity and Deposition Efficiency in Cold Spray Process, J. Therm. Spray Tech. 8 (4) (1999) p.576.

[1-35] R.C. Dykhuizen, M.F. Smith, D.L. Gilmore, R.A. Neiser, X. Jiang, and S. Smapth: Impact of High Velocity Cold Spray Particles, P00998A US DOE Res SAND-98-2682-J (1998) 1

[1-36] M. Grujicica, J.R. Saylor, D.E. Beasley, W.S. DeRosset, and D. Helfritc: Computational analysis of the interfacial bonding between feed-powder particles and the substrate in the cold-gas dynamic-spray process, Applied Surface Science, 219 (2003) pp. 211–227

[1-37] K Takayama: Shock wave hand book, Springer Japan (1995) p. 1076. (in Japanese)

[1-38] A. Kubota: "Detonation welding, current states and application" Welding technology, (1985) p. 33. (in Japanese)

[1-39] H. Assadi, F. Gartner, T. Stoletenhoff, and H. Kreye: Bonding Mechanism in Cold Gas Spraying, Acta Materialia, 51 (2003) pp. 4379-4394.

[1-40] J. Vleck, H. Huber, and H. Voggenreiter: Kinetic Powder Compaction Applying the Cold Spray Process-A Study on Parameter, Proc. Of Proceedings International Thermal Spray Conference ITSC2001, (2001)

[1-41] K.Sakaki, T.Tajima, H. Li, S. Shinkai, and Y.Shimizu: Influence of Substrate Conditions and Traverse Speed on Cold Sprayed Coatings, Proceedings International Thermal Spray Conference (ITSC-2004).

[1-42] T. Stoltenhoff, H. Kreye and H. Richter. J Thermal Spray Tech 11 (2002), p. 542-550.

[1-43] J. Karthikeyan and C.M. Kay, Cold Spray Technology: An Industrial Perspective, Thermal Spray 2003: Advancing the Science and Applying the Technology, C. Moreau and B. Marple, Ed., ASM International, (2003), p 117–121.

2 Cold Spraying

2.1 Introduction

MCrAlYs are difficult to deposit by cold spraying because they are hard and are difficult to deform plastically. Recently, a few researchers have demonstrated that it is possible to produce cold-sprayed MCrAlY coatings [2-1, 2]. However, the optimal spray conditions and the deposition mechanism for cold spraying of MCrAlYs are not completely understood yet. Therefore, a fundamental study of the influence of the spray parameters and spraying procedure is required.

As mentioned in Chapter 1, there are several MCrAlYs, such as CoNiCrAlY, NiCrAlY, CoCrAlY and also the elemental additional modified MCrAlY materials. These materials are selected for use according to situation. Various sizes of MCrAlY particle are commercially available; these are optimized for various thermal spray techniques such as plasma spray and HVOF. Commercially produced CoNiCrAlY, which was used in this study, is the most conventional type of MCrAlY. The size of powder was optimized for low pressure plasma spraying. This kind of powder has been studied widely and is easily obtainable. The gas selection is one of the most important parameters for cold spraying. Nitrogen, which is obtained easily and at a low price, was used as the working gas in this study.

The KINETIKS 3000 (CGT-Cold Gas Technology GmbH) cold-spray facility was used to produce cold-sprayed MCrAlY coatings. This cold spray system has one of the largest market shares of the commercially available cold spray facilities in the world. Therefore, the knowledge that was obtained using this facility has a great spillover effect for many researchers and industries.

This chapter deals with the influence of parameters such as the powder feed rate tendency and gas temperature. The deposition efficiency of cold-sprayed coatings is also discussed using specimens with sparsely deposited particles. Finally, cold-sprayed MCrAlY coatings were produced using the optimal spray conditions obtained in the study.

2.2 Experimental

2.2.1 Powder

CoNiCrAlY (SULZER METCO, AMDRY9951) was used as a coating material. This material was in the form of gas-atomized powder, so the particle shape was spherical as shown in Fig. 2-1. The particle size is -37 +5 μm (-400 mesh + 5 μm). The chemical composition is shown in Table 2-1.

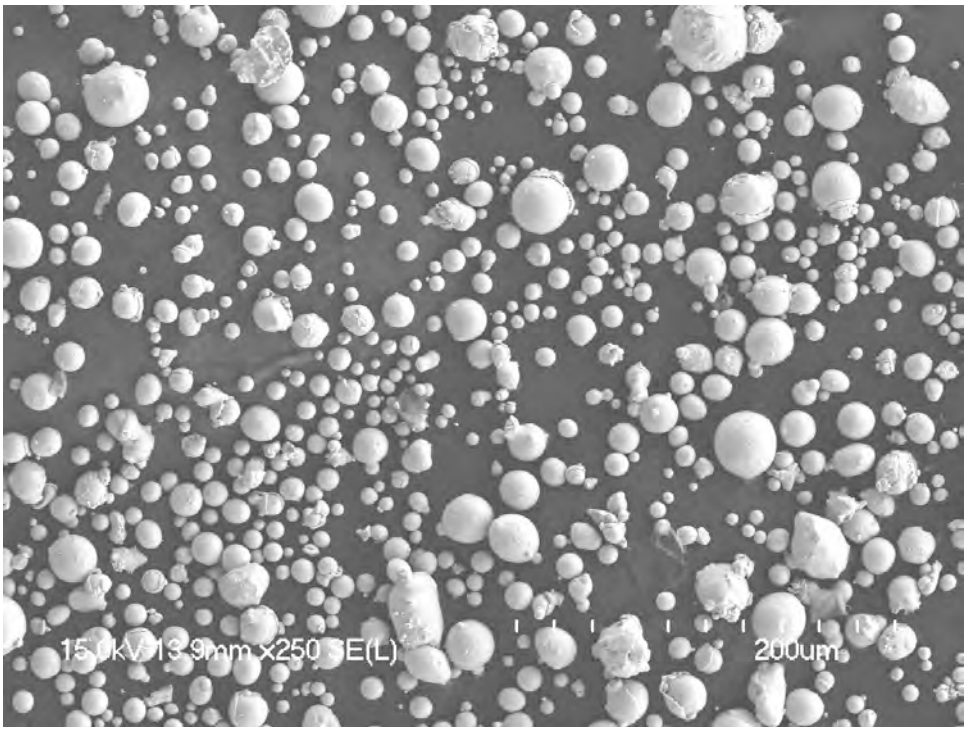

Fig. 2-1 Typical SEM image of AMDRY 9951 CoNiCrAlY powder.

Table 2-1 Chemical composition of CoNiCrAlY (AMDRY9951) powders (wt.%)

Co	Ni	Cr	Al	Y
Bal.	32	21	8	0.5

2.2.2 Cold spray facility

The CoNiCrAlY coatings were sprayed using a KINETIKS 3000 (CGT, Germany) cold-spray facility at the Centre de Compétence en Projection Plasma, Centre des Matériaux, École nationale supérieure des Mines de Paris, Evry, France (Figs. 2-2, 3). This system consists of a spray gun, heating unit, powder feeder and control unit. A schematic illustration of the cold spray system is shown in Fig. 2-4.

A working gas was used as a powder propellant gas and powder carrier. Heating up the propellant gas to moderate temperatures increases its ability to flow and results in a significantly increased velocity of the gas before it enters the gun nozzle. The gas temperature was measured at the nozzle end and feedback-controlled using the measured temperature. In the case of helium, the maximum gas temperature and pressure are 500 ºC and 30 bar, respectively. If using nitrogen, these are 600ºC and 30 bar, respectively. Compressed and pre-heated gas is supplied from a diagonally backward oriented gun and powder is supplied in an axial direction. Mixed gas and particles are accelerated in the nozzle and injected from the gun end. The solid particles, which are injected from the gun, impinge on the substrate to make the coating.

Fig. 2-2 KINETIKS 3000 cold spray system component [2-3].

Fig. 2-3 KINETIKS 3000 cold spray system at Centre de Compétence en Projection Plasma, Centre des Matériaux, École nationale supérieure des Mines de Paris (Evry, France), (Left: Atmosphere control chamber, Right: Gun nozzle with manipulator).

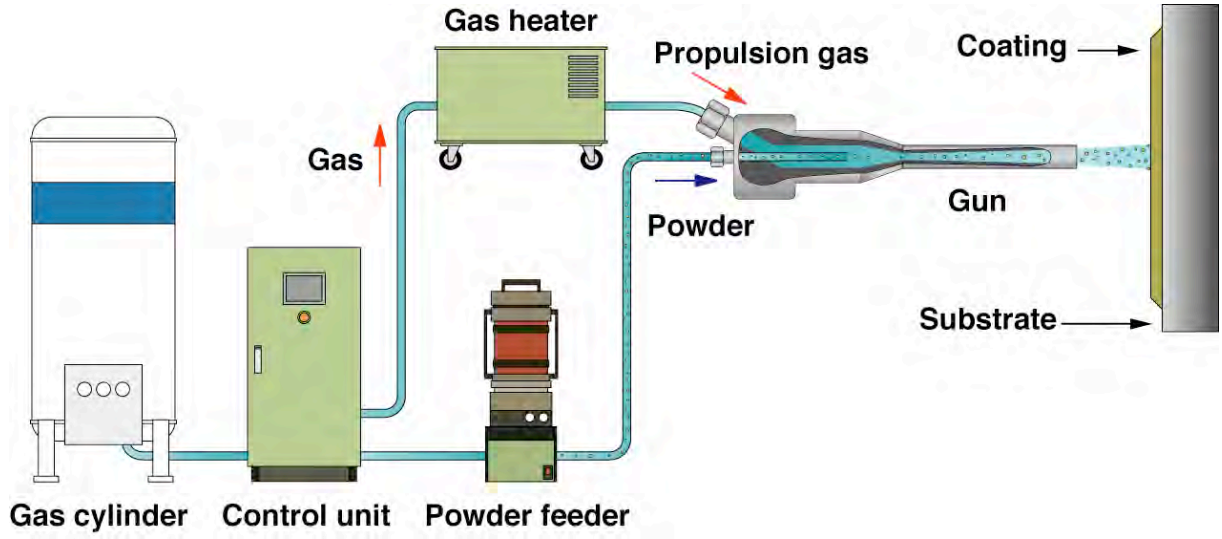

Fig. 2-4 Schematic illustration of KINETIKS 3000 cold spray system [2-3].

2.3 Results and Discussion

2.3.1 Selection of working gas

The cold spray process requires a working gas for particle acceleration. Helium, nitrogen or air are commonly used as the cold spray working gas. Table 2-2 summarizes the characteristics of these cold-spray working gases. Because of the existence of 78 % nitrogen in air, the specific parameters of air and nitrogen such as, gas constant, specific heat ratio, and density are almost the same, and accordingly the particle acceleration characteristics are almost the same. In the cold spray process, however, the working gas is used at a high temperature, for example 500 ℃. Therefore, the use of oxygen introduces concerns about oxidation during cold spraying, and hence using inert nitrogen is better than using active air. In order to select the working gas, we have estimated the difference in gas and particle velocities at the nozzle end for helium and nitrogen gases.

Table 2-2 Characteristics of cold spray working gases

Gas	Molecular weight (g/mol)	Gas constant (J/kg K)	Specific heat ratio	Density (kg/m^3)	Cost (JPY/m^3)
Helium	4.002	2077.2	1.67	0.1785	1480
Nitrogen	28.006	296.9	1.40	1.2505	190
Air	28.95	287.2	1.40	1.2928	Free

From the one-dimensional numerical model of the cold spray gas flow, which was developed by Dykhuizen and Smith [2-4], the gas velocity at the nozzle end can be described using the following isentropic relations:

$$v_g = M\sqrt{\gamma RT} \tag{2-1}$$

$$T = \frac{T_O}{1+(\gamma-1/2)M^2} \tag{2-2}$$

where v_g is the gas velocity at the nozzle end, M is the Mach number of the gas, γ is the specific heat ratio and R is the gas constant (the universal gas constant divided by the molecular weight of the gas), T is the temperature and T_O is the stagnation temperature. Eq. (2-2) is substituted in Eq. (2-1) to obtain:

$$v_p = M\sqrt{\frac{\gamma RT_O}{1+(\gamma-1/2)M^2}} \tag{2-3}$$

Grujicic *et al.* analyzed the relationship between Mach number M and different values of nozzle expansion ratio, A/A^* (A is the cross-sectional area of the nozzle end, $A^*$is the cross-sectional area of the nozzle throat), for several values of the specific heat ratio γ to obtain the function:

$$M = \left[k_1\frac{A}{A^*} + (1-k_1)\right]^{k_2} \tag{2-4}$$

where k_1 and k_2 are functions of the specific heat ratio, γ. A non-linear polynomial regression analysis was used to establish the γ-dependence of k_1 and k_2 as:

$$k_1 = 218.0629 - 243.5764\gamma + 71.7925\gamma^2 \tag{2-5}$$

$$k_2 = -0.122450 + 0.281300\gamma \tag{2-6}$$

The variation of the Mach number with the nozzle expansion ratio and the gas specific heat ratio γ of helium and nitrogen, which is calculated by Eq. (2-4), is shown in Fig. 2-5. The nozzle expansion ratio increases with Mach number and with the difference in Mach number between helium and nitrogen. The nozzle geometry was determined from the nozzle expansion ratio, and the nozzle expansion ratio of the KINETIKS 3000 type cold spray facility used in this study was almost 3. The Mach numbers of helium and nitrogen were determined to be 2.9937 and 2.6551, respectively.

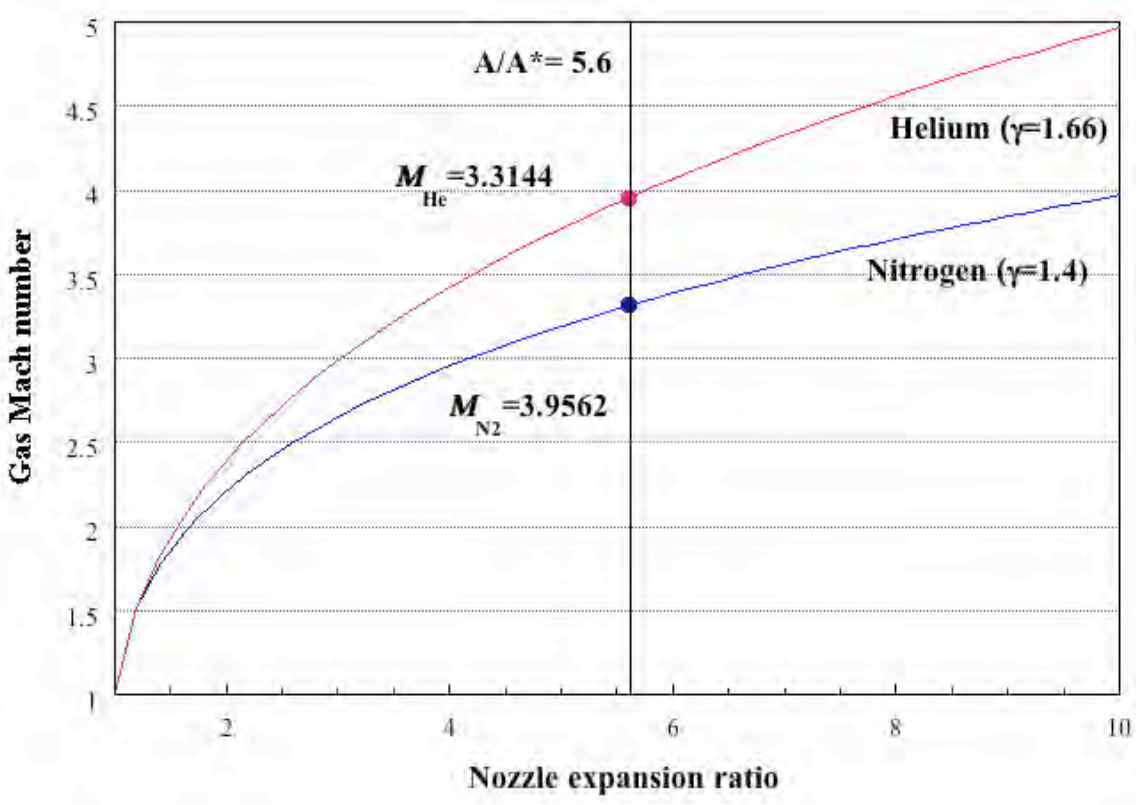

Fig. 2-5 *Variation of the Mach number with the nozzle expansion ratio and the gas specific heat ratio γ.*

The velocity ratio of helium and nitrogen (v_{He}/v_{N2}) can be estimated using Eq. (2-7). Since the gas specific characteristics and nozzle shape have been decided, the v_{He}/v_{N2} ratio is constant and independent of gas temperature. In this case, the v_{He}/v_{N2} ratio is 2.592. In other words, the velocity of helium gas is 2.592 times higher than that of nitrogen in this nozzle.

$$\frac{v_{He}}{v_{N2}} = \frac{M_{He}\sqrt{\dfrac{\gamma_{He}R_{He}T}{1+(\gamma_{He}-1/2)M_{He}^{2}}}}{M_{N2}\sqrt{\dfrac{\gamma_{N2}R_{N2}T}{1+(\gamma_{N2}-1/2)M_{N2}^{2}}}} = \frac{M_{He}\sqrt{\dfrac{\gamma_{He}R_{He}}{1+(\gamma_{He}-1/2)M_{He}^{2}}}}{M_{N2}\sqrt{\dfrac{\gamma_{N2}R_{N2}}{1+(\gamma_{N2}-1/2)M_{N2}^{2}}}} = 2.592 \tag{2-7}$$

However, the velocity of the particles, which are accelerated by the propellant gas, depends strongly on the density of gas. The particle velocity is defined as:

$$v_p = v_g\sqrt{\frac{3\rho_g C_D x}{\rho_p D_p}} \tag{2-8}$$

where v_p is the particle velocity at the nozzle end, r is the density, C_D is the drag coefficient and Dp is the drag force of the powder.

Parameters describing the particles such as those mentioned above depend only on the type of the particle. In this study only CoNiCrAlY was used. Hence these parameters are constant. By assuming the drag parameters are constant in Eq. (2-8), the particle velocity can be described as a function of gas velocity and density. The velocity ratio of helium and nitrogen (v_{pHe}/v_{pN2}) can be estimated using Eq. (2-9), and hence the ratio is constant and the value of the ratio is almost the same in this testing condition. As a result, using either gas, the particle velocity at the nozzle end is similar

$$\frac{v_{pHe}}{v_{pN2}} = \frac{v_{He}\sqrt{\frac{3\rho_{He}C_D x}{\rho_p D_p}}}{v_{N2}\sqrt{\frac{3\rho_{N2}C_D x}{\rho_p D_p}}} = \frac{v_{He}}{v_{N2}}\sqrt{\frac{\rho_{He}}{\rho_{N2}}} = 0.9793 \qquad (2\text{-}9)$$

At the adjacent substrate area, the supersonic impinging jet flow is complicated as shown in Fig. 2-6 [2-5], and the actual particle impingement velocity is affected by the jet flow at this area. The gas selection should consider the actual impingement velocity and this phenomenon. However, the particle velocity at the nozzle end using either helium or nitrogen is similar. Nitrogen is less expensive than helium; therefore, nitrogen was selected as the working gas in this study.

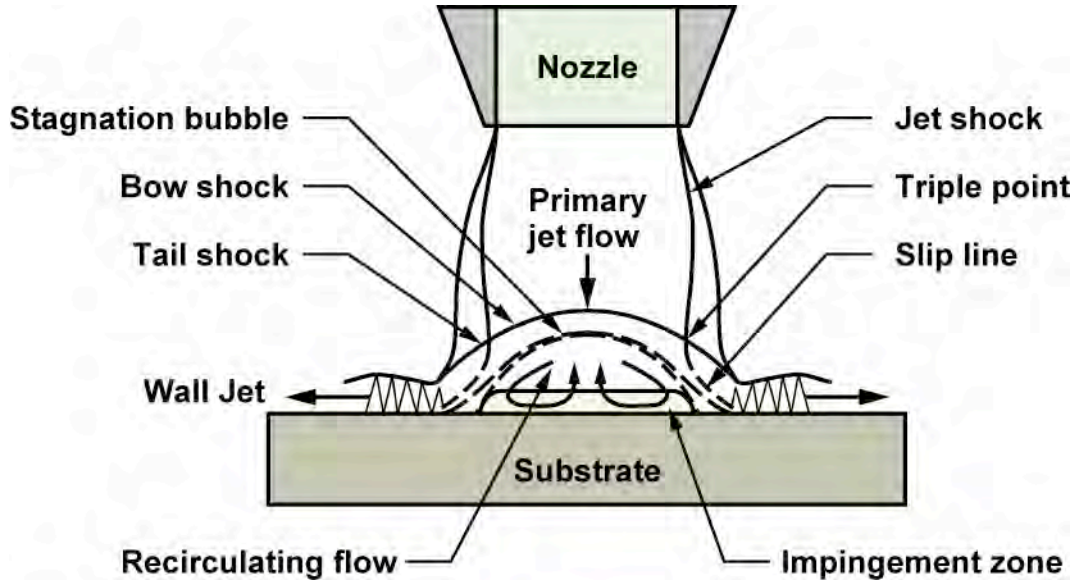

Fig. 2-6 Schematic illustration of a supersonic impinging jet flow field [2-5].

2.3.2 Powder feed rate tendency

Figure 2-7 shows the powder feeder of the KINETIKS 3000 cold-spray system. This powder feeder consists of two chambers, namely the powder supply chamber and the powder storage chamber. These two chambers are separated by a rotating disc, which has a slit. This rotating disc controls the feed rate of powder for the supply chamber. The powder dropped in from the storage chamber is injected by the powder supply gas and is carried to the gun. The powder feed rate is affected by the shape and density of the powder. In particular, a high-density powder, such as CoNiCrAlY, is difficult to supply. In order to obtain a good coating, a stable powder supply and an understanding of the powder feed rate are very important. The powder feed rate was controlled by the disc rotation speed and the gas pressure. In this study, the effect of the disc rotation speed was investigated under 3.2 MPa gas pressure. The test was examined under several rotation speed conditions, which are summarized in Table 2-3. The powder was supplied for one minute, and then the supplied powder was captured at the gun end without spraying and the weight of the captured powder was measured.

The relationship between powder feed rate and rotation speed is shown in Fig. 2-8. The amount of supplied powder varies linearly with the disc rotation speed. Using this system, under 3.2 MPa pressure, it is possible to supply CoNiCrAlY in a stable manner.

Fig. 2-7 Powder feeder of KINETIKS 3000 cold spray system.

Table 2-3 Testing condition of the powder feed rate

Material	AMDRY 9951 CoNiCrAlY
Facility	CGT KINETIKS 3000
Gas	Nitrogen
Powder carrier gas pressure	30 MPa
Disc rotation speed	1, 3, 5, 8.5 rpm
Duration	1 min

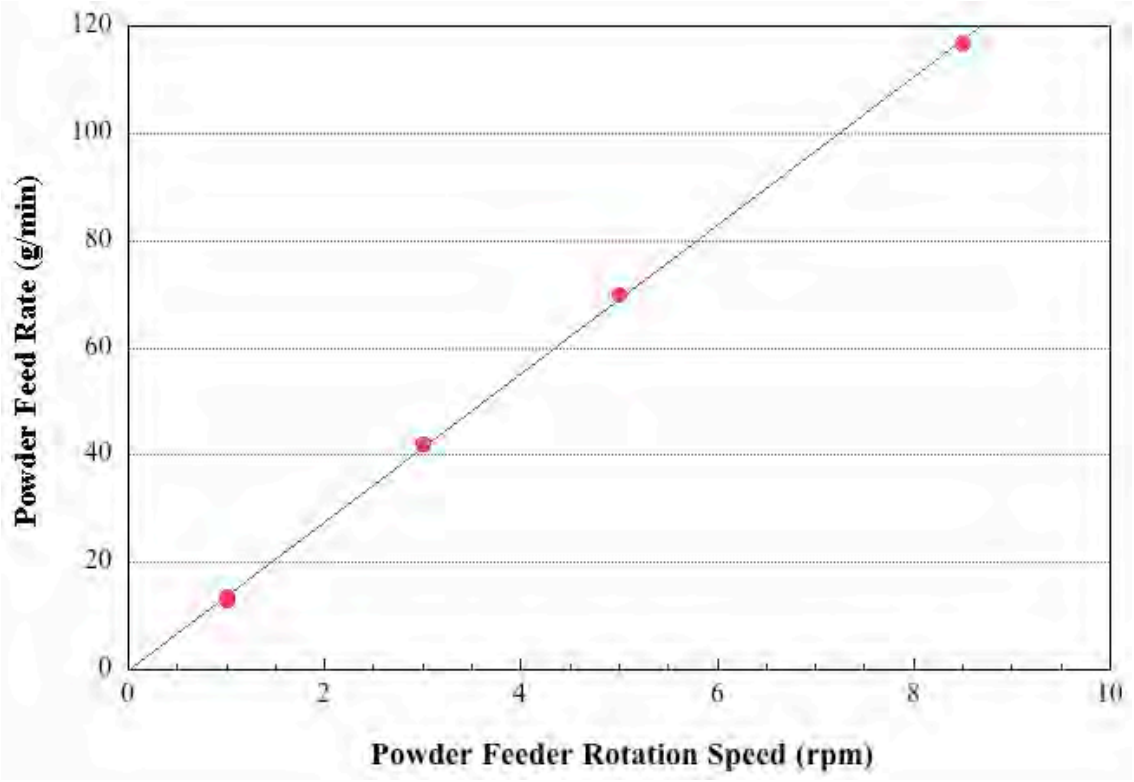

Fig. 2-8 Relationship between powder feeder rotation speed and powder feed rate of AMDRY 9951 CoNiCrAlY powder using at KINETIKS 3000 cold spray system.

2.3.3 Gas temperature effect on spray efficiency

The dependence of spray efficiency on gas temperature was studied by comparison with specimens prepared using different gas temperatures. The specimens were prepared using different gas temperatures, namely 400 ℃ and 600 ℃. INCONEL 625 was used as substrate material. The chemical composition of INCONEL 625 is shown in Table 2-4. The spray conditions are summarized in Table 2-5. The spray efficiency was compared and judged by visual examination of the specimens.

Table 2-4 Chemical composition of INCONEL 625 (wt.%)

Ni	Cr	Mo	Nb	Fe
Bal.	21	9	4	3.5

Table 2-5 Cold spray conditions to investigate the temperature dependence

Material	AMDRY 9951 CoNiCrAlY
Facility	CGT KINETIKS 3000
Gas	Nitrogen
Gas Pressure	30 MPa
Gas Temperatures	400 and 600 ℃
Powder feed rate	13.0 g/ min
Traverse speed	300 mm/s

Fig. 2-9 shows photographs of sprayed specimens obtained using different gas temperatures. In a comparison between the results of 400 ℃ and 600℃, the specimen sprayed at 600 ℃ has a much higher amount of deposit on the substrate. As a result of increasing the gas temperature, the gas and particle velocities increase, as indicated by Eq. (2-1) and (2-3). From these results, increasing the gas temperature improves the spray efficiency, and hence in this study the 600 ℃ gas condition was used. This temperature is the maximum gas temperature of nitrogen available using this spray facility.

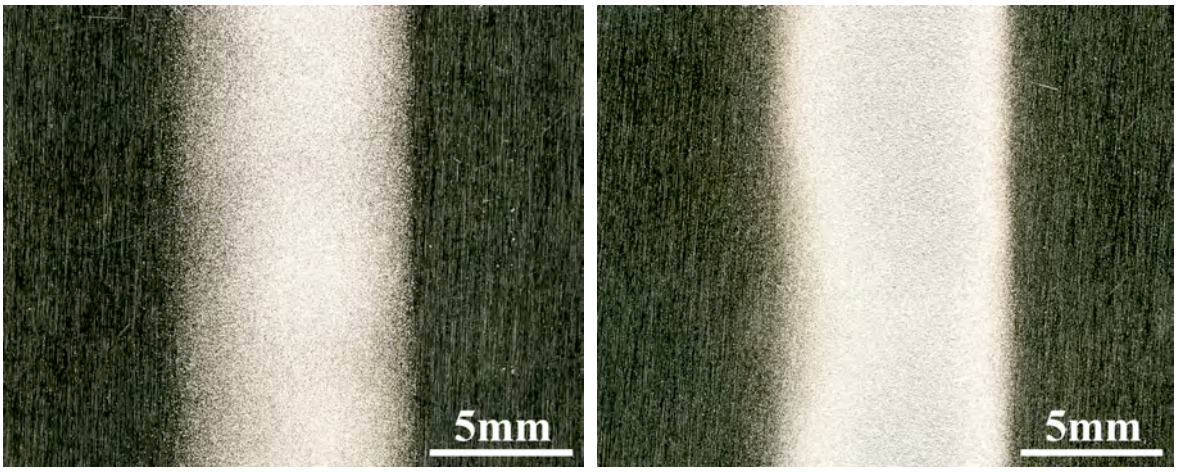

(a) 400ºC (b) 600 ºC

Fig. 2-9 Deposition efficiency dependence on gas temperature (bright particles are deposited CoNiCrAlY particles on polished INCONEL 625 substrate).

2.3.4 Particle deposition efficiency of cold sprayed CoNiCrAlY

As discussed in Section 2.3.3, the 600 ºC gas condition has a better deposition efficiency. In this session, a quantitative approach for particle deposition efficiency is discussed. The particle deposition efficiency of cold spraying was investigated using a sparse particle deposited specimen, which was made with a low powder supply and a high traverse speed. The spray conditions are shown in Table 2-6. Using these spray conditions and single traverse spraying, a sparse particle deposited specimen was obtained. The substrate material is the Ni-base superalloy INCONEL 625. Prior to spraying, the substrate material was polished using waterproof abrasive papers (#320 to #1500) and mirror polished using colloidal silica.

Table 2-6 Cold spray conditions to make a sparse particle deposited specimen

Material	AMDRY 9951 CoNiCrAlY
Facility	CGT KINETIKS 3000
Gas	Nitrogen
Gas Pressure	30 MPa
Gas Temperature	600 ºC
Powder feed rate	6.9 g/ min
Traverse speed	300 mm/s

The particle deposition efficiency E_{Add}, defined by the total number of impinging particles, N_{Total} and the number of deposited particle, N_{Dep}, is given by Eq. (2-10).

$$E_{Add} = \frac{N_{Dep}}{N_{Total}} \tag{2-10}$$

The measurement procedure was conducted using the following steps:

1. Taking SEM images (magnification 250 times) at 10 positions for each condition
2. Counting the number of deposited particles and rebounded traces
3. Obtaining the total numbers of impinged particles, which were defined as (number of deposited particles) + (number of rebounded traces)
4. Calculating the particle deposition efficiency using Eq. (2-10).

Fig. 2-10 shows an SEM image of a sparse particle deposited specimen and a schematic illustration of deposited particles and rebounded traces. In the case of 600 ℃ nitrogen gas, the calculated particle deposition efficiency was 83.9 %. In this discussion, the deposition efficiency was defined as the relationship between the total number of impinging particles and the number of deposited particles, as described by Eq. (2-10). Using the cold spraying system, almost all of the particles that were introduced into the nozzle were accelerated and sprayed, and hence we can assume the number of impinging particles to be equal to the number of supplied particles. Accordingly, the deposition efficiency, which is defined by the relationship between the total number of impinging particles and the number of deposited particles, corresponds to the spray efficiency, which is calculated from the total number of input particles and deposited particles with this assumption. Many researchers have reported the spray efficiency of conventional thermal spraying. From the report of Dorfman et al. [2-6], the spray efficiency of the plasma spray technique was from 20 to 30%, because the plasma has wide distributions of temperature and velocity, and hence the number of particles satisfying good spray conditions is very low. The cold spray technique has the advantage of higher spray efficiency compared to the plasma spray technique.

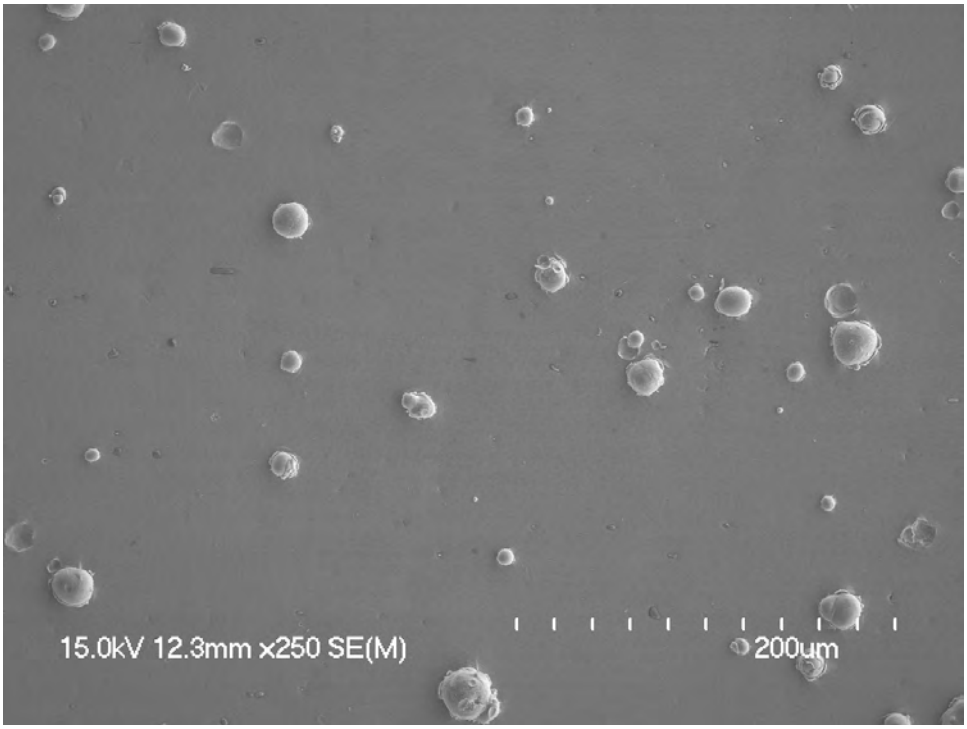

(a) SEM image

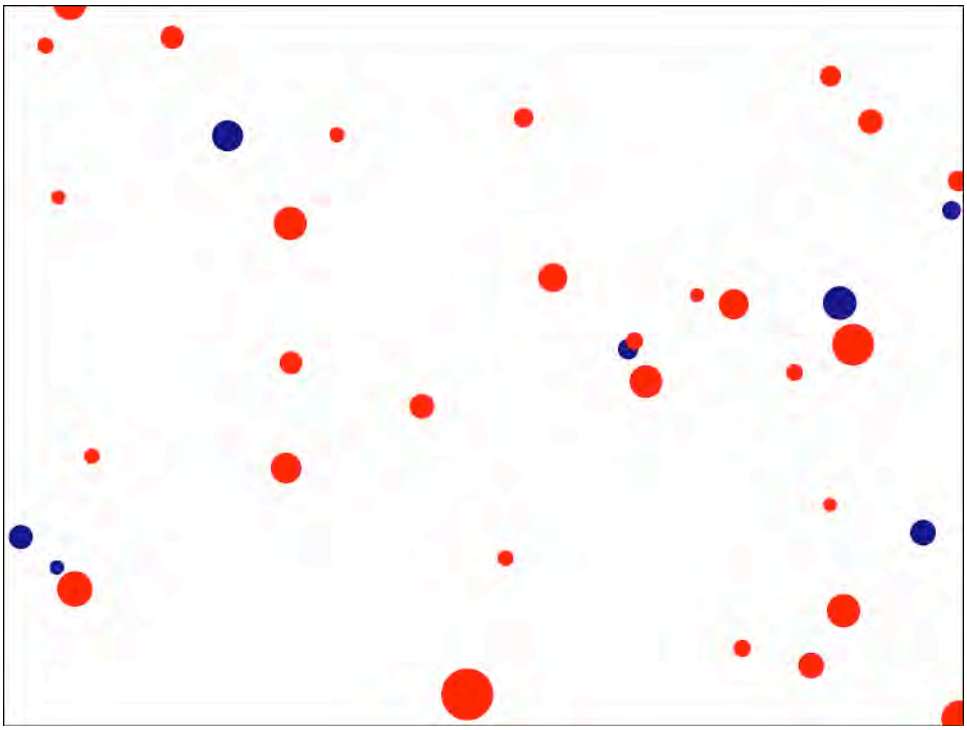

(b) Deposition relationship (Red: deposited particle, Blue: rebound trace)

Fig. 2-10 SEM image and schematic of the sparse particle deposited specimen for evaluation of deposition efficiency.

2.3.5 Cold spraying parameters and as-sprayed coatings

Finally, a comparison was made between the morphologies of cold and thermal spray coatings. The coating conditions used for cold spraying were summarized in Table 2-7. A Ni-based INCONEL 625 superalloy sample with dimensions of 50 × 50 × 4 mm^3 was used as the substrate. It was grit-blasted with 300 μm diameter corundum prior to cold spraying. The results of cross-sectional SEM observation of the coating obtained are shown in Fig. 2-11. In order to compare the quality of this coating with that from low-pressure plasma sprayed CoNiCrAlY, the results of cross-sectional SEM observation of a low-pressure plasma sprayed CoNiCrAlY coating, which was obtained using the spray conditions given in Table 2-8, is shown in Fig. 2-12. Using the optimized cold-spray parameters, we could obtain a dense and thick CoNiCrAlY coating by the cold spray technique. The cold-sprayed CoNiCrAlY coating is as dense as low-pressure plasma sprayed coatings.

Table 2-7 Spray condition of cold spraying

Material	AMDRY 9951 CoNiCrAlY
Facility	CGT KINETIKS 3000
Gas	Nitrogen
Gas Pressure	30 MPa
Gas Temperature	600 ℃
Powder feed rate	13.5 g/ min
Spray distance	40 mm
Traverse speed	300 mm/s

Table 2-8 Spray conditions for low-pressure plasma splaying

Material	AMDRY 9951 CoNiCrAlY
Gun	Praxair SG-100
Powder feeder	Praxair 1264 type
Primary Gas	Argon (345 kPa)
Secondary Gas	Helium (345 kPa)
Power	900 A/ 30 V
Traverse speed	36 mm/s
Environment	Ar 10 kPa
Spray distance	140mm

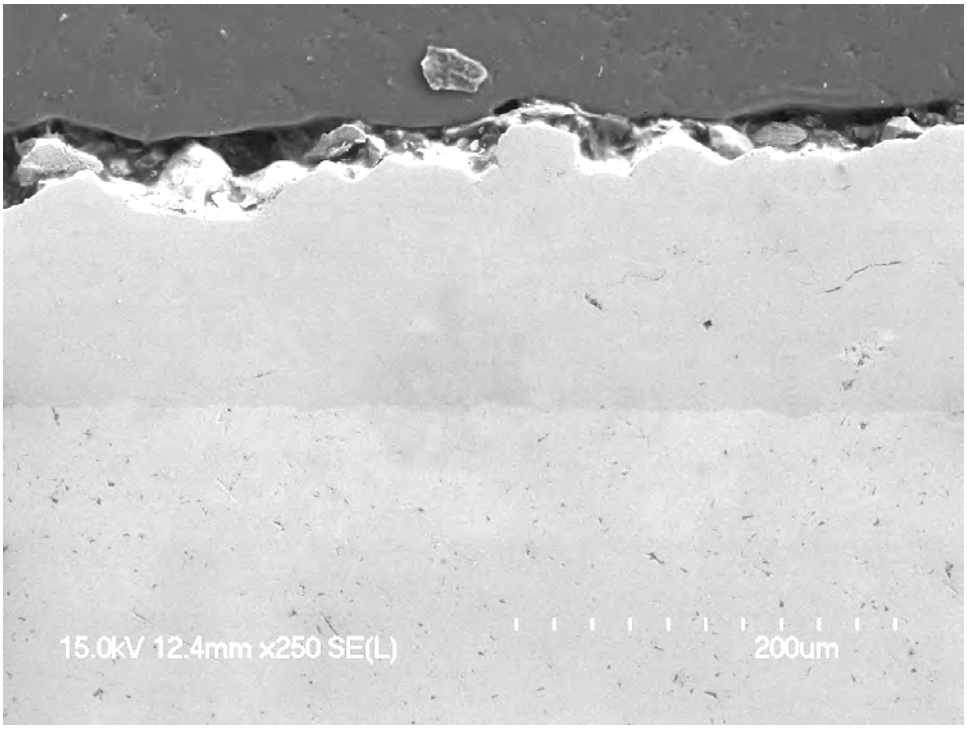

Fig. 2-11 Cross sectional SEM images of cold-sprayed CoNiCrAlY coating.

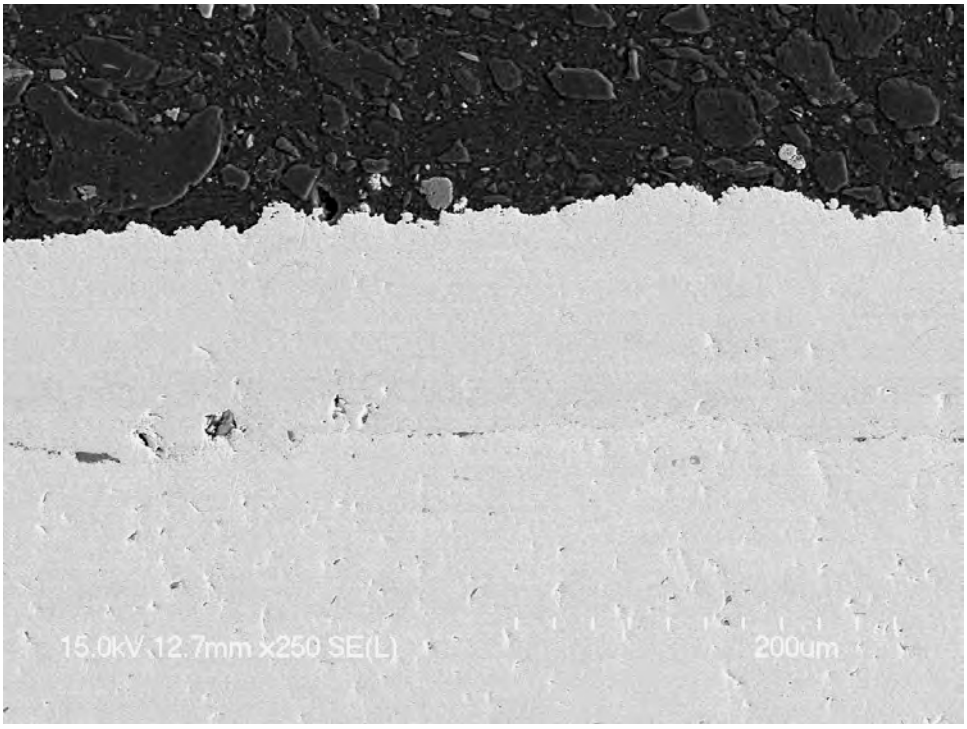

Fig. 2-12 Cross sectional SEM images of low-pressure plasma sprayed CoNiCrAlY coating.

2.4 Summary

This chapter discusses the influence of several parameters, such as the powder feed rate and gas temperature. In addition, the deposition efficiency of cold-sprayed coatings used in the sparsely particle deposited specimen was discussed. The following conclusions are drawn:

- From the results of the estimation of particle velocity, nitrogen was selected to be the working gas for CoNiCrAlY cold spraying.
- The cold spray system used (CGT, KINETIKS 3000) is capable of supplying the stabilized CoNiCrAlY powder.
- Increasing the gas temperature results in enhancement of the spray efficiency.
- When using nitrogen gas at 600 ºC, the calculated particle deposition efficiency was 83.9 %. This condition allows a dense cold-sprayed CoNiCrAlY coating to be obtained.

References

[2-1] T. Stoltenhoff, H. Kreye, and H. Richter: J Thermal Spray Technol., 11 (2002) pp. 542-550.

[2-2] J. Karthikeyan, and C.M. Kay: Cold Spray Technology: An Industrial Perspective, Thermal Spray 2003: Advancing the Science and Applying the Technology, C. Moreau and B. Marple, Ed., ASM International, (2003) pp 117–121.

[2-3] Website of CGT - cold gas technology, (http://www.cgt-gmbh.com/).

[2-4] R.C. Dykhuizen, and M.F. Smith: Gas Dynamic Principles of Cold Spray, J. Therm. Spray Technol. 7 (1998) pp.205-212.

[2-5] M. Grujicic, C.L. Zhao , C. Tong , W.S. DeRosse, and D. Helfritch: Analysis of the impact velocity of powder particles in the cold-gas dynamic-spray process, Materials Science and Engineering A368 (2004) pp.222-230.

[2-6] M.R. Dorfman, M. Nonni, J. Mallon, W. Woodard and P. Meyer: Thermal Spray Technology Growth in Gas Turbine Coatings, Proceedings International Thermal Spray Conference (ITSC-2003).

[2-7] R.C. Dykhuizen, M.F. Smith, D.L. Gilmore, R.A. Neiser, X. Jiang, and S. Smapth: Impact of High Velocity Cold Spray Particle, J. Therm. Spray Tech. 8 (4) (1999) p.599.

3 Characterization of Fundamental Properties of Cold-Sprayed MCrAlY Coatings

3.1 Introduction

In Chapter 2, cold-sprayed coatings were successfully produced. In order to determine the mechanical properties of the coatings and characterize the cold-spray coating, porosity measurements and hardness tests were carried out.

MCrAlY coatings as overlay coatings for turbine components improve their oxidation resistance and provide a longer lifetime for turbines even under high-temperature oxidation conditions. The oxide film is usually called a thermally grown oxide (TGO) layer. TGO formation behavior is one of the important aspects of MCrAlY coating. The TGO consists of an Al_2O_3 layer, and a mixed oxide layer that consists of NiO, CoO, Cr_2O_3, or (Ni, Co)(Cr, $Al)_2O_4$ spinel oxides[3-1]. The dense Al_2O_3 layer plays the role of a protective layer. However, the formation of TGO often accelerates failures of thermal barrier coatings, which consist of between MCrAlY bond coatings and ceramic (i.e. yttrium stabilized zirconia) coatings. A number of investigations were carried out to understand the oxidation mechanism of thermally spayed MCrAlY coatings [3-1 to 11].

The formation of the TGO depends not only on the chemical composition of the coating (Al and Y content) and the oxidation conditions (temperature, time, and environment), but also on the manufacturing process and the structure of the coating. Generally, conventional MCrAlY coatings can be produced by thermal spraying (vacuum plasma spraying: VPS or low-pressure plasma spraying: LPPS; high-velocity oxygen fuel spraying: HVOF) method. Recently, studies on the oxidation behavior of VPS and HVOF sprayed MCrAlY coatings [3-2, 3] have shown that the oxidation rate of HVOF coatings is lower than that of LPPS coatings. The authors explain the reason for the lower oxidation rate in terms of the fast formation of thermodynamically stable α-Al_2O_3 in the initial stages of oxidation; the Al-containing oxide particles, which were formed during spraying, favor the formation of α-Al_2O_3. Toma et al. [3-4] summarized that the oxidation rates of the HVOF sprayed coatings are two times lower than the corresponding oxidation rate of LPPS MCrAlY coatings. The main difference between the oxidation behavior is in the transient stage of oxidation as shown in Fig. 3-1.

However, the high-temperature oxidation behavior of cold-sprayed MCrAlY coatings is not yet completely understood. The purpose of this study was to investigate the oxidation behavior. In order to

compare the oxidation behavior of cold spray and LPPS techniques, high-temperature exposure tests were carried out. The oxidation rate was evaluated from the formation and thickness of the alumina and of the mixed oxide using SEM observation and EDX elemental analyses.

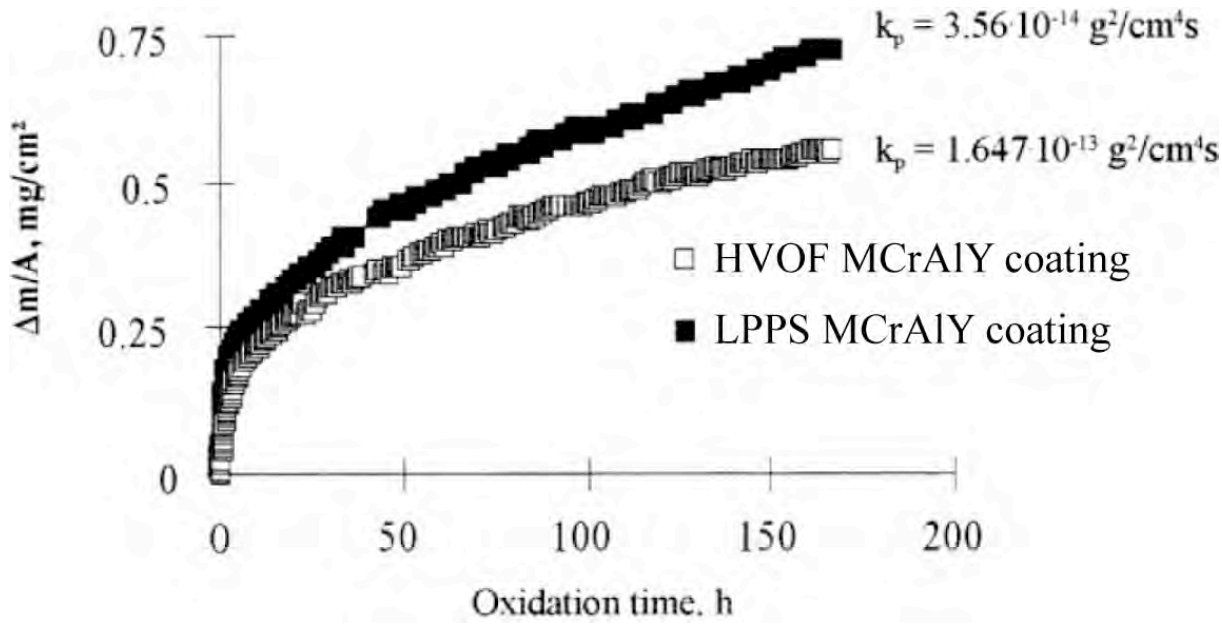

Fig. 3-1 Oxidation behavior of thermally sprayed MCrAlY coatings in synthetic air at 1050 ℃ [3-4].

3.2 Experimental

3.2.1 Cold spraying

The specimens used, which were studied by SEM observations, porosity measurements and hardness tests, were prepared using the method described in Chapter 2. In order to investigate the influence of the spray technique, cold-sprayed and low-pressure plasma sprayed CoNiCrAlY coating specimens were examined.

3.2.2 SEM observation and porosity measurements

Two as-sprayed coatings were cross-sectionally observed using a Field Emission-type Scanning Electron Microscope (FE-SEM: Hitachi S-4700). The specimens were cut and embedded in epoxy resin (BUEHLER: EPO-THIN), polished using waterproof abrasive paper (#320 to #1500) and mirror polished with colloidal silica. In order to prevent electron charge-up during the SEM observation, the sample was coated with a Pt sputtered using an ion sputtering apparatus (JEOL: JFC-1100E).

The porosity measurements were performed on cross-sectional SEM images using image analysis software (Image-J, version 3.5 for Mac OSX). In order to avoid any influence from polishing scratches and surface roughness, SEM images were taken with the backscattered electron signal. All the images were taken at 2000 times magnification, and 10 images were taken, each at 200μm intervals, at the center of the coating. The porosity was defined as the area fraction of pores in the SEM images.

3.2.3 Hardness tests

The hardness of the as-sprayed coatings was measured using a FISCHERSCOPE HM2000 type (HELMUT FISCHER GmbH + Co.KG) micro hardness testing system. The measurements were made in a direction perpendicular to the coating cross-section. Additional measurement positions were located adjacent to the coating-substrate interface. The Vickers indenter was a quadrangular pyramid-shaped diamond with an edge angle of θ =136º. The maximum load was 100 μN and the load was held at the maximum load for 20 sec. The Young's modulus of the coatings was estimated from a load penetration depth curve obtained from the indentation profile.

The tested specimens were embedded in epoxy resin and polished under the same conditions as the specimens observed by SEM. In order to evaluate the relationship between hardness and position on the coating (in terms of depth), the hardness measurements were made in a cross-sectional direction. Testing conditions are summarized in Table 3-3.

Table 3-1 Vickers hardness testing conditions

Facility	FISCHERSCOPE HM2000
Indenter	Vickers type
Loading condition	100 μN/ 20sec

3.2.4 Evaluation of high temperature oxidation behavior

High temperature exposure tests were performed in an 1100 ºC atmospheric environment inside a muffle furnace (Yamato Scientific Co., Ltd.: Type FJ-31). The durations of the tests were 24 and 100 hours.

The specimens exposed to high temperature were cut and embedded in epoxy resin (BUEHLER: EPO-THIN), polished using waterproof abrasive paper (#320 to #1500) and mirror polished with colloidal silica. In order to prevent electron charge-up during the SEM observation, the sample was coated with Pt sputtered produced by an ion sputtering apparatus (JEOL: JFC-1100E). The samples were cross-sectionally observed and the oxide film compositions were investigated by field-emission-type scanning microscopy (FE-SEM (HITACHI: S-4700)) and energy dispersive X-ray spectrometry (EDX (EDAX: Phenix type)).

3.2.5 Measurement of oxide film thickness

The oxidation rate was measured by determining the thickness of the alumina layer. The measurement procedure took place according to the following steps:

1. Taking SEM images of TGO (magnification 1000 times) at each of 20 positions.
2. Measurement of the alumina layer thickness. For the measurement, the thickness was measured in a direction perpendicular to the coating surface. The number of measurement positions was 10 equally spaced positions each image. Therefore, the total number of measurement points is 200 points. 200 measurements were considered to be enough to determine the oxidation behavior.

3.3 Results and Discussion

3.3.1 SEM observation and porosity measurements

The cross-sectional images of the as-sprayed coatings are shown in Figs. 3-2 and 3. Both the coatings have good density and are thick coatings.

An example of an SEM image is shown in Fig. 3-4. This is an image of the low-pressure plasma-sprayed coating. Using image analysis software, a binarized image was obtained. The threshold of the image contrast was automatically determined by the image analysis software. The black areas represent pores or splat boundaries. The porosity was taken as equal to the area fraction of the black area. Fig. 3-4 (b) shows a modified binarized image; in this picture, the red area indicated the porosity of the coating. From Fig. 3-4 (b), the porosity ratio was 1.3 %. The summarized average porosity data is shown in Table 3-2. From these results, it can be seen that the coating density of the cold-sprayed CoNiCrAlY coating is denser than that of the low-pressure plasma sprayed coating. Therefore, the cold-spray technique allows deposition of a much denser coating. Cold spraying coating is expected to improve the corrosion and oxidation behavior of the coating due to its higher density.

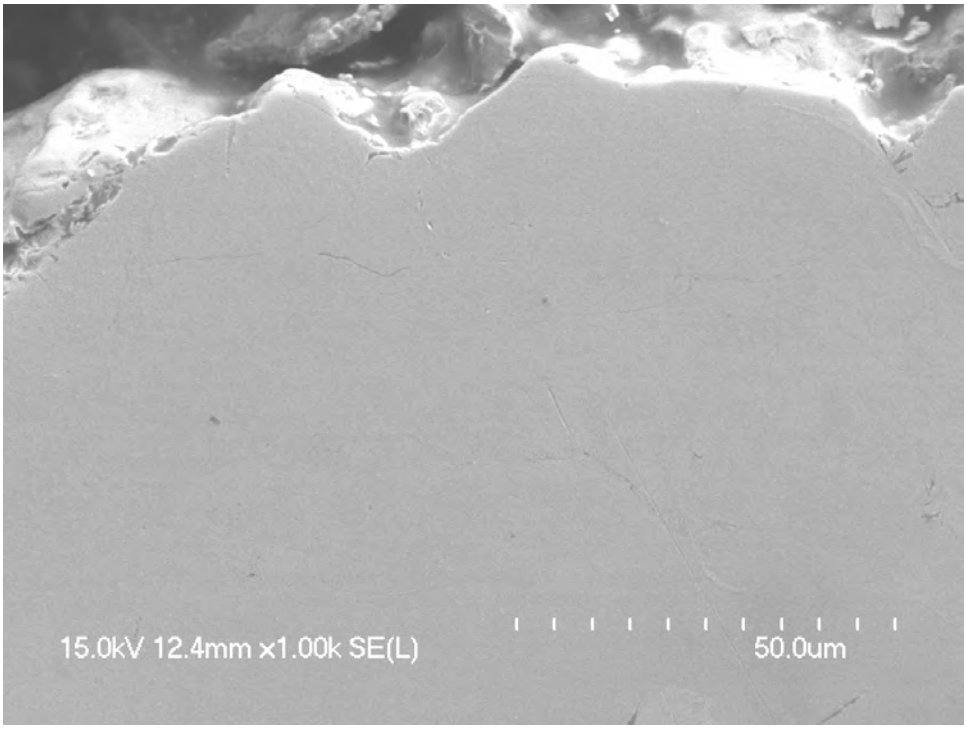

Fig. 3-2 Cross sectional SEM observation results of cold-sprayed CoNiCrAlY coating.

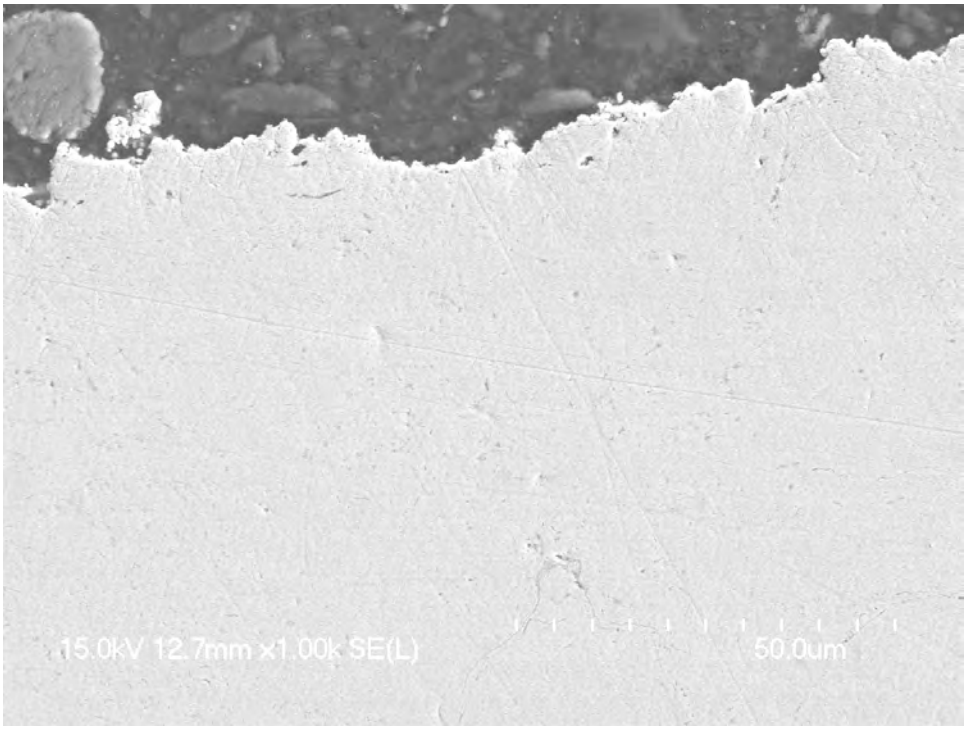

Fig. 3-3 Cross-sectional SEM observation results of cold-sprayed CoNiCrAlY coating.

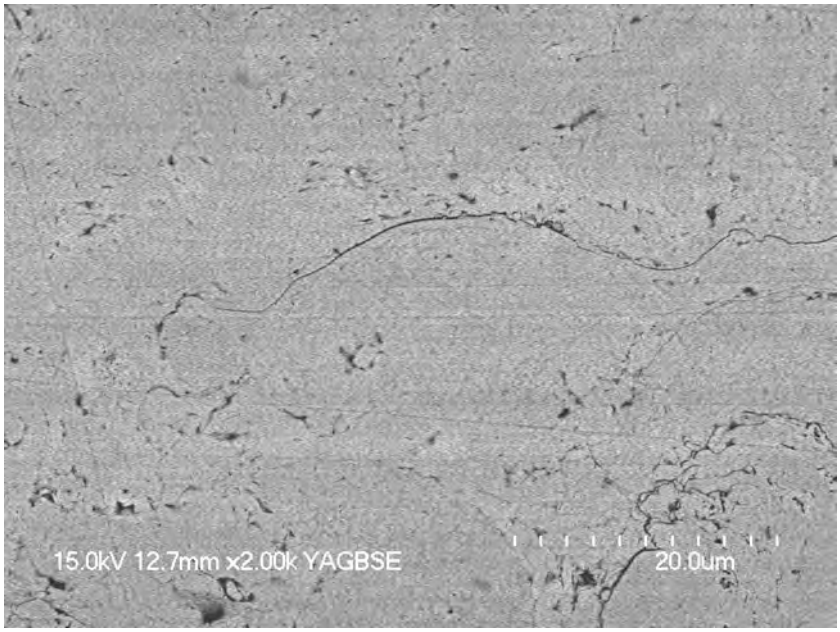

(a) SEM image

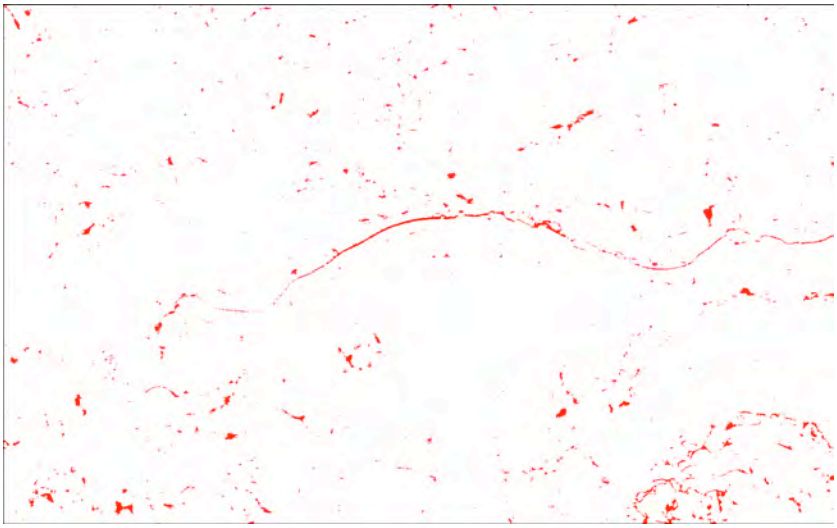

(b) Image analysis results 1.3%

Fig. 3-4 Example of image analysis porosity.

Table 3-2 Image analyses results of porosity measurement

Spray technique	Porosity
Cold-sprayed coating	**0.363 %**
Low pressure plasma sprayed coating	**2.212 %**

3.3.2 Hardness tests

Before conducting hardness tests on the as-sprayed coatings, the hardness of the as-received CoNiCrAlY powder and INCONEL substrate were measured. The powder was cross-sectionally measured using an embedded and polished specimen as shown in Fig. 3-5. The results for the as-received powder and substrate are summarized in Table 3-3. These results show that the INCONEL 625 substrate is harder than the CoNiCrAlY powder.

Fig. 3-5 *Optical microscopic observation of micro Vickers hardness tested cross-sectional cut specimen of as-received CoNiCrAlY powder.*

Table 3-3 *Vickers hardness test results on as-received CoNiCrAlY powder and INCONEL 625 substrate*

	CoNiCrAlY powder	**INCONEL 625 substrate**
Vickers hardness (Hv)	**179**	**356**

Fig. 3-6 shows the relationship between the Vickers hardness and the distance from the coating/substrate interface. Lines of average hardness lines for the as-received particle and substrate are shown in this figure. Fig. 3-7 shows the Vickers hardness distribution of as-sprayed CoNiCrAlY.

In the case of the as-sprayed coatings, the cold-sprayed CoNiCrAlY coating is much harder than the low-pressure sprayed CoNiCrAlY coating and substrate material. This hardening effect was caused by the solid-state impact. In the shot peening technique, the numerous impingements cause work hardening and grain miniaturization. Therefore, it was assumed that the cold-sprayed coatings, too, had miniaturized grain structures.

The distance from the interface has no influence on the hardness. The reason for this independence of distance was that the all of the individual particles had almost the same impingement history. Therefore, the hardness distribution range of the cold-sprayed coating was narrower than that of the low-pressure plasma sprayed coatings. Generally, plasma sprayed coatings include various phases and particles with various thermal histories particles, such as once completely melted, half melted etc. Therefore, the hardness strongly depends on the thermal history of the individual particles, and hence the low-pressure plasma sprayed coatings have wider distributions of hardness.

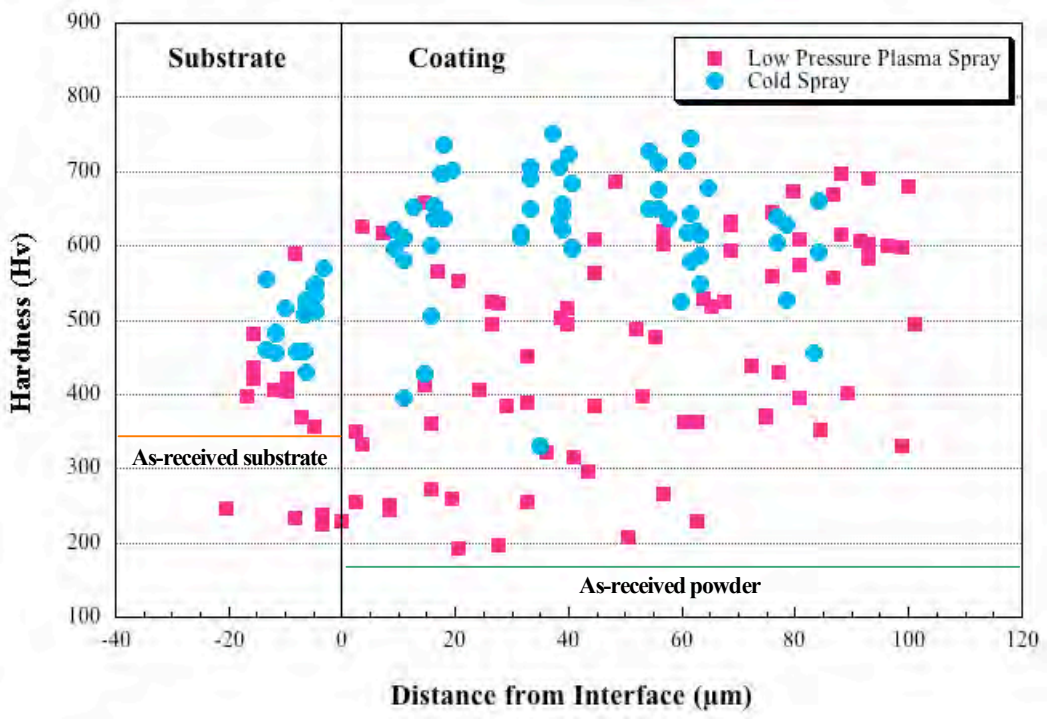

Fig. 3-6 Relationship between Vickers hardness and distance from coating/substrate interface of as-sprayed CoNiCrAlY coatings, which were produced by cold spray and low-pressure plasma spray techniques.

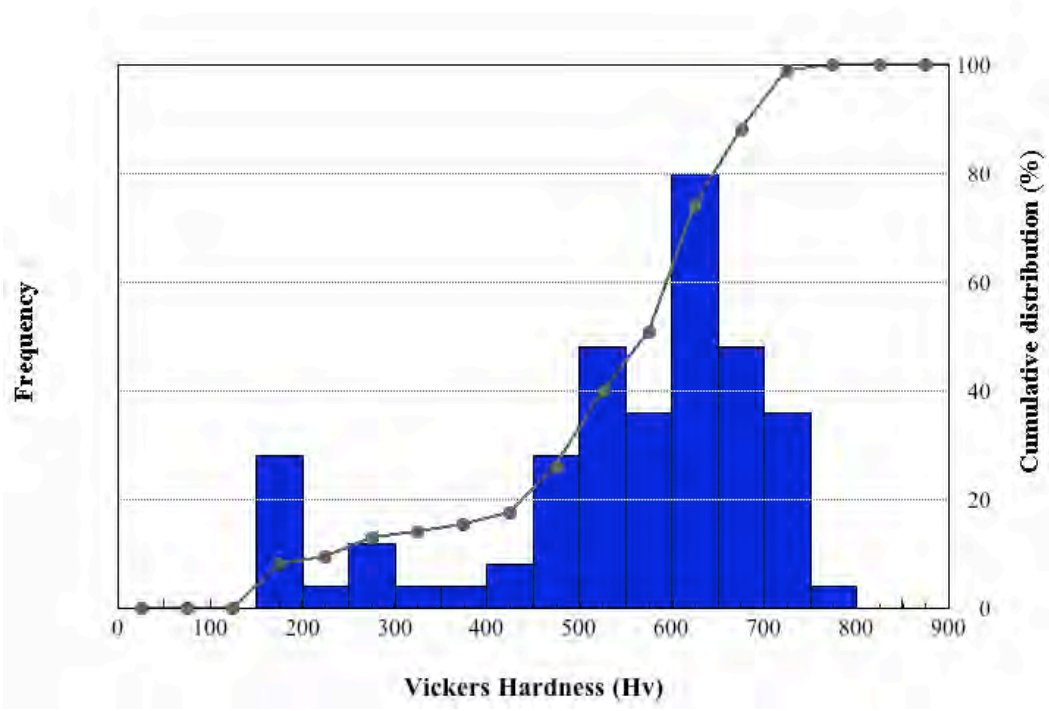

(a) Cold-sprayed coating

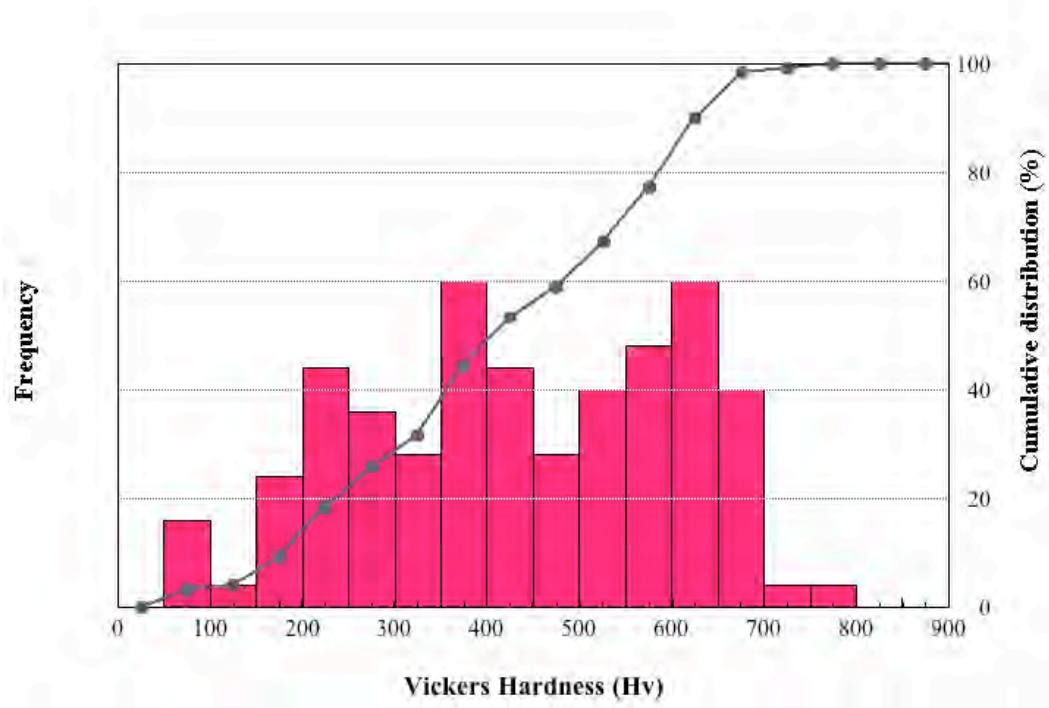

(b) Low-pressure plasma sprayed CoNiCrAlY coating

Fig. 3-7 Vickers hardness distribution of as-sprayed CoNiCrAlY coatings (a): cold-sprayed coating, (b): low-pressure plasma splayed coating.

3.3.3 Co diffusion during high-temperature exposure tests

The results of cross-sectional SEM observation and EDX elemental mapping of the specimens exposed for 100 hours at 1100 ºC are shown in Fig. 3-8. Both of the coatings formed an alumina layer uniformly. Prior to investigation of the oxidation behavior, the cobalt diffusion behavior from the coating layer to the substrate was studied. The as-sprayed CoNiCrAlY coating contains 38.5 wt.%. Co. However, the substrate does not contain Co. The Co content represents the largest compositional difference between coating and substrate. Hence, during high-temperature exposure, cobalt diffuses to substrate because of the Co concentration gradient. In EDX elemental mapping of Co in Fig. 3-8, the Co was observed below the initial coating/substrate interface of the exposed specimen. This is evidence of Co diffusion.

In order to evaluate the influence of the coating method on cobalt diffusion depth and tendency, EDX elemental line analyses were carried out. The line analysis profiles for Co are shown in Fig. 3-9. Because of the differences in coating thickness, the original point of the depth axis was set to be on the interface between substrate and coating. These Co profiles have good agreement, and hence the spray method is found to have a negligible effect on the Co diffusion depth and. In other word, there are no diffusion barriers at the interface between substrate and coating. These results indicated that the cold-sprayed MCrAlY coatings have good adhesion and contact on the substrate, similar to that of low-pressure sprayed MCrAlY coatings.

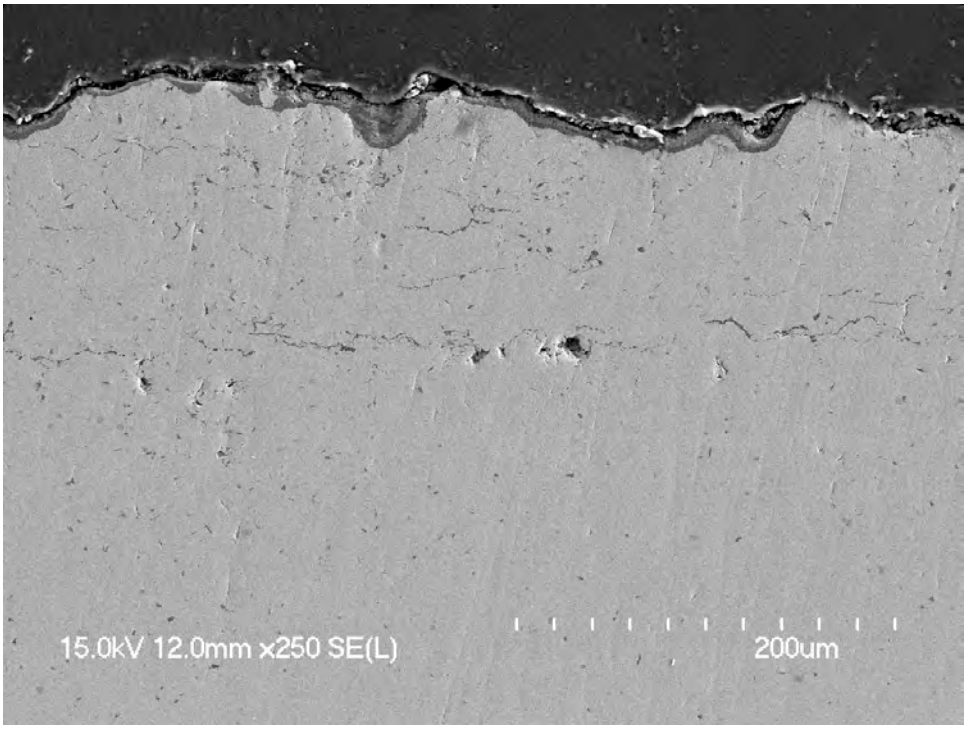

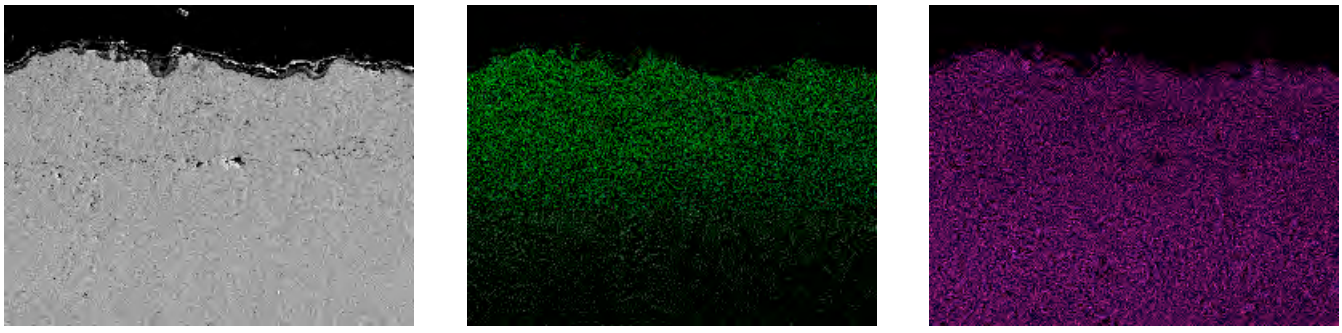

SEM **Co** **Ni**

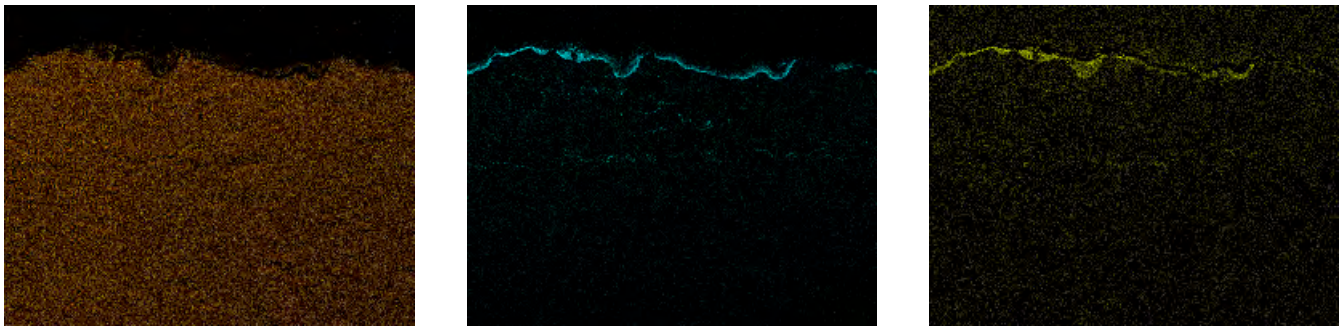

Cr **Al** **O**

(a) Cold-sprayed CoNiCrAlY coating aged for 100 hours at 1100 ℃

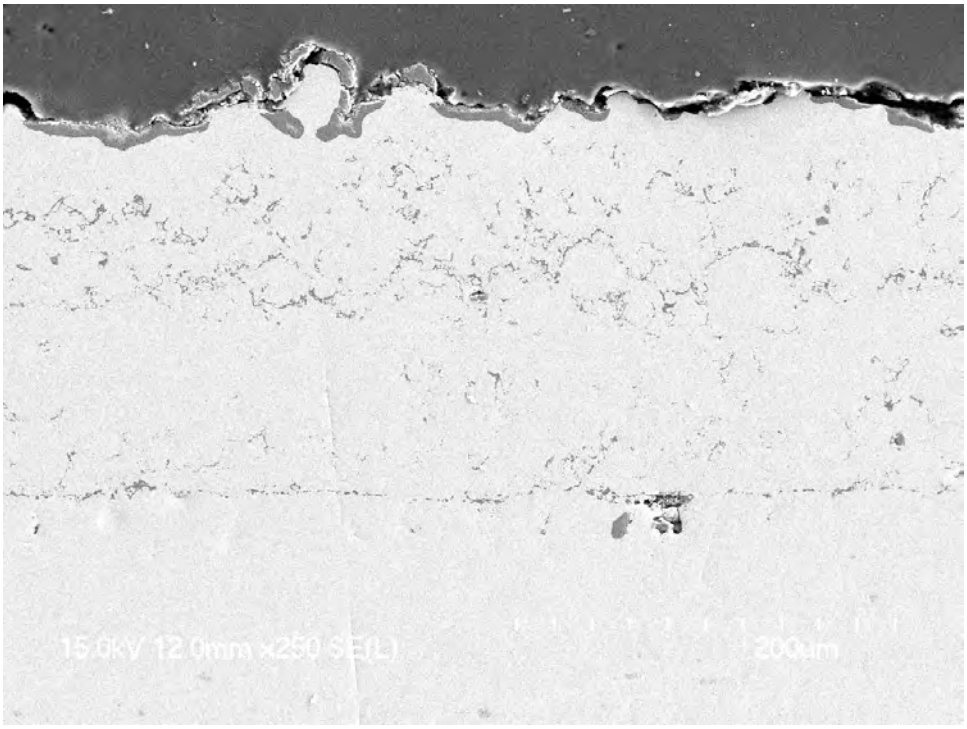

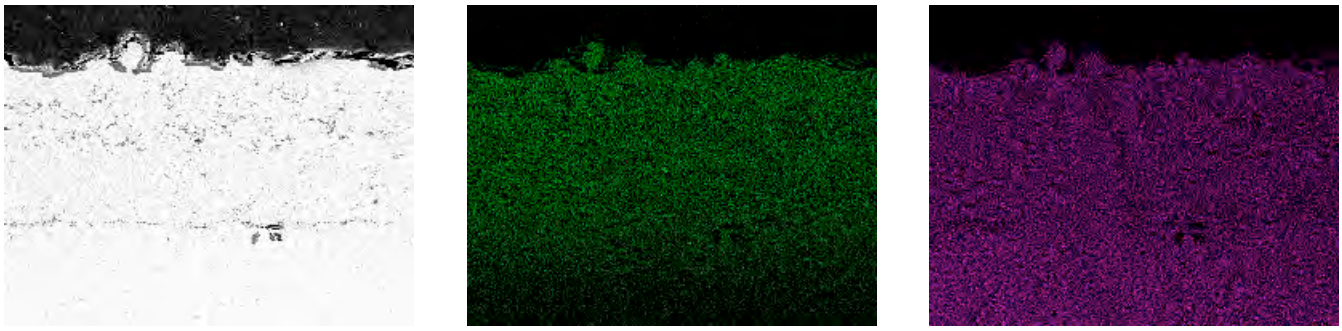

SEM **Co** **Ni**

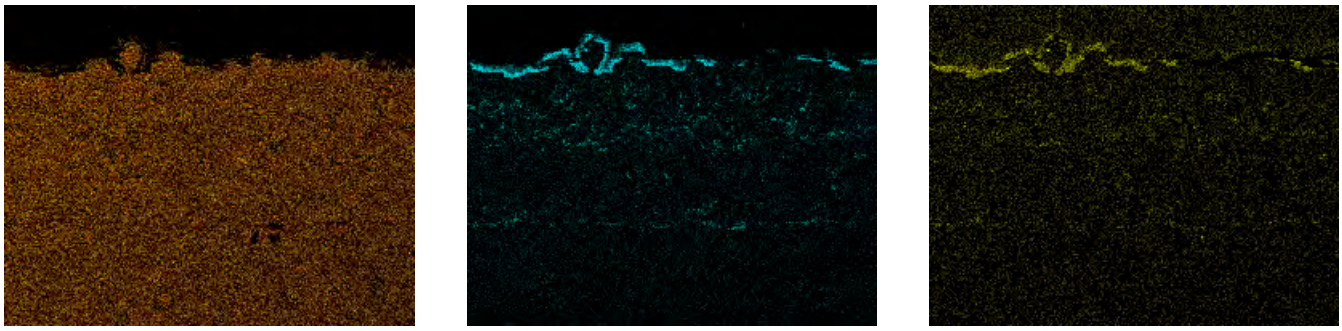

Cr **Al** **O**

(b) Low pressure plasma sprayed CoNiCrAlY coating aged for 100 hours at 1100 ℃

Fig. 3-8 SEM-EDX elemental analyses results of 100 hours aged CoNiCrAlY coatings (a): cold-sprayed coating, (b): low-pressure plasma sprayed coating.

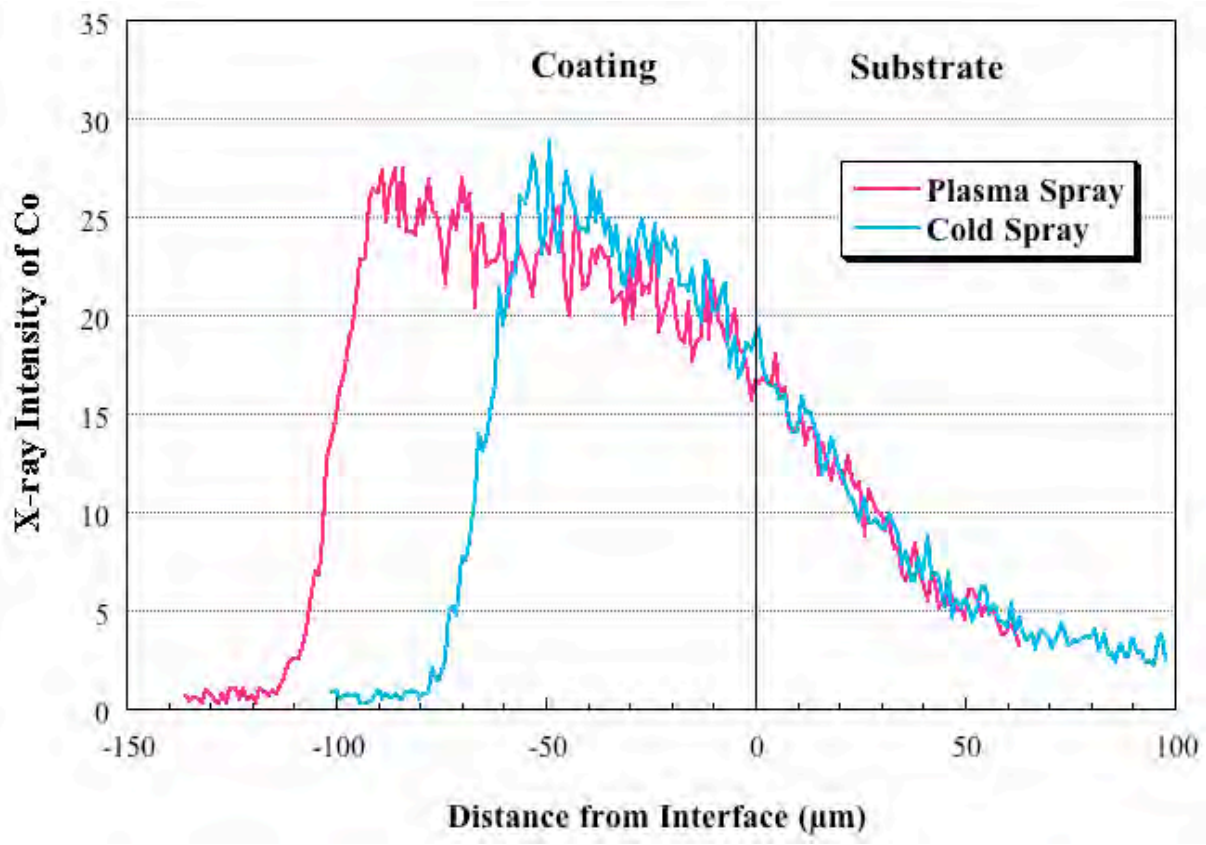

Fig. 3-9 Relationship between EDX line analyses results of Co and perpendicular distance from interface of 1100 ℃, 100-hour thermally aged CoNiCrAlY coatings.

3.3.4 Oxidation behavior in 1100 ºC atmospheric environments

From the results of EDX elemental mapping of the coatings exposed to high temperature for 100 hours, the TGO layer, mainly alumina, which appears as a black region on the SEM images, formed uniformly. Mixed oxides of Co, Ni and Cr formed locally on the alumina layer; these can be seen as gray regions on the SEM images.

The TGOs of both coatings consist of the same oxide. However, the thicknesses of the mixed oxide and alumina layers are different. Figures. 3-11 and 12 show cross-sectional SEM observations of the specimen aged for 24 hours and 100 hours.

Comparing these images, the alumina layer thickness of the cold-sprayed MCrAlY coating is greater than that of the low-pressure plasma sprayed MCrAlY coating for both testing times. The mixed oxide thickness of the cold-sprayed coating also seems to be thicker than that of the low-pressure plasma sprayed MCrAlY coating

Because the mixed oxide formation is not uniform, it is difficult to estimate quantitatively the oxidation rate of the mixed oxide. Therefore, this study uses the alumina layer thickness to estimate the oxidation rate. Figs. 3-13 and 14 show the alumina layer thickness distribution of the specimens aged for 24 hours and 100 hours. Figure 3-15 shows the oxidation ratio that was calculated from the relationship between aluminum oxide thickness and duration of aging duration of the cold-sprayed and low-pressure plasma-sprayed CoNiCrAlY coatings in an 1100 ºC atmospheric environment. It is seen that the cold-sprayed MCrAlY coating has a lower oxidation ratio than the low-pressure-plasma sprayed coating in this environment, Therefore, the cold-sprayed coating technique improves the high-temperature oxidation behavior of the MCrAlY coatings.

The primary reason for the improved high-temperature oxidation behavior is considered to be the difference in the temperature during the spraying process. The working temperature of cold spraying is lower than 600 ºC, and this lower spraying temperature spraying inhibits oxidation during spraying. In contrast, the plasma temperature is much higher than 2000 ºC, and even though the LPPS was performed in a low-pressure environment, it was difficult to prevent oxidation caused by adsorbed oxygen. This oxide acts as an oxide diffusion path and accelerates oxidation during thermal aging. Moreover, the cold-sprayed coating is denser. Higher density inhibits the diffusion through the oxide.

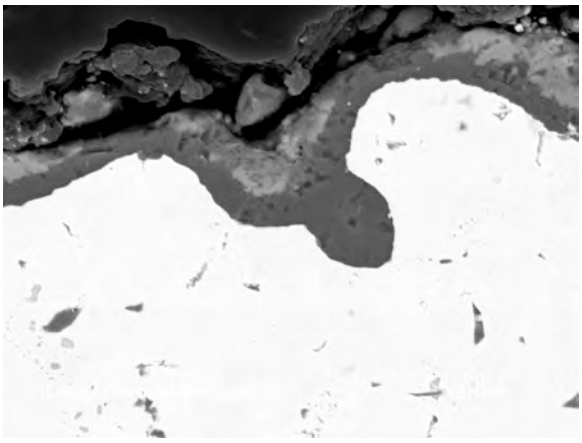

SEM (BSE)

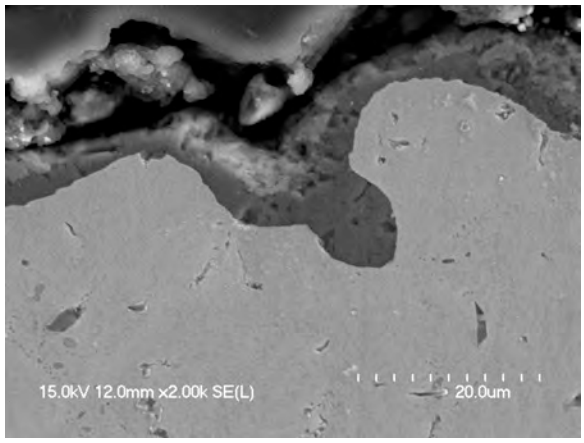

SEM (SE)

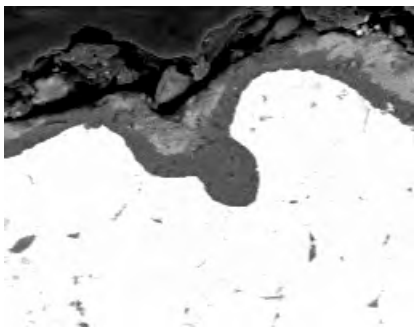

SEM

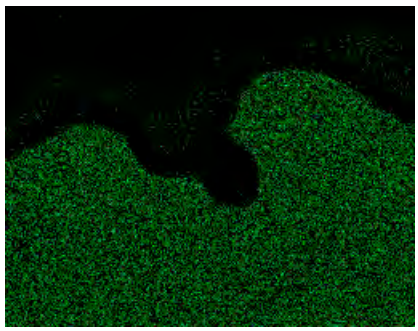

Co

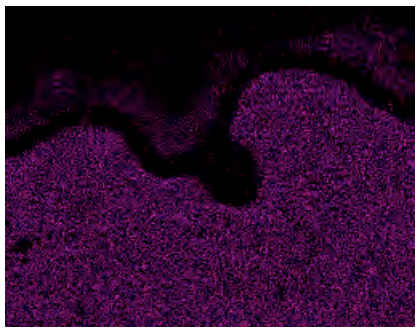

Ni

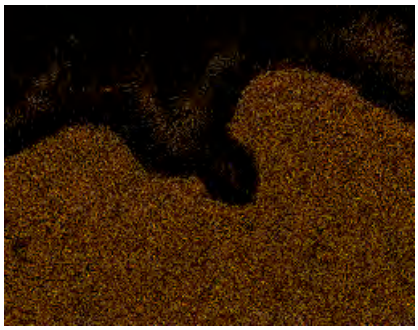

Cr

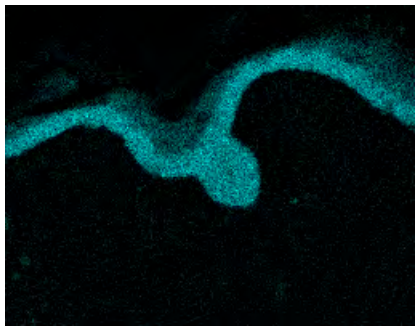

Al

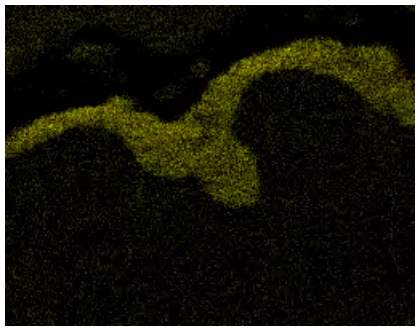

O

(a) Cold-sprayed CoNiCrAlY coating aged for 100 hours at 1100 ºC

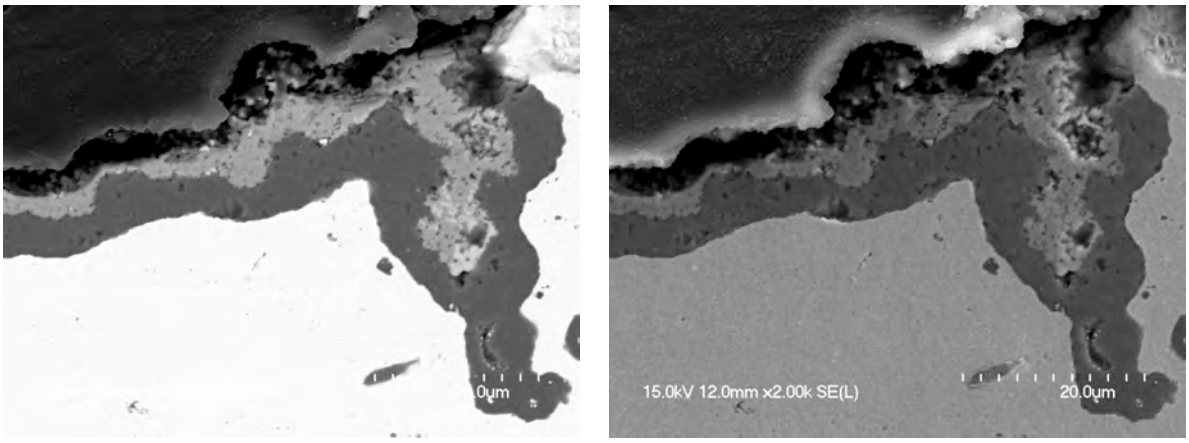

SEM (BSE) SEM (SE)

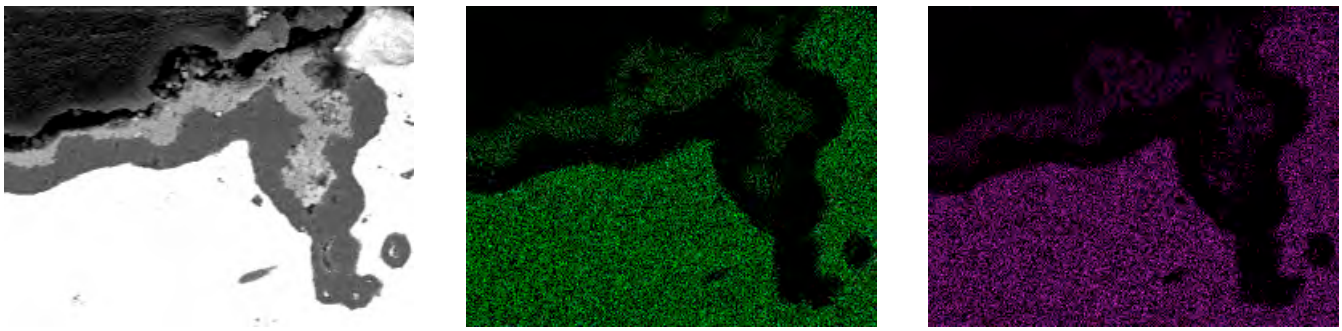

SEM **Co** **Ni**

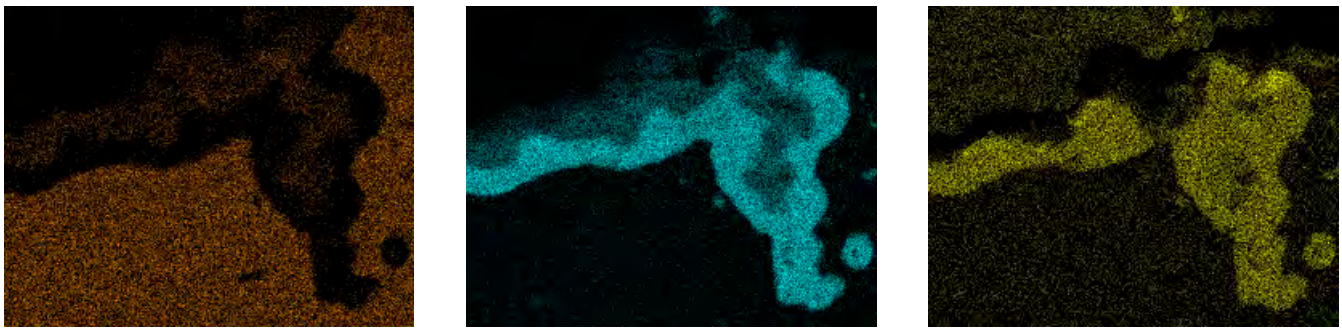

Cr **Al** **O**

(b) Low pressure plasma sprayed CoNiCrAlY coating aged for 100 hours at 1100 ℃

Fig. 3-10 SEM-EDX elemental analysis results on 100-hour aged CoNiCrAlY coatings focused on thermally grown oxide (a): cold-sprayed coating, (b): low-pressure plasma splayed coating.

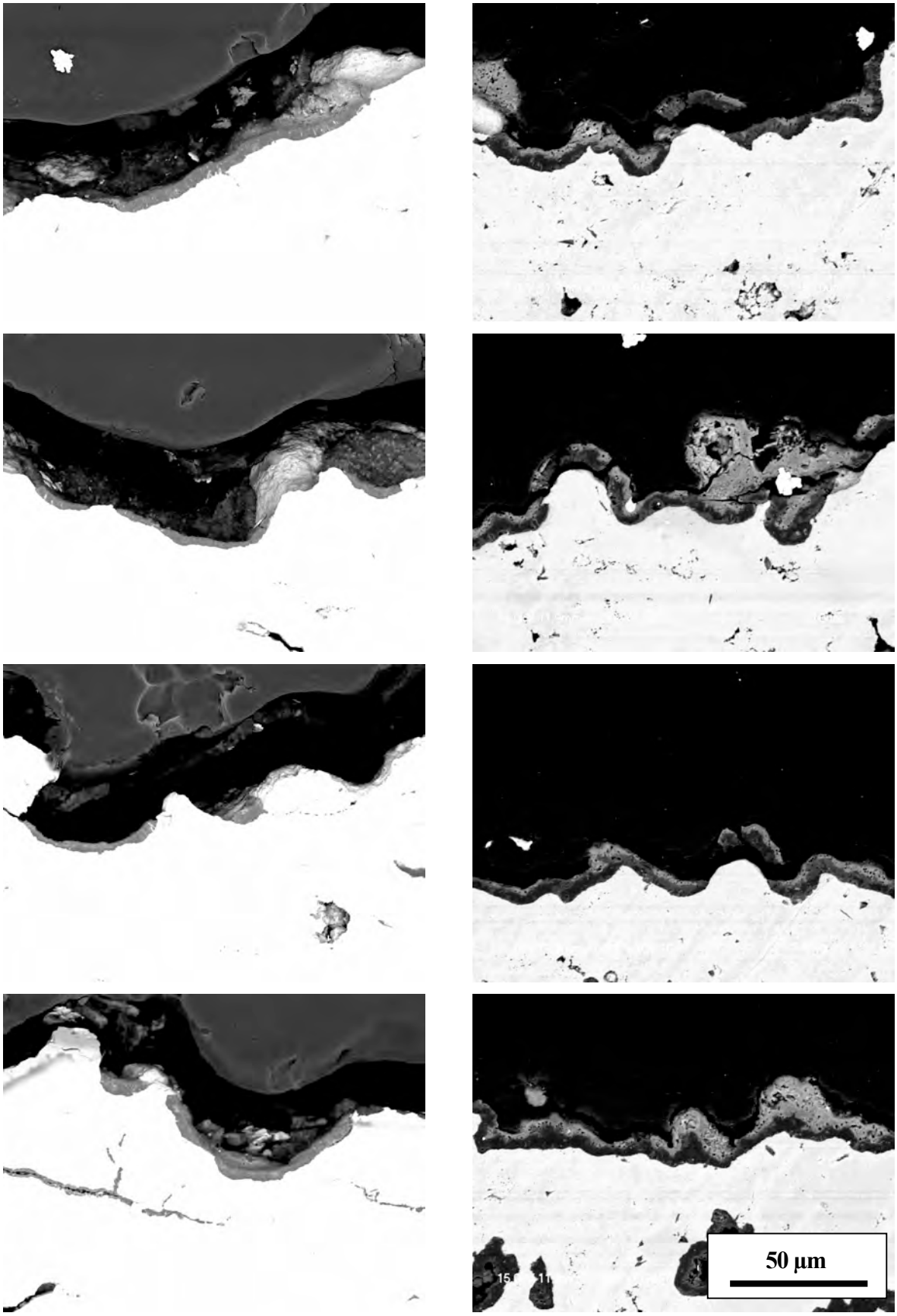

Cold-sprayed coating **Low pressure plasma sprayed coating**

Fig. 3-11 Typical SEM images of the specimens aged for 24 hours at 1100 ℃.

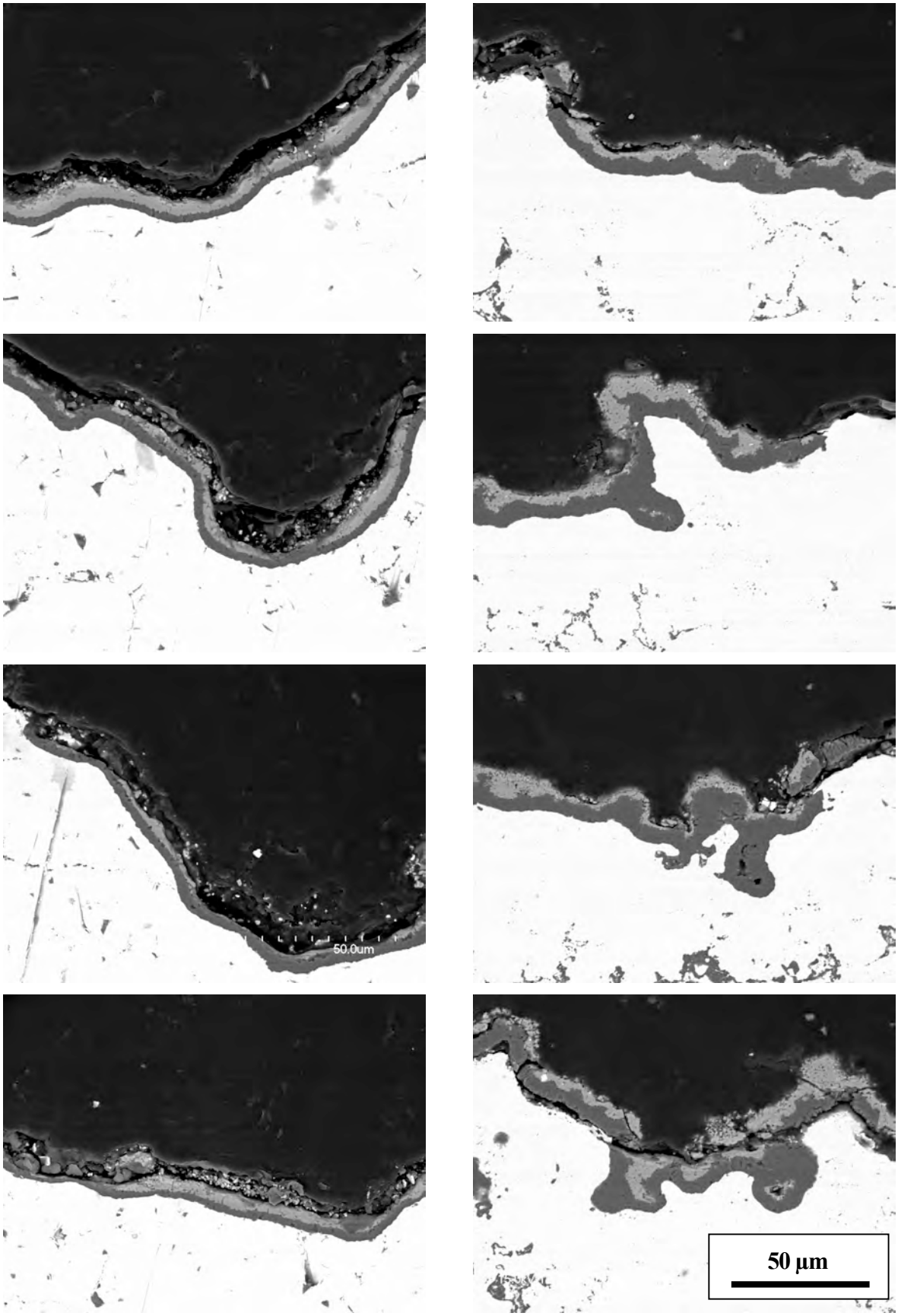

Cold-sprayed coating **Low pressure plasma sprayed coating**

Fig. 3-12 Typical SEM images of the specimens aged for 100 hours at 1100 ℃.

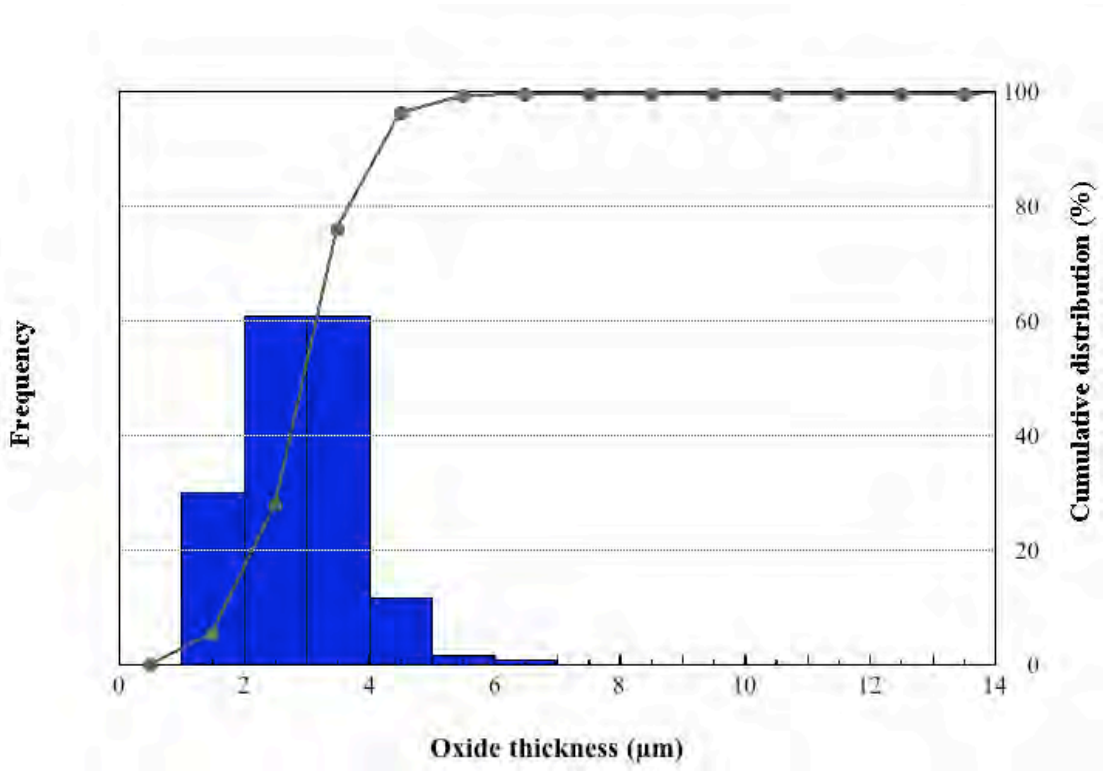

(a) Cold-sprayed CoNiCrAlY coating

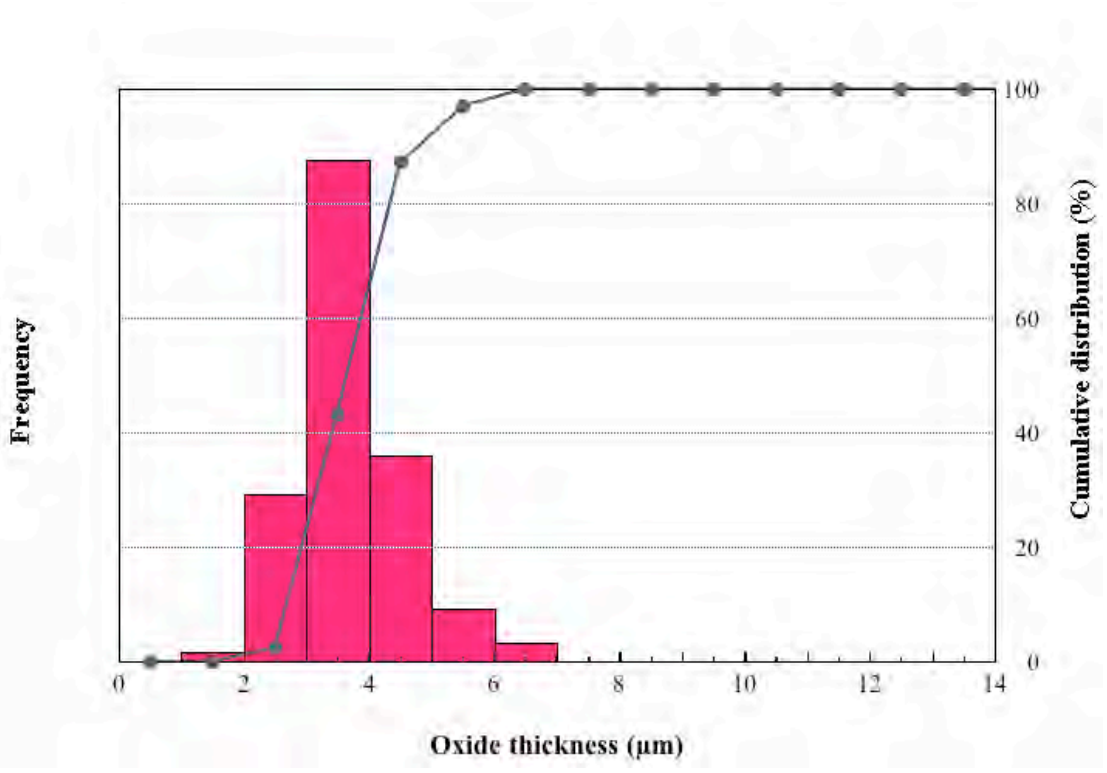

(b) Low pressure plasma sprayed CoNiCrAlY coating

Fig. 3-13 Aluminum oxide film thickness distribution of CoNiCrAlY coatings on specimens aged for 24 hours at 1100℃ (a): cold-sprayed coating, (b): low-pressure plasma-sprayed coating.

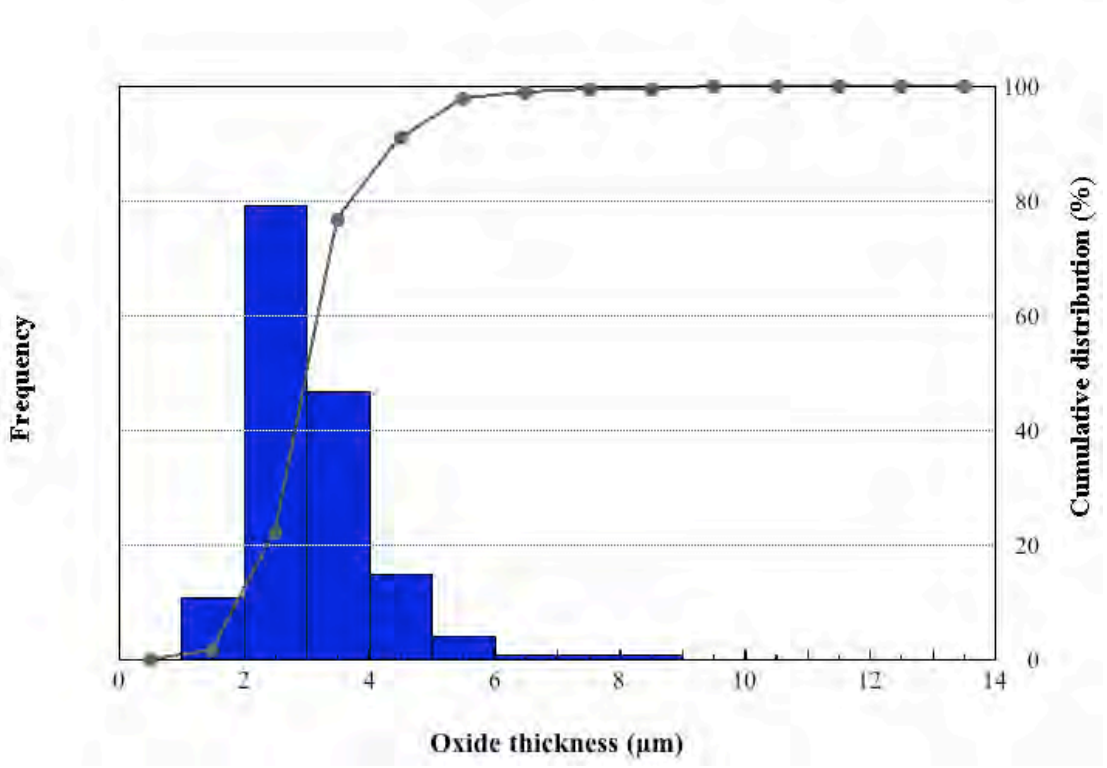

(a) Cold-sprayed CoNiCrAlY coating

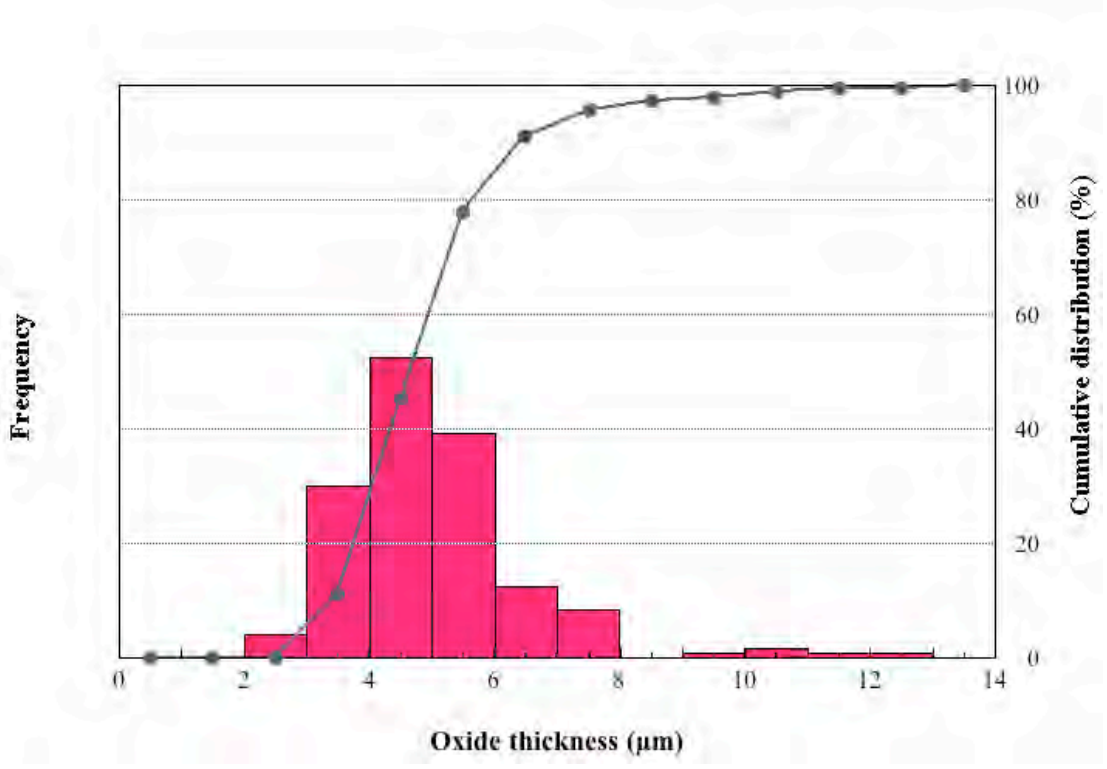

(b) Low pressure plasma sprayed CoNiCrAlY coating

Fig. 3-14 Aluminum oxide film thickness distribution of CoNiCrAlY coatings on specimens aged for 100 hours at 1100℃ (a): cold-sprayed coating, (b): low-pressure plasma-sprayed coating.

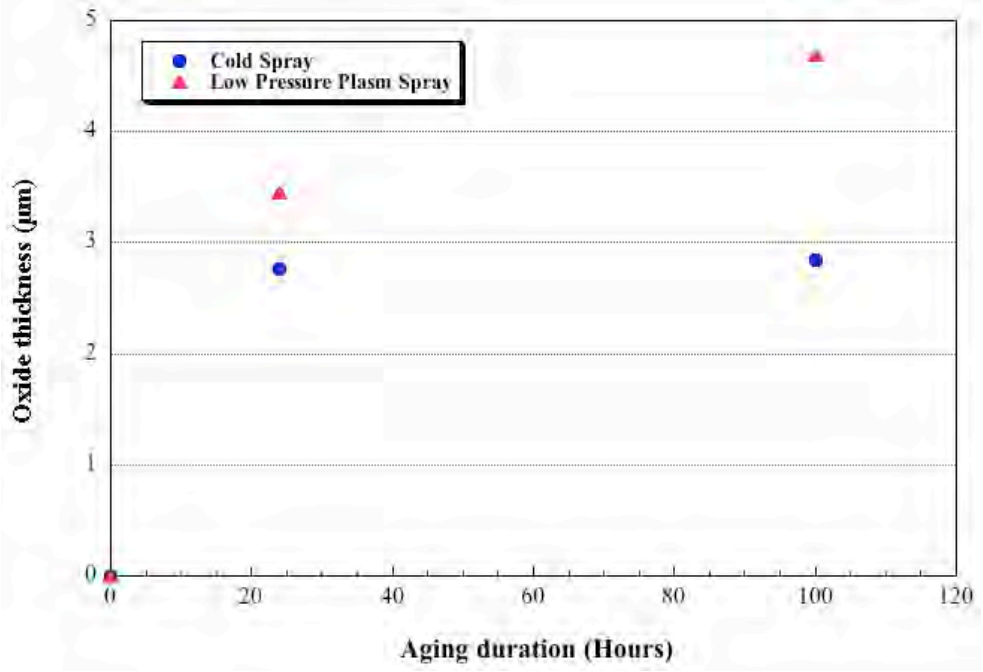

Fig. 3-15 Relationship between aluminum oxide thickness and aging duration for cold-sprayed and low-pressure plasma-sprayed CoNiCrAlY coating in 1100 ℃ atmospheric environment.

3.4 Summary

In order to determine the mechanical properties of coatings and characterize the cold-spray coating, porosity measurements and hardness tests were carried out. In addition, in order to obtain an understanding of the high-temperature oxidation behavior of cold-sprayed CoNiCrAlY coatings, high-temperature exposure tests were carried out. The main results obtained from this chapter can be summarized as follows:

- From the results of porosity measurements, the coating density of the cold-sprayed CoNiCrAlY coating is greater than that of the low-pressure plasma-sprayed coating.
- From the results of hardness tests of the cold-sprayed coating, one can conclude that the distance from the interface has no influence on the. The hardness distribution range of the cold-sprayed coating was narrower than that of the low-pressure plasma sprayed coatings.
- Results of EDX analyses on high-temperature exposure tested specimens showed that the spray method has negligible effects on the Co diffusion depth and tendency have during high temperature operation.
- From the results of EDX elemental mapping of the TGO layer of coatings exposed for 100 hours at high temperature, it can be seen that cold-sprayed MCrAlY coatings have a lower oxidation ratio than that of low-pressure plasma-sprayed coatings in this environment, as cold-sprayed coatings are denser than the low-pressure plasma sprayed coatings. Therefore, the cold-sprayed coating technique improves the high-temperature oxidation behavior of the MCrAlY coatings.

References

[3-1] A. Gil, V. Shemet, R. Vassen, M. Subanovic, J. Toscano, D. Naumenko, L. Singheiser, and W.J. Quadakkers: Effect of surface condition on the oxidation behaviour of MCrAlY coatings, Surf. Coat. Technol. 201 (2006) pp. 3824–3828.

[3-2] W. Brandl, D. Toma, J. Krüger, H.J. Grabke, and G. Matthaus: The oxidation behaviour of HVOF thermal-sprayed MCrAlY coatings, Surf. Coat. Technol. 94–95 (1997) pp. 21-26.

[3-3] W. Brandl, D. Toma, and H.J. Grabke. The characteristics of alumina scales formed on HVOF-sprayed MCrAlY coatings, Surf. Coat. Technol. 108–109 (1998) pp. 10-15.

[3-4] D. Toma, W. Brandl and U. Koster: Studies on the transient stage of oxidation of VPS and HVOF sprayed MCrAlY coatings, Surf. Coat. Technol. 120–121 (1999) pp. 8–15.

[3-5] W. Brandl, H.J. Grabke, D. Toma, and J. Krüger. The oxidation behaviour of sprayed MCrAlY coatings Surf. Coat. Technol. 86–87 (1996), p. 41.

[3-6] J.H. Sun, E. Chang, C.H. Chao, M.J. Cheng, Spalling modes and degradation mechanism of ZrO_2-8 wt.% Y_2O_3/CVD-Al_2O_3/Ni-$_{22}$Cr-$_{10}$Al-1Y thermal-barrier coatings, Oxidation of Metals 40 (5-6)(1993) pp.465-481.

[3-7] Y.N. Wu, M. Qin, Z.C. Feng, Y. Liang, C. Sun, and F.H. Wang: Improved oxidation resistance of NiCrAlY coatings, Materials Letters 57 (2003) pp.404 – 2408.

[3-8] A. Gil, V. Shemet, R. Vassen, M. Subanovic, J. Toscano, D. Naumenko, L. Singheiser and W.J. Quadakkers: Effect of surface condition on the oxidation behaviour of MCrAlY coatings, Surf. Coat. Technol. 201 (2006) pp.3824-3832.

[3-9] Kh.G. Schmitt-Thomas, and M. Hertter: Improved oxidation resistance of thermal barrier coatings, Surf. Coat. Technol. 120–121 (1999) pp. 84–88.

[3-10] W. Beele, N. Czech, W.J. Quadakkers and W. Stamm: Long-term oxidation tests on a Re-containing MCrAlY coating, Surf. Coat. Technol. 91-95 (1997) pp.11-15.

[3-11] W. Zhou, Y.G. Zhao, W. Li, Q.D. Qin and S.W. Hu, B. Tian: Degradation formula and working lifetime prediction for high-temperature coating, Applied Surface Science 253 (2006) pp.2565–2571.

4 SEM Analyses of Deposited Particles

4.1 Introduction

An understanding of the deposition conditions of an individual impinged particle is one of the important approaches for the elucidation of the cold spray mechanism. Therefore, cross-sectional SEM analyses of the interface between an individual deposited particle and the substrate were carried out. Cross-sectional observation required cutting and polishing of the specimens. In this study, however, the deposited particle size ranges from almost 5 μm to 30μm. Therefore, it is difficult to obtain a particle cross-section by cutting and polishing. In this study, a Focused Ion Beam (FIB) system was used to fabricate the cross-section of a deposited particle.

FIB has been widely used for manufacturing and characterization of nano- to micro-scale structures, such as next-generation microelectronic devices [4-1], Micro Electro Mechanical Systems (MEMS) [4-2, 3], novel materials [4-4, 5], manufacturing of scanning probe tips [4-6, 7], transmission electron microscope (TEM) sample preparation [4-8], failure analysis of semiconductor devices [4-9, 10], integrated circuit device repair [4-11], mask-less focused ion beam lithography [4-12], and ion-beam-assisted deposition [4-13].

The fundamental principle of FIB systems is comparable to that of the scanning electron microscope (SEM). However, instead of an electron beam, a finely focused beam of ions with a diameter down to approx. 5 nm is applied in FIB. The FIB mainly comes from an ion source: the Liquid Metal Ion Source (LMIS). The feature of LMIS are high brightness, high emission current density per unit solid angle, which allows a sufficient amount of current to be focused into a small beam (hundreds of pA) for ion-solid interactions to be effective. The source material must have a high surface tension and a low vapor pressure at the melting point. Generally, Ga (melting point: 29.75 ºC) is used for LMIS.

When 30 keV Ga^+ ions hit the sample surface, ion sputtering occurs. Atoms from the sample, in different species (neutral, ions, meta-stable), are removed from the surface region as a result of the collision process generated by the incoming ion beam. Fig. 4-1 shows a schematic illustration of ion sputtering. A sputtering process with ion beams of nanometer size is the basis of FIB machining and patterning at nano-scale accuracy. Secondary electrons are also produced in the ion beam-sample

interaction process. Detected secondary ions are used to obtain a Scanning Ion Microscopy (SIM) image of the surface.

Using FIB cutting for the cold particles deposited by cold spraying, a cross-sectional observation specimens were obtained of the interface between particle and substrate, and between a particle and the adjacent particle. Using the results of cross-sectional SEM analyses, the deformation and deposition phenomena are discussed in this chapter.

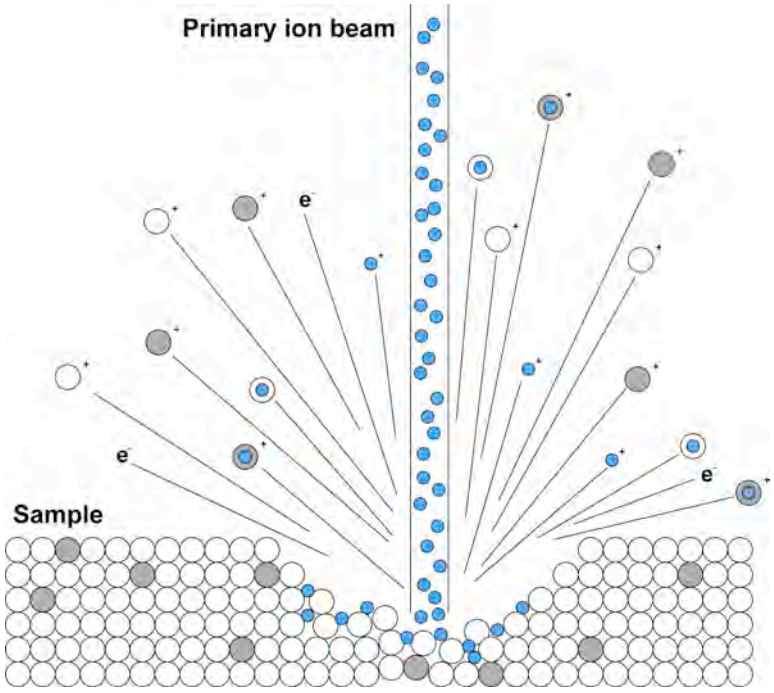

Fig. 4-1 Schematic illustration of ion sputtering.

4.2 Experimental

4.2.1 Specimens

The specimens used are the same as those discussed in Chapter 2. The sparse particle deposited specimens, which were used for the discussion of particle deposition efficiency, were used for the observations in this part of the work. The details of the spray conditions have already been described in Chapter 2. The Ni-base superalloy INCONEL 625 was used as the substrate material. Prior to spraying, the substrate material was polished with waterproof abrasive paper (#320 to #1500) and mirror-polished with colloidal silica. The appearance of the specimens observed by SEM is shown in Fig. 4-2, and a higher-magnification observation of the deposited particles is shown in Fig. 4-3.

4.2.2 SEM sample preparation by FIB

In this study, a FIB (Hitachi, FB-2000A) was used to fabricate a cross-sectional specimen of a deposited particle. The FIB is capable of pinpoint analysis and extremely precise cutting of the order of a few nm. The specimen fabricated using FIB specimen is shown in Fig. 4-4. This figure was observed from a 45 º oblique direction as shown in the cross-sectional schematic illustration in Fig. 4-5. The cross-section of the interface between the deposited particle and the substrate was observed.

Fig. 4-6 shows a schematic illustration of cold spraying and the cutting position of the cross-sectional specimen. All of the observed particles were located to the left of the spraying center and the observation direction is from below to above in this illustration. Therefore, all of the particles impinged from the upper right to lower left direction on the SEM image.

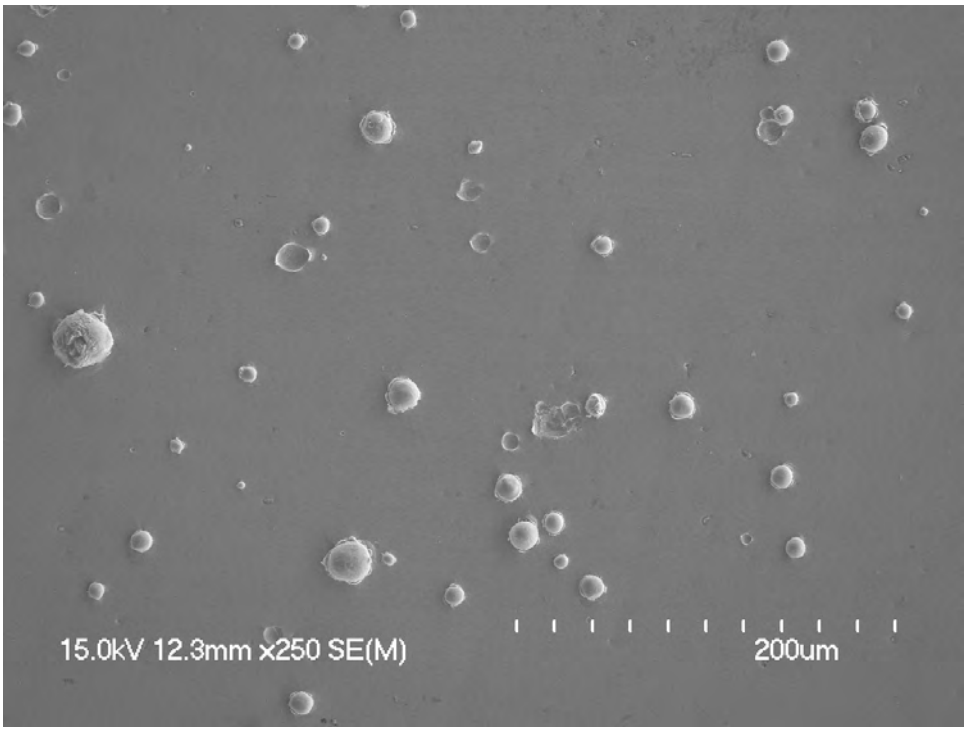

Fig. 4-2 Appearance of sparse particle deposited specimen.

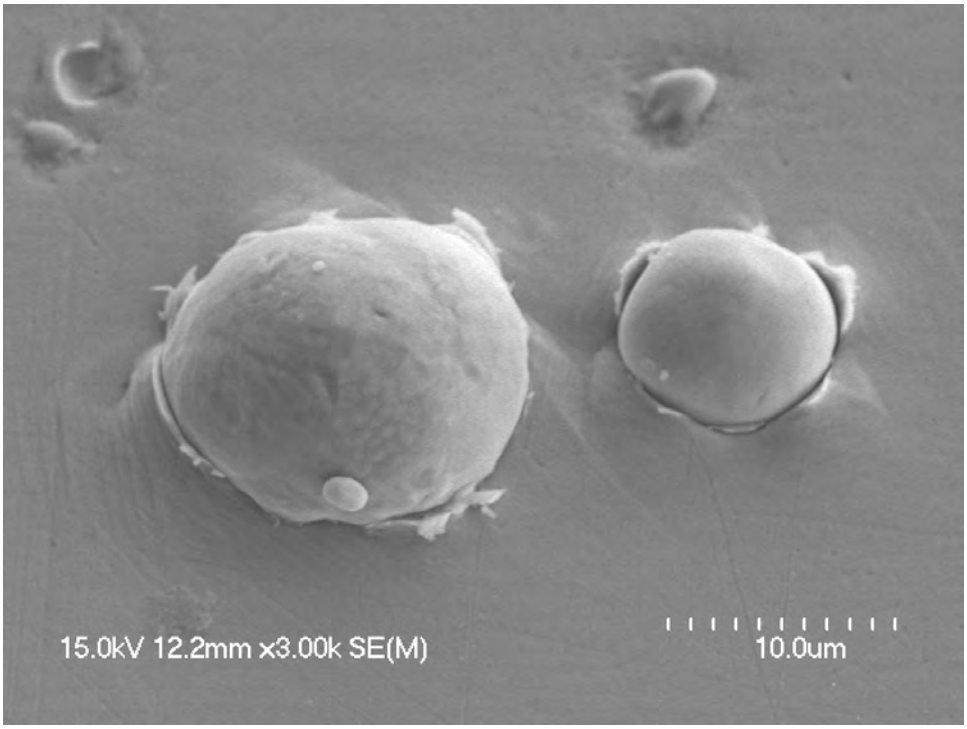

Fig. 4-3 Example of deposited particles.

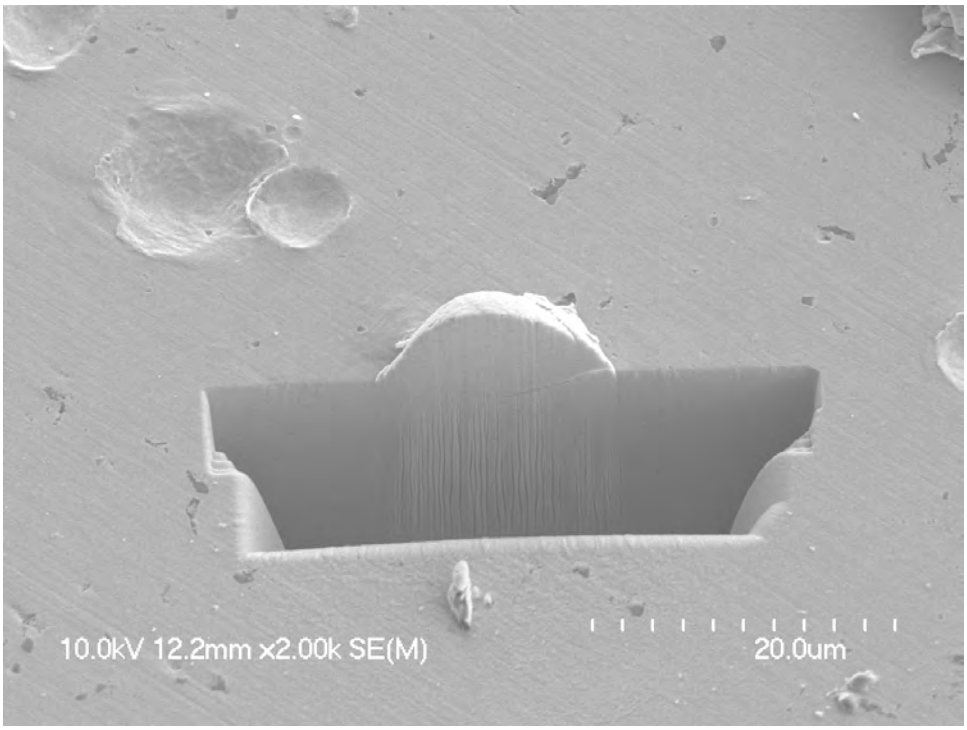

Fig. 4-4 Appearance of FIB specimen fabrication position.

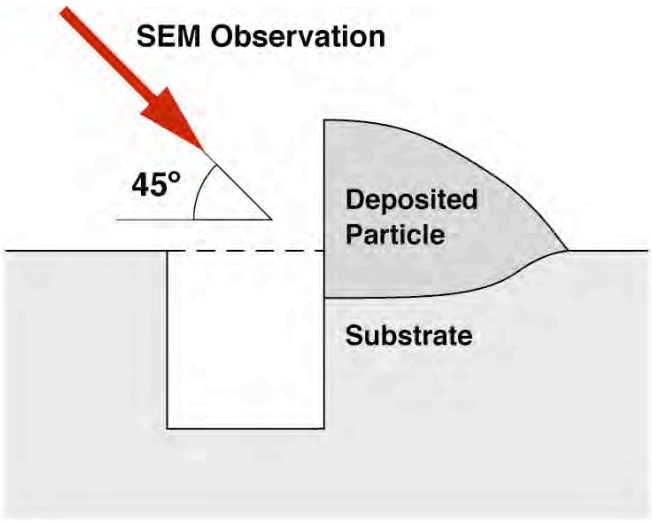

Fig. 4-5 The angle for SEM observation of FIB fabricated deposited particle/substrate interface.

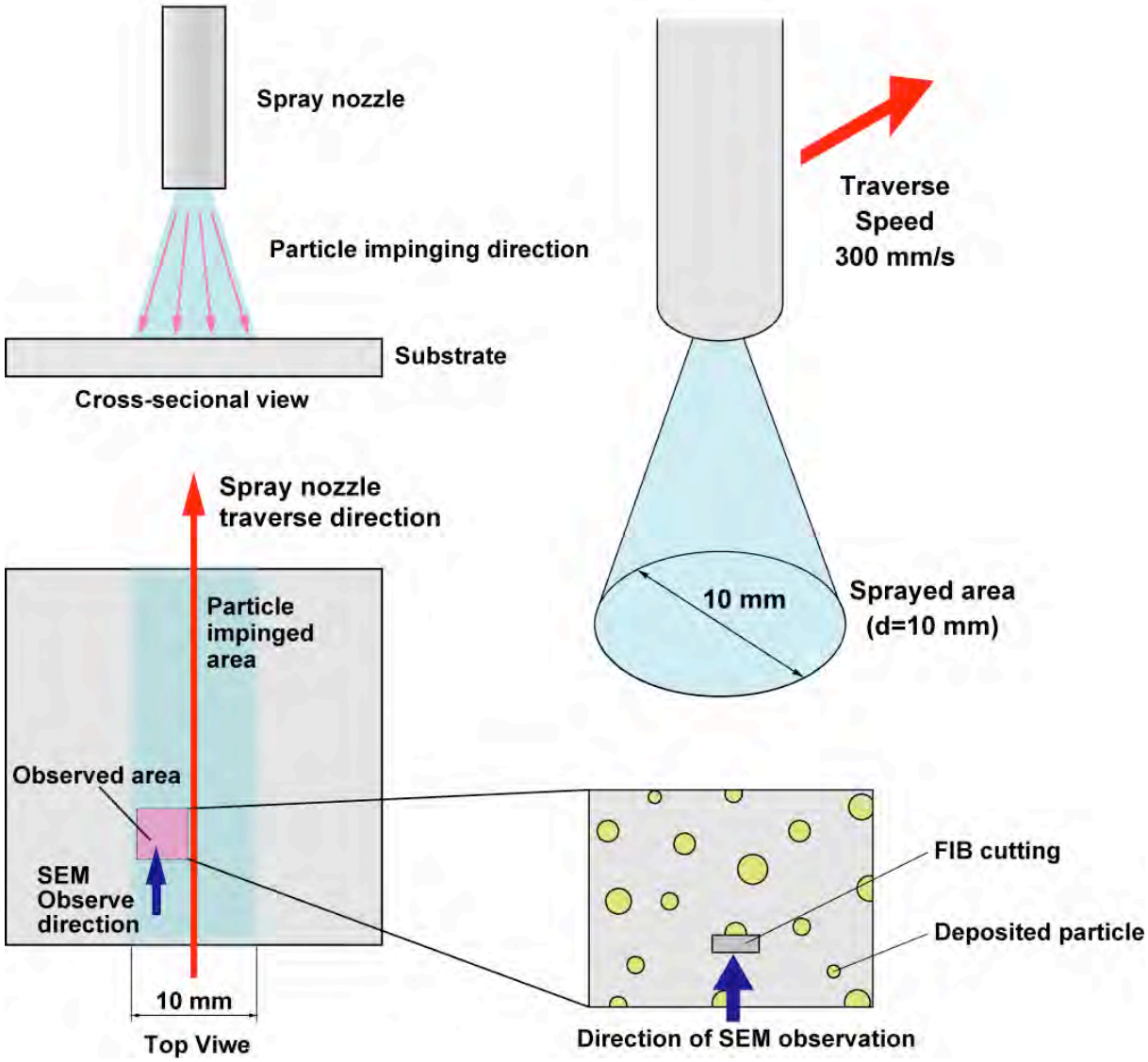

Fig. 4-6 Schematic illustration of cold spraying and cutting position of cross-sectional specimen.

4.3 Results and Discussion

Figures 4-7 to 9 show cross-sectional SEM images of several deposited particles. In the single deposited particle, which is shown in Fig. 4-7, the left-hand side of the interface between particle and interface was strongly in contact. However, the right side was open. The open area of interface might have contacted and plastically deformed, because the interface shape of the particle side corresponds to that of the substrate. Sometimes an impinged particle can rebound. If the adhesion force is larger than the rebound force, the particle is deposited on the substrate. This particle impinged from the upper right direction to the lower left direction. Therefore, the left-hand side of the particle was at the center of the impinging point and this part has stronger adhesion. However, the adhesion force of the right-hand part was not enough for strong attachment, and the rebound force opened the interface at the right-hand side. In the actual cold spay process, the particle impingement direction is not uniform, and the size of the particles and their impinging velocity vary widely. Therefore, an actual cold-sprayed coating may be incompletely deposited in the same way as the particle in Fig. 4-7.

Figure 4-8 shows a cross-sectional SEM image of two overlapping particles. The particle numbers in the schematic illustration indicate the order of impingement. Under the testing conditions, the spray area was a circular shape of approximately 10 mm in diameter and the traverse speed was 300 mm/s. The delay between the impacts of the two overlapped particles was less than 0.03 second. The interface between the first deposited particle and the substrate has complete adhesion. On the other hand, the second deposited particle has a similar interface as that seen in Fig. 4-8. It was considered that the reason for the difference in interface was the following mechanisms. Even though the first particle was deposited, the interface between first particle and substrate had not completely closed. After a very short time, the second particle was deposited on the substrate or on the already-deposited first particle. If the particle hits the substrate on the first particle, the resulting impact can cause the open interface to be closed. The follow-on particles can thus improve the adhesion force at the interface.

Figure 4-9 shows a cross-sectional SEM image of three overlapped particles. The first and second particles have good deposition at the interface, however the deposition of the third particle is not good. The reason for the difference in deposition is the same as in the case of two particles. In this image, the right-hand part, which is the interface between the third particle and the substrate, was not well deposited. However, the most strongly deposited area is the edge of the interface between third particle and first particle. In the case of particle impinging on rough surface as well as impinging on the past-deposited particles, the particle deformation behavior so much more complicated than the impinging on polished surface. The third particle in Fig. 4-9 was impinged from upper right direction to lower left direction. The most deformed area was the deposited area between third particle and first particle, and hence this area has good adhesion.

In actual cold spraying, particle-impingement phenomena such as the direction, velocity, particle size, etc., are much more complicated. Especially, multiple impingement can improve the adhesion force at the interface between particle and substrate. The complicated multiple impingement leads to good adhesion of the cold-sprayed coatings.

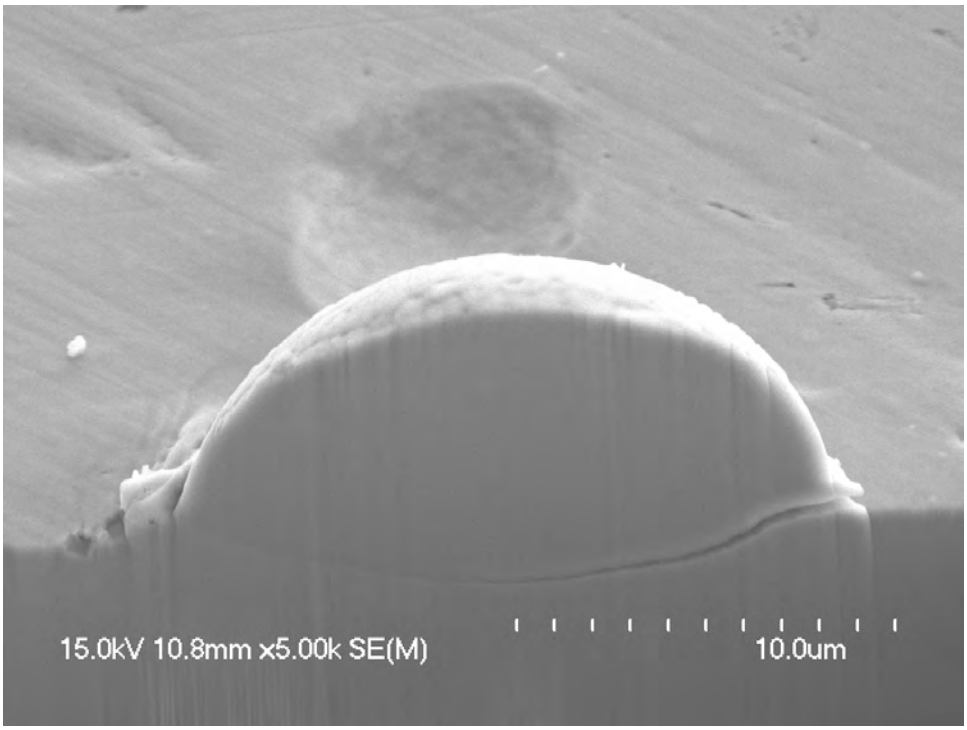

(a) SEM image

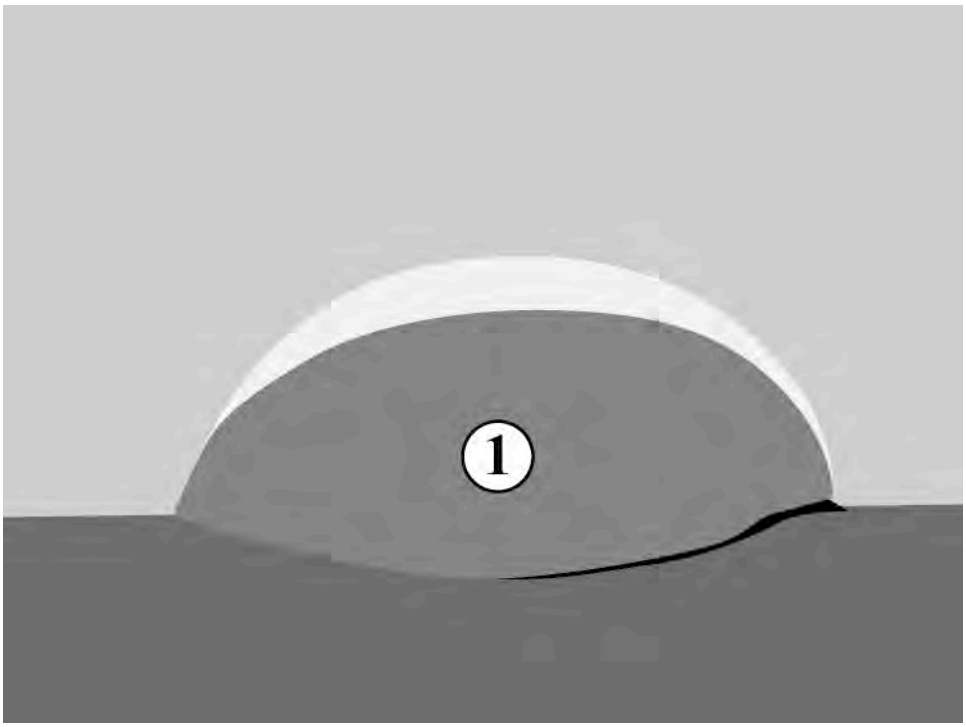

(b) Schematic illustration

Fig. 4-7 Cross sectional SEM observation results and schematic illustration of deposited CoNiCrAlY particle, which deposited on the mirror polished INCONEL 625 substrate.

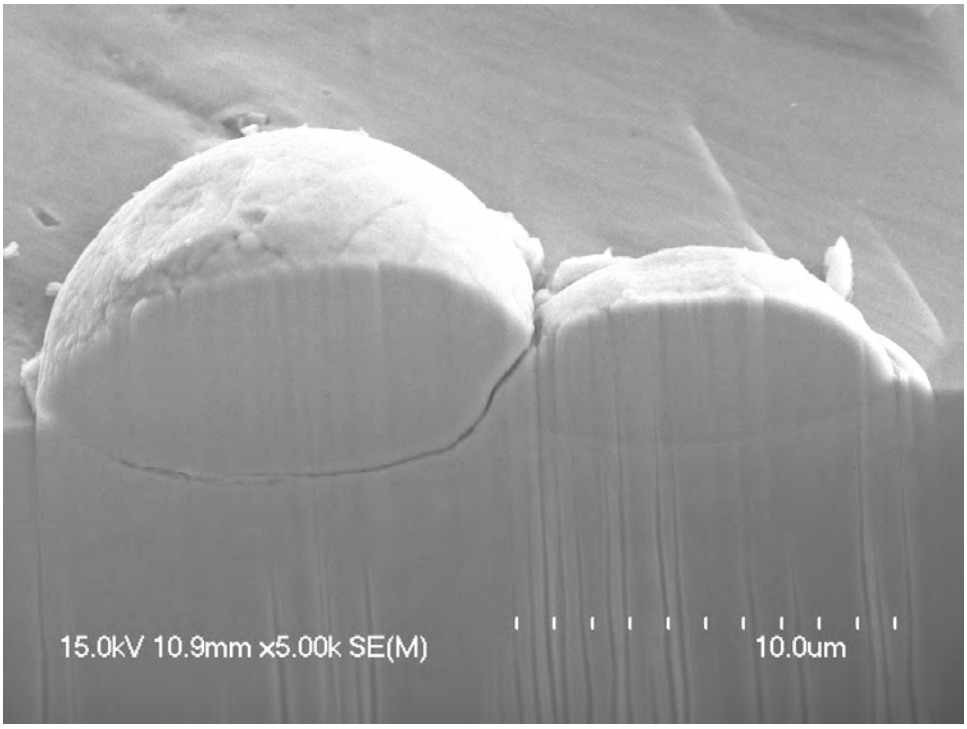

(a) SEM image

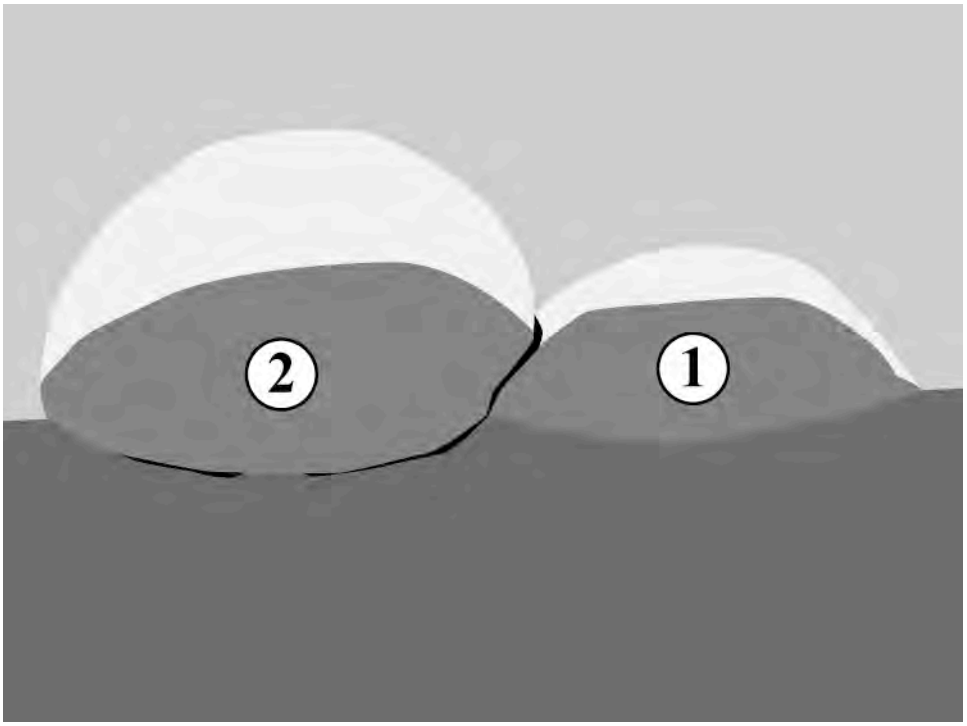

(b) Schematic illustration

Fig. 4-8 *Cross-sectional SEM observation results and schematic illustration of 2 deposited CoNiCrAlY particles, which were deposited on mirror polished INCONEL 625 substrate.*

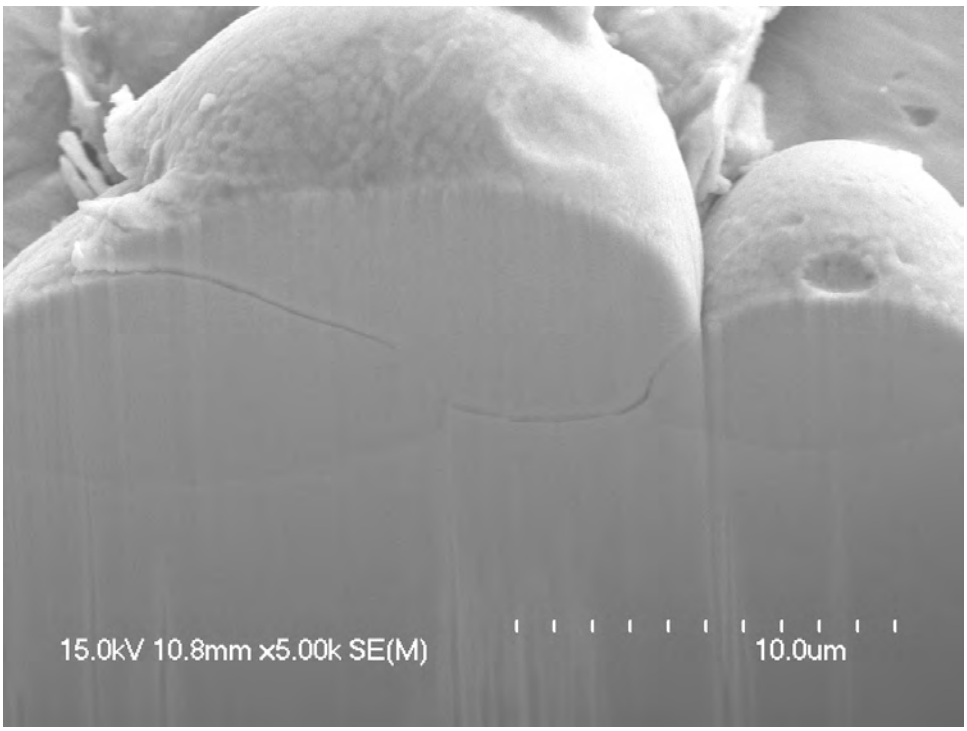

(a) SEM image

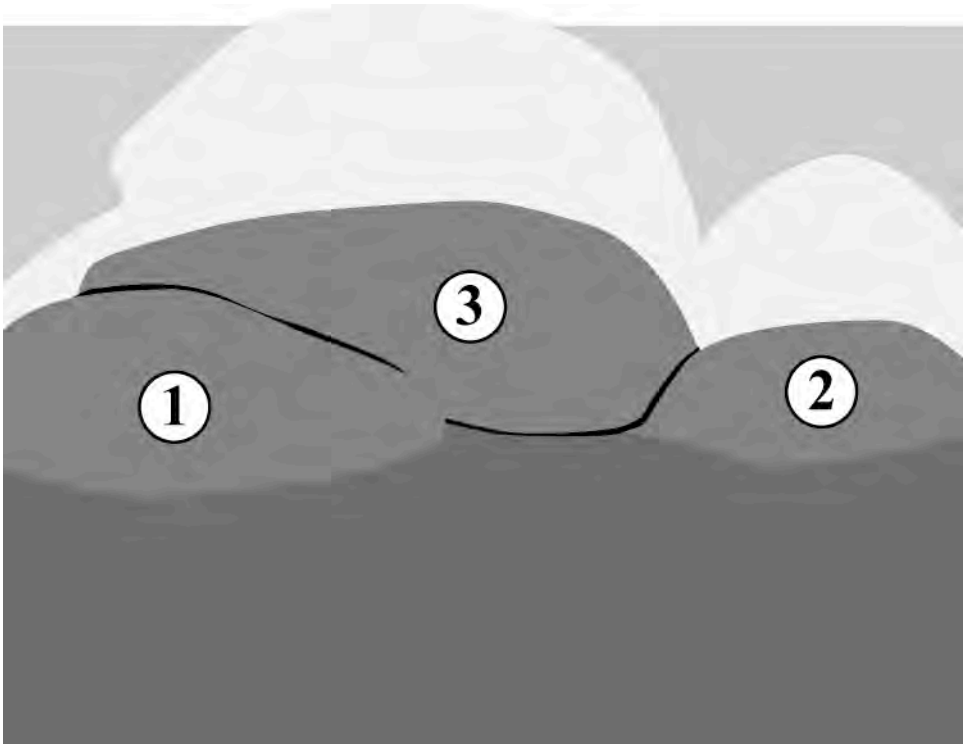

(b) Schematic illustration

Fig. 4-9 *Cross sectional SEM observation results and schematic illustration of 3 deposited CoNiCrAlY particles, which were deposited on mirror polished INCONEL 625 substrate.*

4.4 Summary

In order to understand the deposition conditions of the individual impinged particles, which is one of the most important approaches for elucidation of the cold spray mechanism, this chapter considers SEM cross-sectional analyses of deposited particles, which were fabricated by FIB. The main results obtained from this chapter can be summarized as follows:

- The single deposited particle observed did not have good adhesion but was only partly deposited.
- From the analysis results of two or three overlapped particles, it is shown that the first particle will have better adhesion when it is attacked by the other particles than when it is not followed by any other particles. Impact of other particles on the first particle will result in closure of any open interfaces. Therefore, follow-on particles can improve the adhesion force at the interface.
- In actual cold spraying, particle-impingement phenomena such as the direction, velocity, particle size, were much more complicated. Especially, multiple impingements can improve the adhesion force at the interface between particle and substrate. The complicated multiple impingements gives good adhesion in the cold-sprayed coatings.

References

[4-1] F.A. Stevie, T.C. Shane, P.M. Kahora, R. Hull, D. Bahnk, V.C. Kannan and E. David, Applications of focused ion beam in microelectronics production, design and development. Surf. Interface Anal. 23 (1995) pp. 61–65.

[4-2] T.W. Kim, D.C. Choo, J.H. Shim, and S.O. Kang, Single-electron transistors operating at room temperature, fabricated utilizing nanocrystals created by focused-ion beam. Appl. Phys. Lett. 80 (2002) pp. 2168-2170.

[4-3] G.M. Kim, M.A.F. van den Boogaart and J. Brugger, Fabrication and application of a full wafer size micro/nanostencil for multiple length-scale surface patterning. Microelectr. Engineering 67-68 (2003) pp. 609-614.

[4-4] R. Hull, D. Dunn, New Techniques for the Nanostructural Characterization of Semiconductor Materials and Devices Using Combined Focused Ion Beam and Transmission Electron Microscopy Techniques, 1998 MRS Symposium on Microscopy of Semiconducting Materials, Materials Research Society Symposium Proc. 524 (1998) pp. 141-151.

[4-5] N. Motta, Self-assembling and ordering of Ge/Si(111) quantum dots: scanning microscopy probe studies. J. Phys. Cond. Matter 14 (2002) pp. 8353-8378.

[4-6] A. Olbrich, B. Ebersberger, C. Boit, P. Niedermann, W. Hänni, J. Vancea et al., High aspect ratio all diamond tips formed by focused ion beam for conducting atomic force microscopy. J. Vacuum Sci. Technol. B 17 (1999) pp. 1570–1574.

[4-7] J.R. Krogmeier, R.C. Dunn, Focused ion beam modification of atomic force microscopy tips for near-field scanning optical microscopy Appl. Phys. Lett. 79 (2001) pp. 4494-4496

[4-8] H. Bender, Focused Ion Beam and Transmission Electron Microscopy for Process Development, Elchem. Soc. Pennington, (1999) pp. 232-247.

[4-9] M. Abramo and R. Wasielewski, FIB for Failure Analysis. Semicond. International, 133 (1997).

[4-10] D. Verkleij, The use of the focused ion beam in failure analysis. Microelectron. Reliab. 38 (1998) pp. 869-876.

[4-11] K.N. Hooghan, K.S. Wills, P.A. Rodriguez and S. O'Connell. Integrated Circuit Device Repair using FIB system : Tips, Tricks, and Strategies, Proc. 25th Int. Symp. f. Test. a. Fail. Anal. Analysis (ISTFA 99), (ASM International, Materials Park, Ohio), (1999) pp. 247-254.

[4-12] J. Melngailis, C.R. Musil, E.H. Stevens, M. Utlaut, E.M. Kellogg, R.T. Post, M.W. Geis and R.W. Mountain, The Focused Ion Beam as an Integrated Circuit Restructuring Tool. J. Vac. Sci. Technol. B 4, (1986) p. 176.

[4-13] E. J. Sánchez, J. T. Krug II, and X. S. Xie, Ion and electron beam assisted growth of nanometric Si_mO_n structures for near-field microscopy. Rev. Sci. Instr. 73, (2002) pp. 3901-3907.

[4-14] J. Melngailis, Focused ion beam technology and applications. J. Vac. Sci. Technol. B, 5 (1987) pp. 469-495.

[4-15] S. Reyntjens, and R. Puers, A review of focused ion beam applications in microsystem technology. J. Micromech. Microeng., 11 (2001) pp. 287-300.

5 TEM and STEM Analyses of the Interface between Cold-Sprayed MCrAlY Coating and Substrate

5.1 Introduction

Transmission electron microscopy (TEM) observation is one of the most important experimental approaches for understanding the bonding mechanism of cold spraying. In the previous chapter, the FIB technique was used for micro-machining with the aim of making a cross-sectional specimen for observation of the deposited particles. The FIB technique allows sectioning of thin samples. Recently, a FIB system equipped with a micro sampling system, which allows site-specific micro samples for TEM observation to be prepared with pinpoint accuracy, has become commercially available [5-1].

In order to understand the mechanisms of deposition by cold spraying, TEM and scanning transmission electron microscopy (STEM) observations and micro-Energy Dispersive X-ray spectrometer (EDX) elementary analyses were carried out. In addition, nano-beam diffraction was used to analyze the orientation relationships between the contacting grains of coating and substrate.

5.2 Experimental

5.2.1 Cold spraying

For TEM and STEM evaluation, specimens were produced using different spray conditions. CoNiCrAlY (SULZER METCO, AMDRY9951) was used as the coating material. The powder was screened before spraying and those particles smaller than 25 μm in diameter were used. The Ni-based superalloy INCONEL 625 with dimensions of 50 × 50 × 4 mm^3 was used as the substrate. This was grit-blasted with 300 μm corundum prior to cold spraying. The CoNiCrAlY coatings were sprayed using the KINETIKS 3000 cold-spray facilities at CGT / Linde in Unterschleissheim (Germany). The cold-spray conditions are summarized in Table 5-1.

Table 5-1 Cold spray conditions

Material	AMDRY 9951 CoNiCrAlY
Facility	CGT KINETIKS 3000
Gas	Nitrogen
Gas Pressure	30 MPa
Gas Temperature	520 ℃

5.2.2 TEM and STEM Sample preparation

Cross-sectional TEM and STEM specimens were prepared using Focused Ion Beam (FIB) milling with a microsampling unit (HITACHI FB-2000A) as shown in Fig. 5-1. The specifications for the FIB are shown in Table 5-2. The FIB microsampling technique allows pin-point preparation of STEM samples from a desired area of a bulk specimen [5-1 to 3]. A rotational-type side-entry stage was used for the micro fabrication. This stage allows micro-samples to rotate by 360º around the axis of the stage and to be maneuvered in the forward (x) and radial (y) directions as shown in Fig. 5-2. A microprobe attached to the sampling system enables the micro-sample to move in the three directions. A small sample, which includes a coating-substrate interface, 3 μm wide × 15 μm long × 15 μm depth, was lifted out of the block using the microsampling system attached to the FIB, put on a Cu mesh and thinned to less than 100 nm thickness from the perpendicular direction at an accelerating voltage of 30 keV. FIB assisted deposition was used to attach the sample to the microprobe and for bonding the sample with the Cu mesh. $W(CO)_6$ was used as the material of the assist gas. A schematic illustration of the microsampling procedure is shown in Fig. 5-3.

Fig. 5-1 HITACHI FB-2000A FIB system.

Table 5-2 Specifications for FB-2000A FIB system

Accelerating voltage	30 kV
Maximum beam current	13 nA and above
Maximum beam current density	15 A/cm^2 and above
Image resolution	10 nm

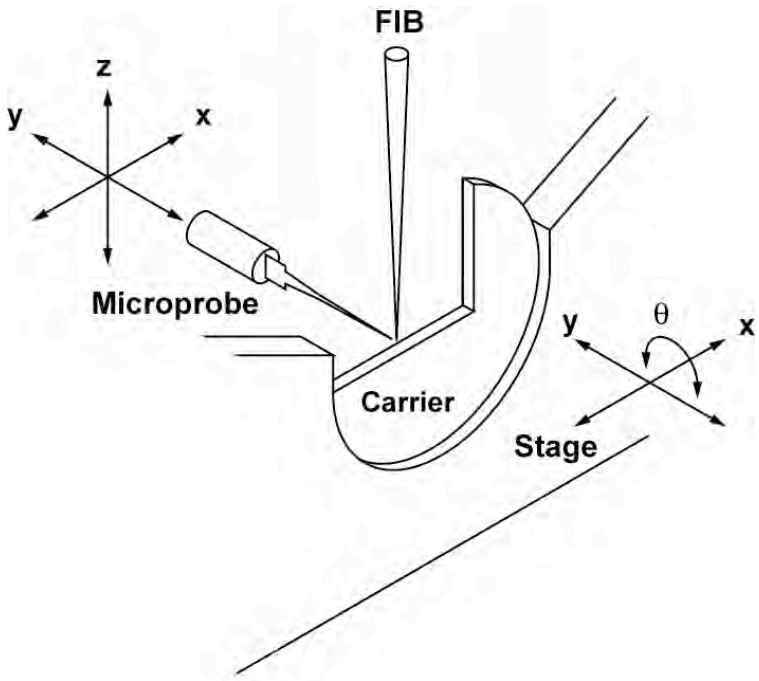

Fig. 5-2 Schematic illustration of a rotational--type side-entry stage and microsampling system [5-3].

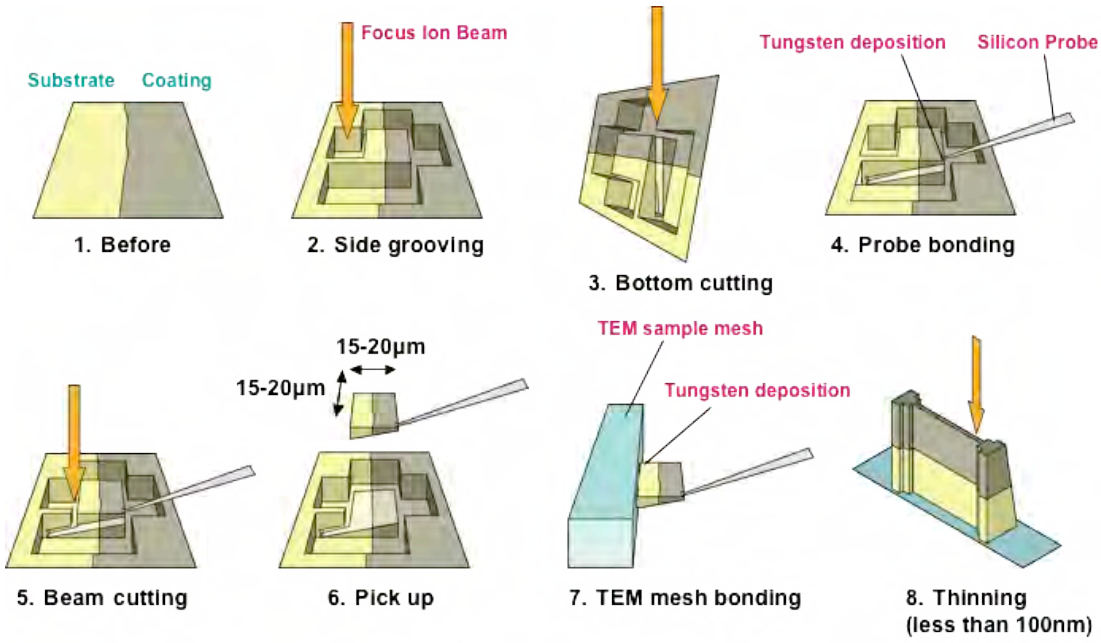

Fig. 5-3 FIB microsampling procedure.

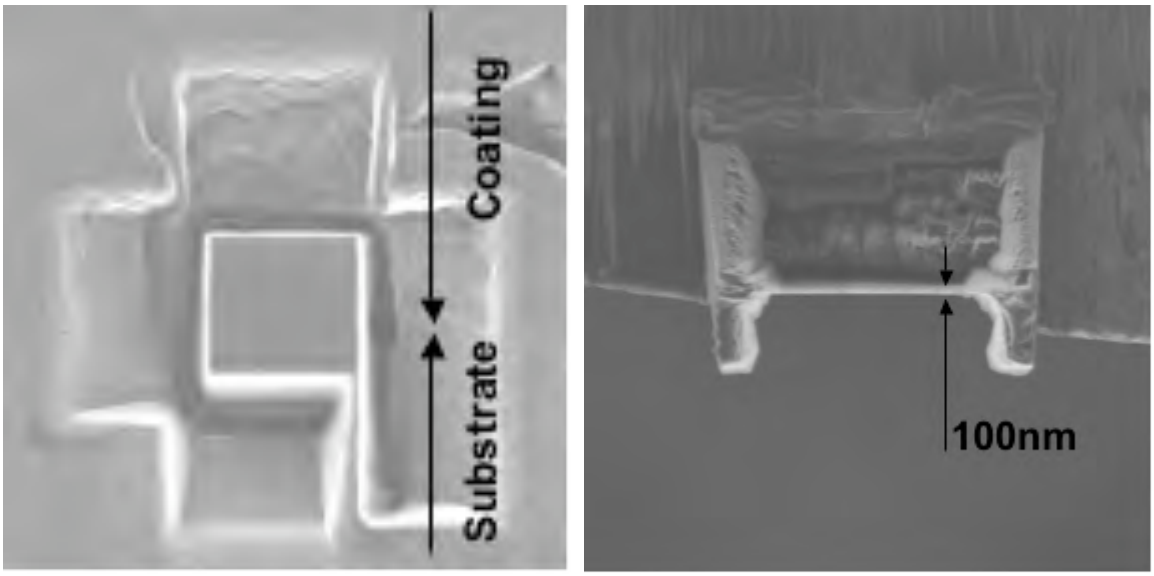

(a) (b)

Fig. 5-4 FIB sample fabrication procedure, (a) side grooved sample corresponding to step No. 2 in Fig. 5-3, (b) picked-up and thinned specimen corresponding to step No. 8 in Fig. 5-3. These images were observed using a scanning ion microscope.

5.2.3 STEM-EDX line analyses

Before TEM observation, in order to identify the phase of CoNiCrAlY attached on the substrate, STEM-EDX analyses were carried out. Scanning Transmission Electron Microscopy (STEM) allows high-resolution imaging and high-sensitivity EDX analysis with 1 nm in resolution. The interface between the as-sprayed CoNiCrAlY coating and the substrate was magnified and observed, and then the material was identified using STEM (Hitachi HF-2000) and micro-energy dispersive spectroscopy (micro-EDX) elemental analysis.

5.2.4 TEM observation

Finally, the interface between the CoNiCrAlY coating and the substrate was evaluated using a transmission electron microscope (TEM) (Hitachi HF-2000) with a micro-EDX system Thin-sectional samples of less than 50 nm in thickness were prepared using the FIB microsampling technique for TEM observation. The observation conditions are shown in Table 5-3.

Table 5-3 TEM observation condition

Facility	HF-2000
Acceleration voltage	200 kV
Camera length	0.20 m
Electron beam wavelength	0.0025 nm
Correction coefficient	0.98

5.3 Results and Discussion

5.3.1 Cold Spraying

Figure 5-5 shows a cross-sectional SEM image of a cold-sprayed CoNiCrAlY coating for TEM and STEM observation. This coating was approximately 100 μm in thickness with a high density similar to that of low-pressure plasma-sprayed coatings.

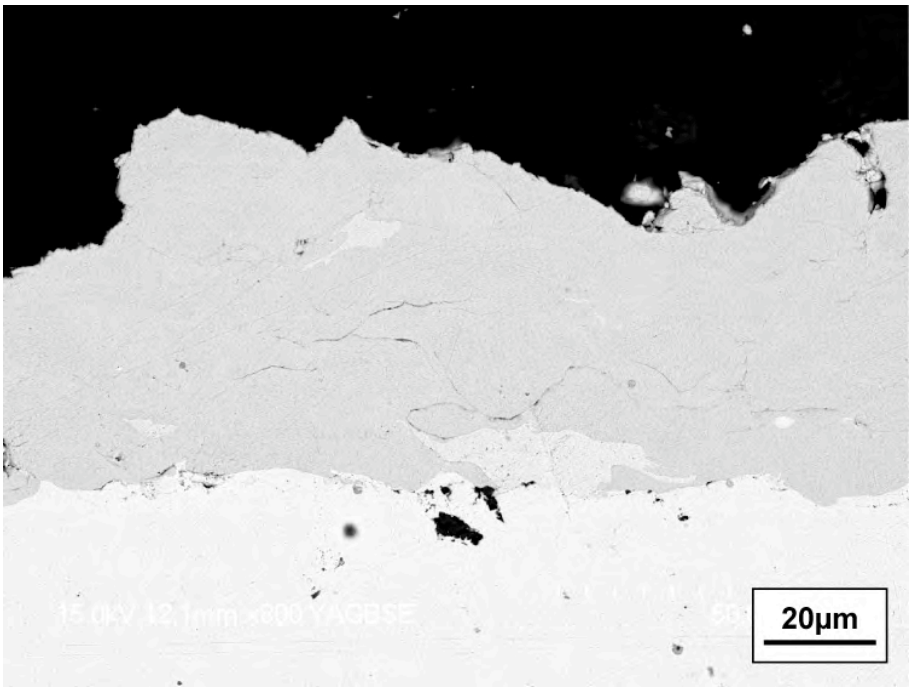

Fig. 5-5 Typical cross-sectional SEM images of a as-sprayed CoNiCrAlY coatings.

5.3.2 STEM-EDX line analyses

Figure 5-6 shows a scanning ion microscope (SIM) image of an STEM specimen of cold-sprayed CoNiCrAlY coating on an INCONEL 625 substrate, which was obtained by FIB. Because of the clear SIM image contrast, it can be concluded that this image shows the interface between the coating and the substrate. It was experimentally observed that the interface between coating and substrate of cold-sprayed coating was densely bonded.

Results of the EDX elemental line analyses are shown in Fig. 5-7. These were obtained along the white line marked with an arrow from position A to B in Fig. 5-6. Concentrations of the elements Co, Ni, Cr, Al and Mo were analyzed. The intensity of Co decreased continuously in the region between 2 μm and 3 μm. Accompanying this decrease was an increase in the intensity of Ni. These continuous changes are most likely due to the geometry of the interface, which was not perpendicular to the observation direction. Al is only present in the CoNiCrAlY coating. A decrease in Al was observed at an earlier position comparing to the decrease in Co. Thus, it was concluded that Al was depleted at the interface. Therefore, the Al depletion suggests that the bonded material at the interface was the γ/γ'-(Ni/Ni_3Al) phase of CoNiCrAlY, which contains a relatively small amount of Al. Within the substrate (near the 4.5 μm region) a decrease in Ni and Mo was observed. The decrease in this region may be attributed to the deposition occurring in a specific phase during cold spraying.

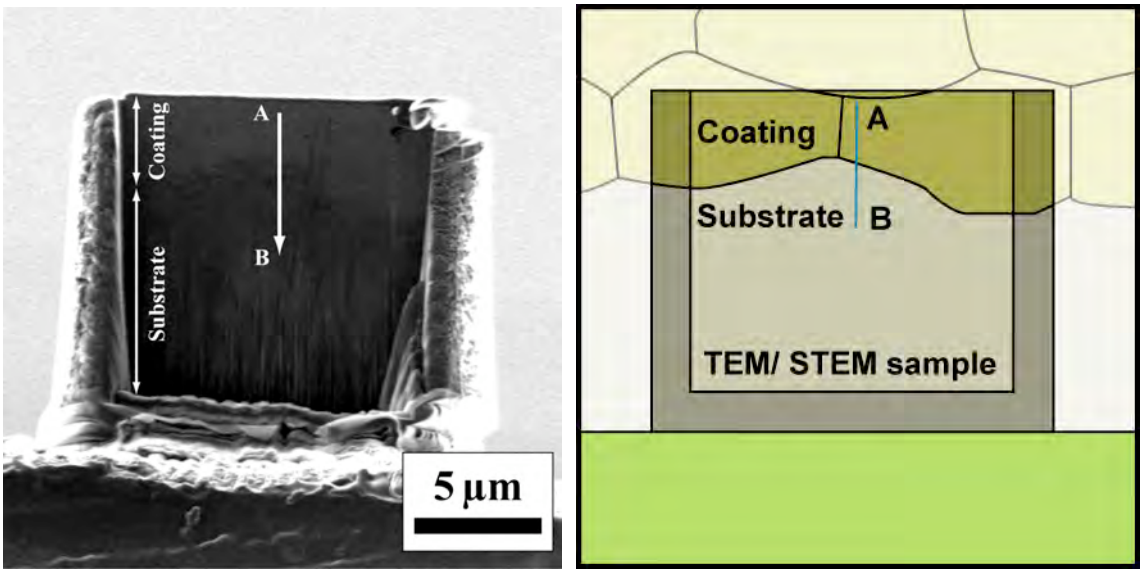

Fig. 5-6 Scanning ion microscope (SIM) image of TEM/STEM sample of cold-sprayed CoNiCrAlY coating on INCONEL 625 substrate sample prepared and imaged by FIB.

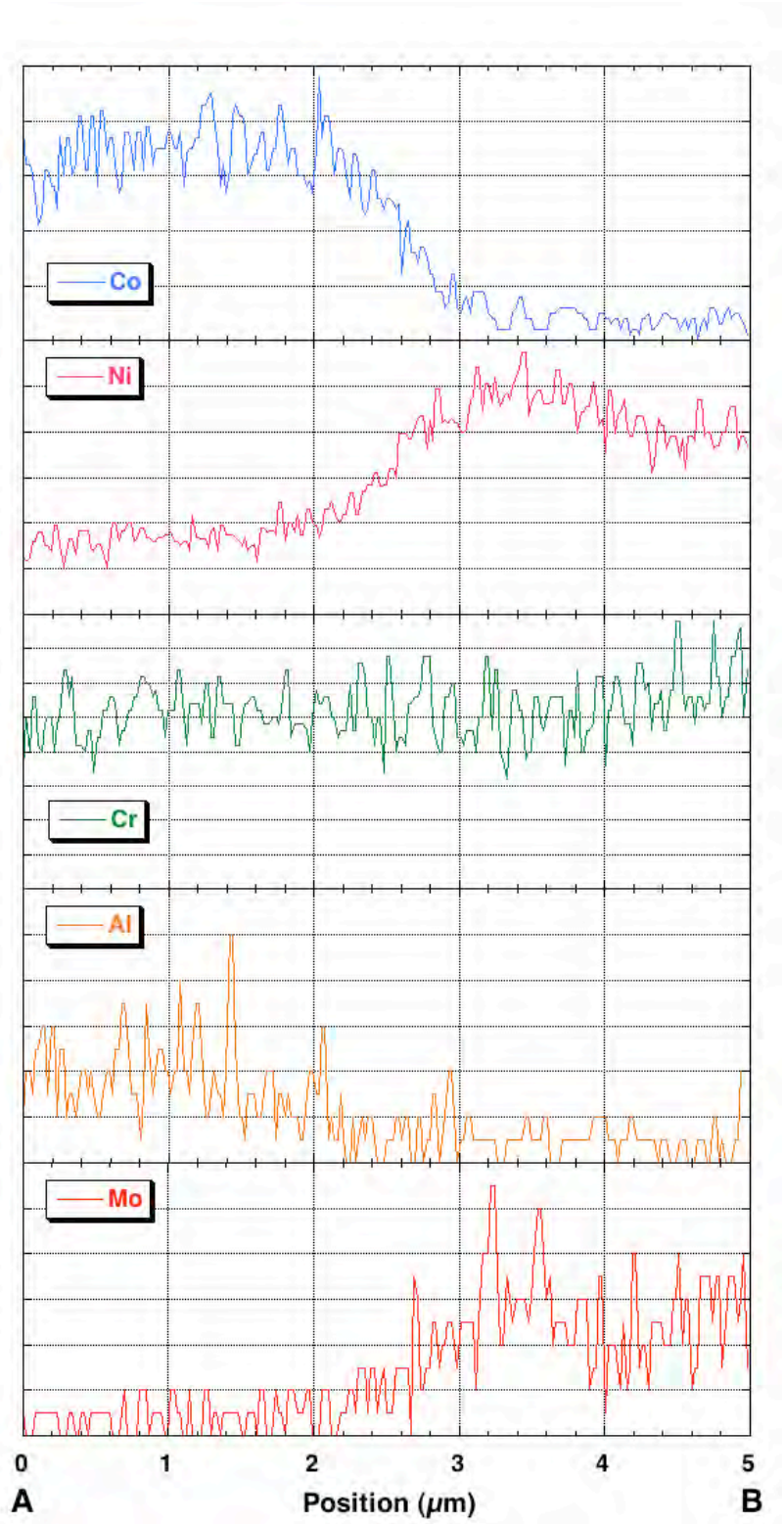

Fig. 5-7 STEM-EDX line elemental analysis results in the interface region between cold-sprayed CoNiCrAlY coating and INCONEL 625. Evaluation of Co, Ni, Cr, Al, and Mo.

5.3.3 Results of TEM and EDX analyses

Figures 5-8, 9 show the results of TEM observations of the interface between the cold-sprayed CoNiCrAlY coating and the substrate. The coating-substrate interface was located at the center of the TEM images. At the center of the images, a white line is observed, and this separated areas of different image contrast. Therefore, it was assumed that the white line was the interface.

EDX point analyses were performed above and below the white line and on the interface. The measured points are indicated by the positions A to H in Fig. 5-9. The beam spot diameter was approximately 5 nm. EDX analyses at points A and B, which are indicated by a blue line in Fig. 5-9 (a) and (b), were identified as the CoNiCrAlY coating, because of the strong peak of Co identified. The positions G and H were identified as the INCONEL substrate using the results from Fig. 5-9 (g) and (h). The thickness of the interface, that is 0.8 nm to 3 nm, is smaller than the EDX beam diameter, and hence we could not obtain a signal from only the interface. The results of Fig. 5-10 (c), (d), (e) and (f) include information from adjacent areas. However, the results of Fig. 5-10 (c), (d), (e) and (f) indicate the both elements of coating and substrate. Therefore, measurement around the interface includes the interface between the coating and substrate. Moreover, because of the Fig. 5-10 (c), (d), (e) and (f) indicate an oxygen peak, the interface is an oxide film. Come back

Since the as-received CoNiCrAlY powder was produced by gas atomization, the grain size is equal to the particle size. In this study, the as-received grain size is approximately 5 to 30 μm. However, the TEM image shows that the grain size within the interface is several dozens of nm. The grain size miniaturization was caused by high-speed plastic deformation during the cold spraying process.

Results from extensive observations indicate that most parts of the interface were covered with oxide film. However, areas without oxide covering were found intermittently, such as the right-hand part of the EDX position C at the Fig. 5-9. An oxide film is not, and the grain overlaps the coating and substrate at these positions. More specifically, intermittent adhesion between coating and substrate occurred at these positions.

The oxide film may be a natural oxide film. Generally, natural oxide films, typically of order of few Å to few nm in thickness, grow and cover the metallic materials in an air environment. The plastic deformation of the splat and substrate fracture the natural oxide film during the spraying process. A fractured area, which is not covered with oxide film, is called a nascent metal surface.

Understanding the bonding conditions among nascent metal surfaces is most important for elucidating the deposition mechanisms of cold spraying. In order to determine their bonding condition, nano-beam diffraction (NBD) patterns of contacting grains were taken and the bonding mechanisms discussed.

Figure 5-11 shows the NBD patterns and measured point TEM images. These measured points correspond with the two contacting two grains which are located at the right part of the EDX position C at the Fig. 5-9. Pattern 1 is from the grain of the coating; Pattern 2 is from the grain of the substrate. From the result of the STEM-EDX, the contacting CoNiCrAlY phase may be Ni_3Al, and the substrate is γ-Ni. Both phases have face-centered cubic (fcc) lattice structures. The lattice constants of Ni_3Al and γ-Ni are 3.5238 Å and 3.5748 Å, respectively. These NBD patterns show the bonded surfaces of this interface are (311) of Ni_3Al and (1-11) of γ-Ni. Because Ni_3Al and γ-Ni ohave similar lattice structures, this combination gives high coherency. Therefore, even though bonding of (311) in Ni_3Al and (1-11) in

γ-Ni is not the best possible bonding condition, this combination has good adhesion, similar to that at a grain boundary.

More specifically, actual bonding of the cold-sprayed coating and the substrate occurred at contacts with nascent surfaces. The nascent surfaces are clean without any contamination. Among nascent metal surfaces, contacting interfaces may be similar to grain boundaries. Therefore, the lattice orientation was not an important factor in bonding phenomena. However, a better orientation relationship makes for stronger bonding, the grain structure relationship having an influence on the adhesion strength and difficulty of deposition. A summarized schematic illustration of bonding interface is shown in Fig. 5-12.

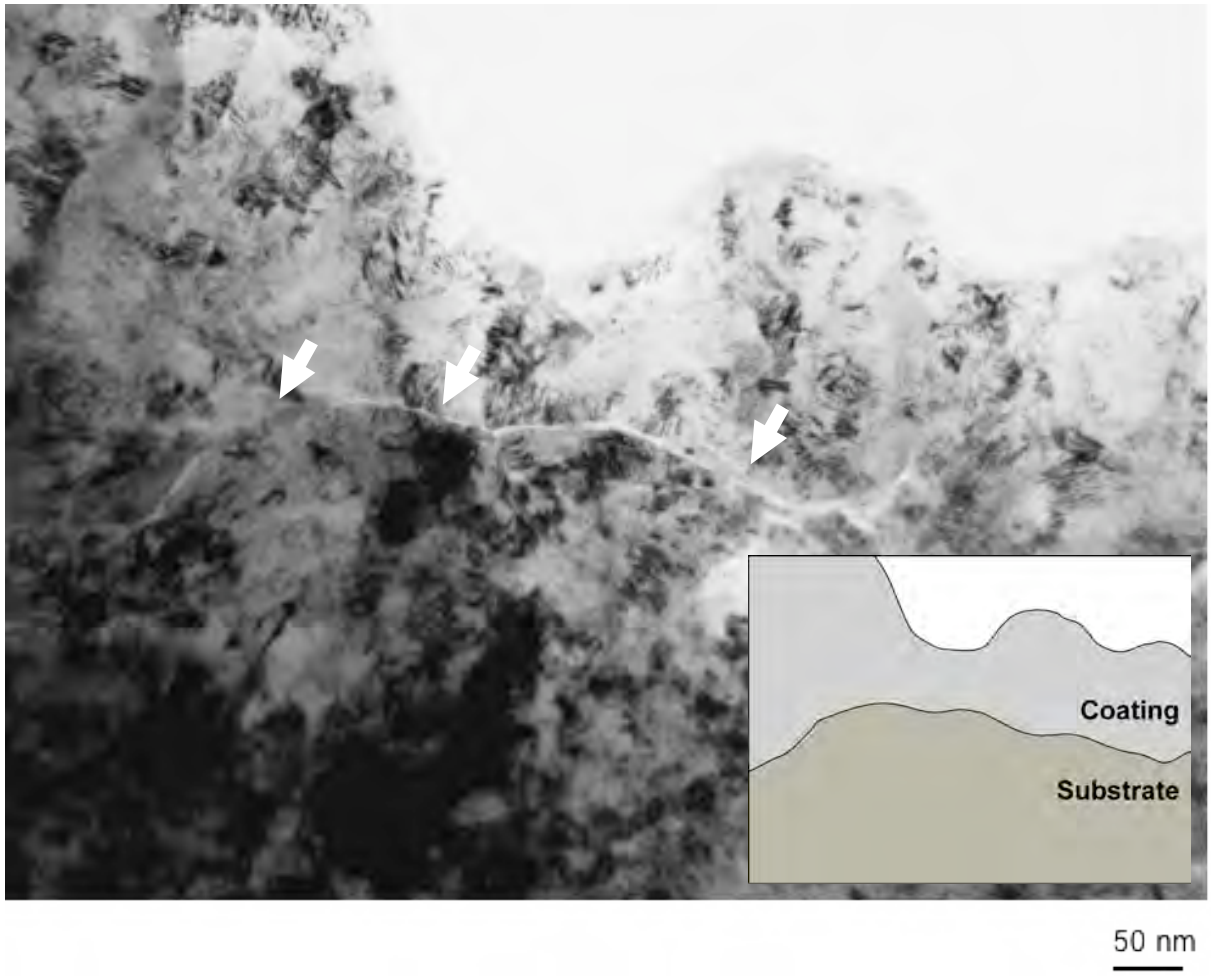

Fig. 5-8 TEM image of coating/substrate interface of as-sprayed CoNiCrAlY cold-sprayed coating (arrow indicates the interface).

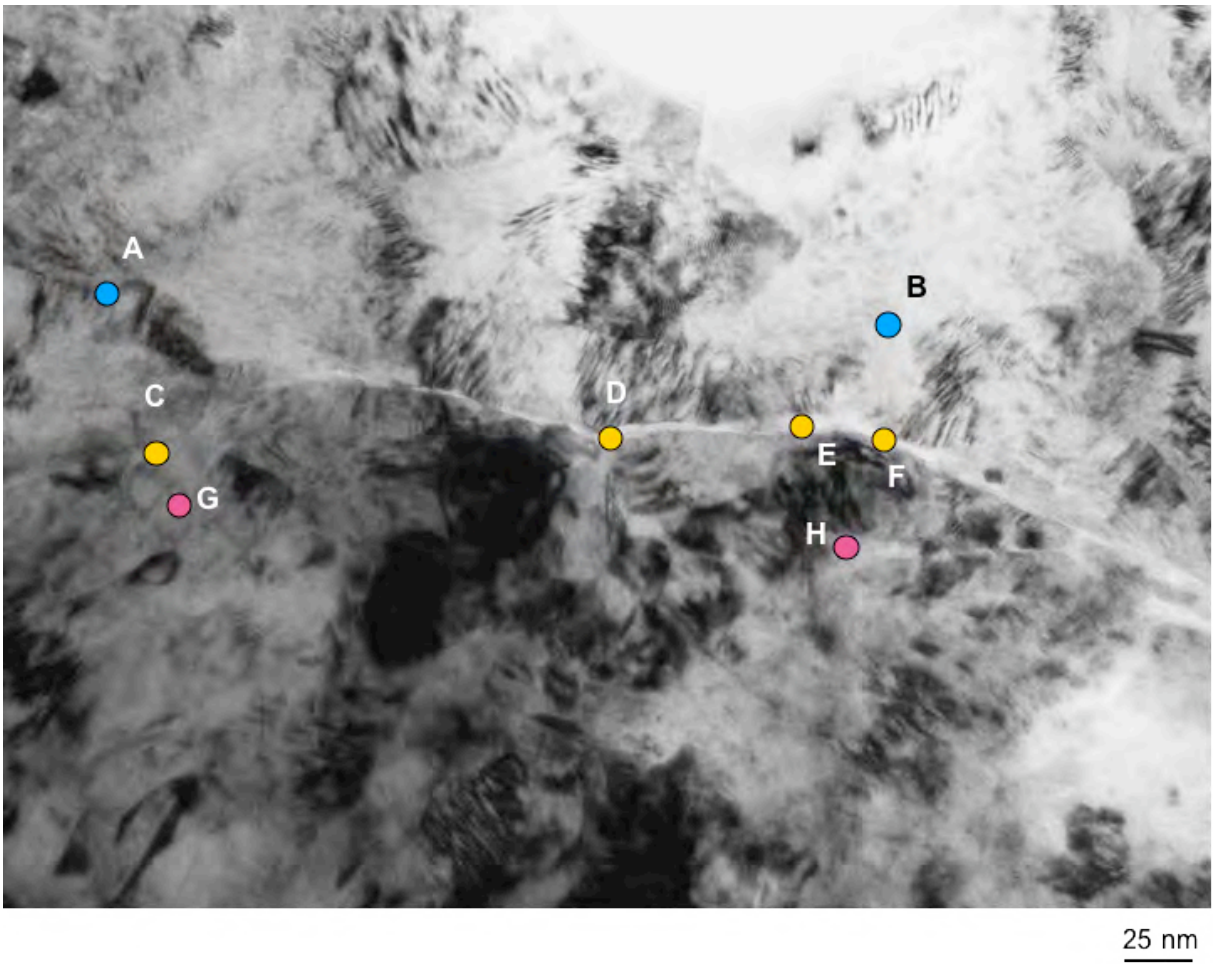

Fig. 5-9 TEM image of coating/substrate interface and EDX analysis positions.

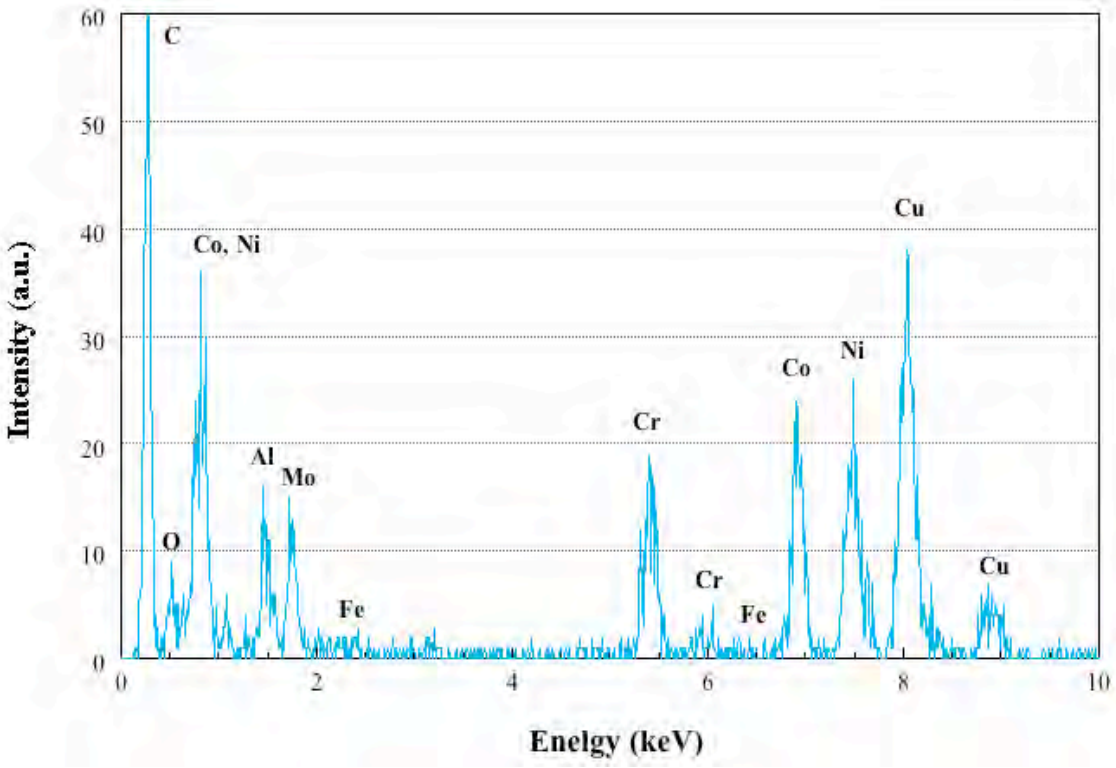

(a) Position "A" at Fig. 5-9

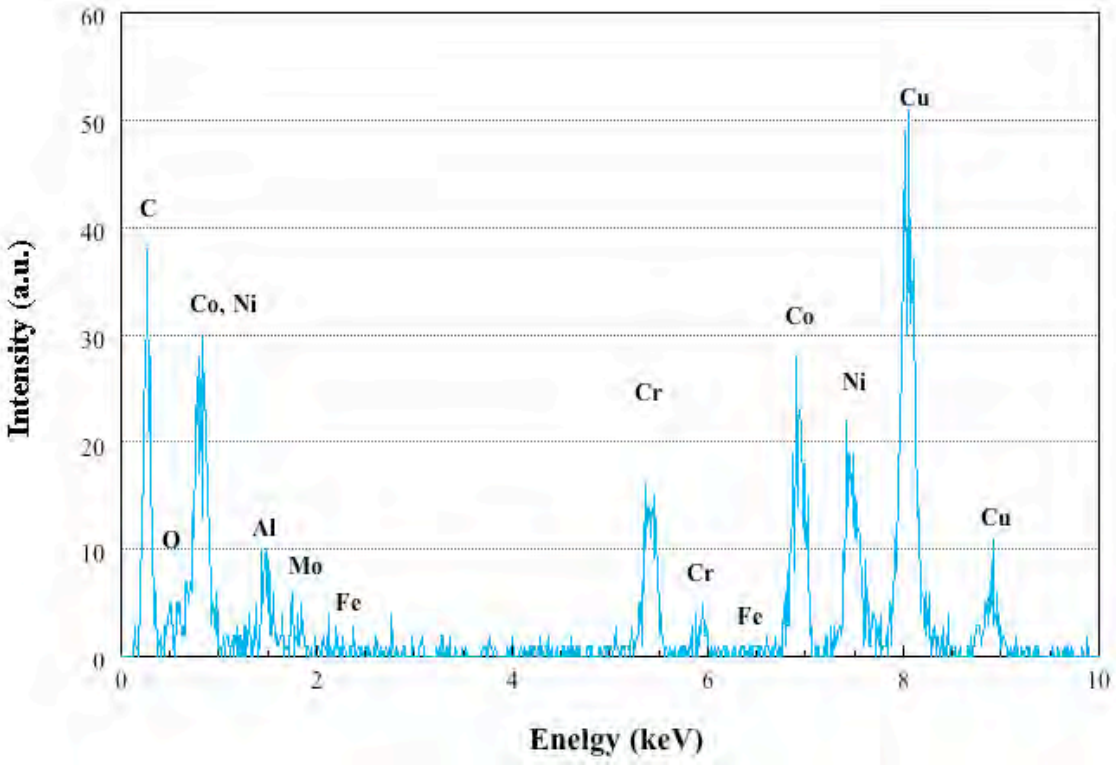

(b) Position "B" at Fig. 5-9

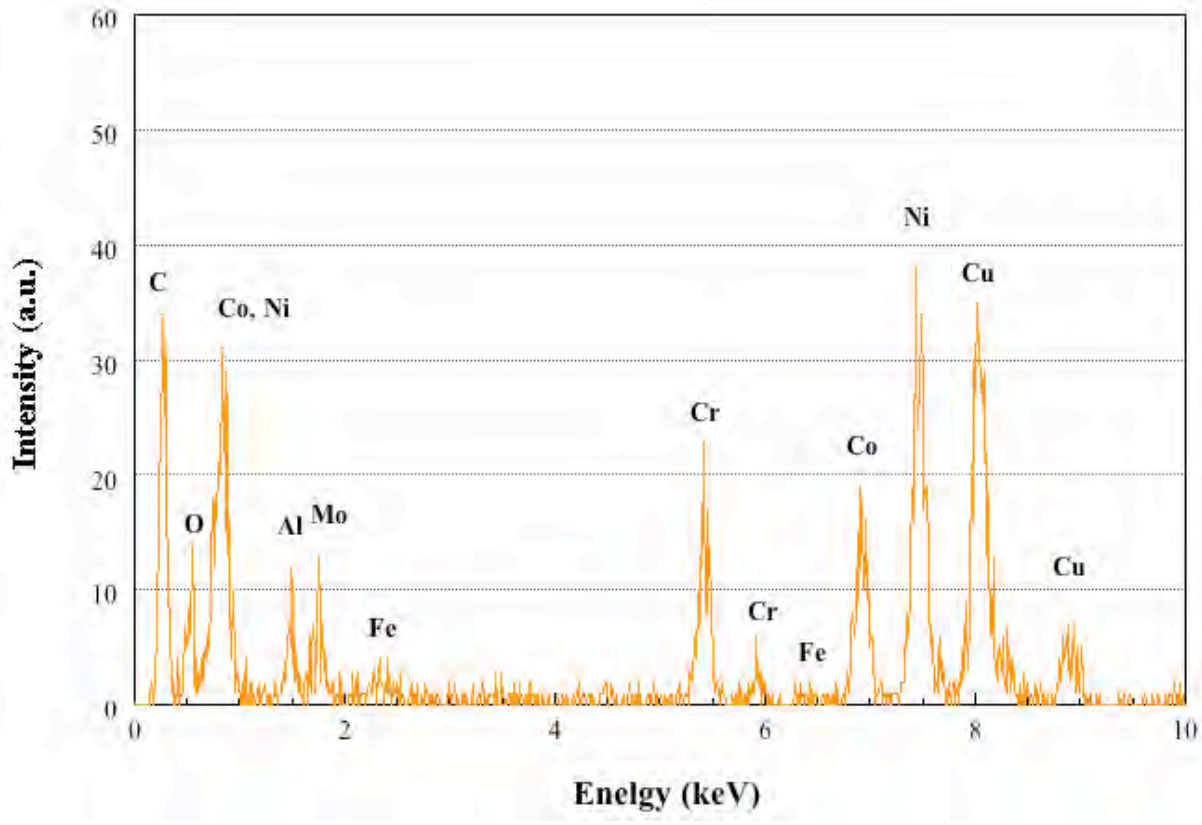

(c) Position "C" at Fig. 5-9

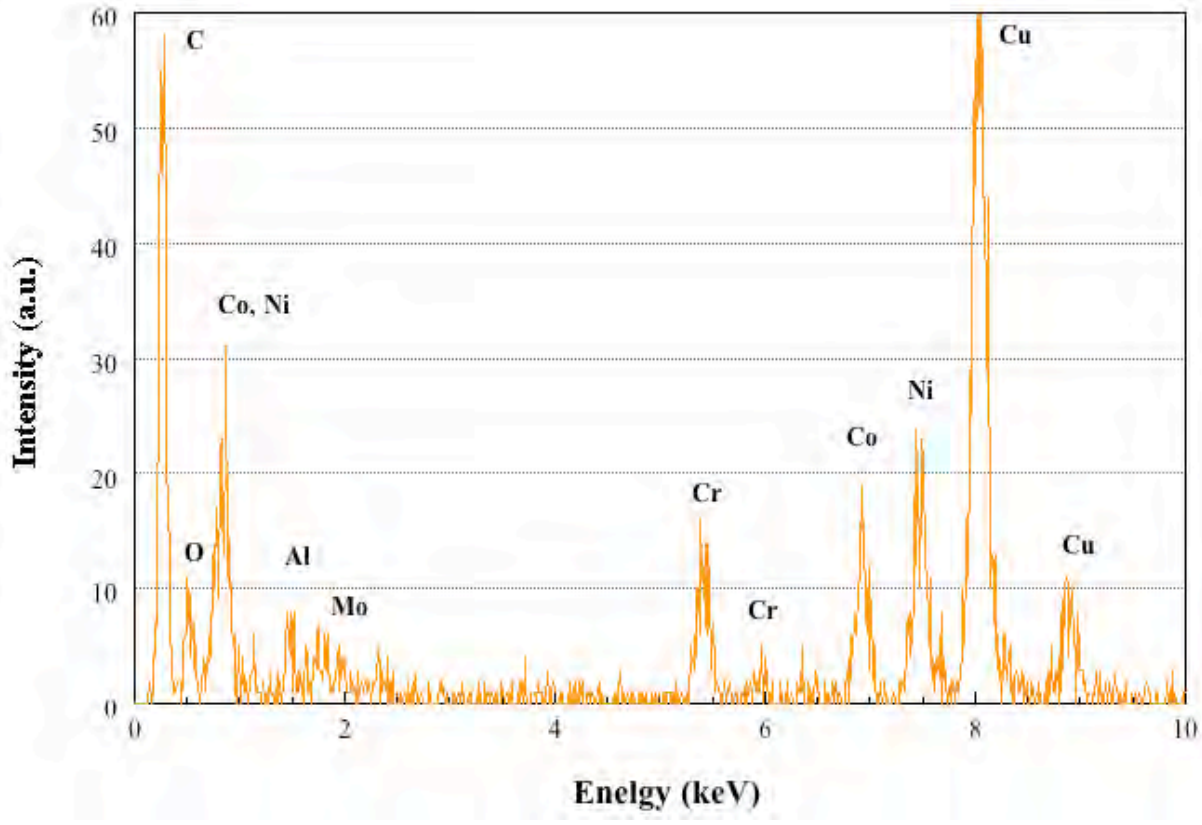

(d) Position "D" at Fig. 5-9

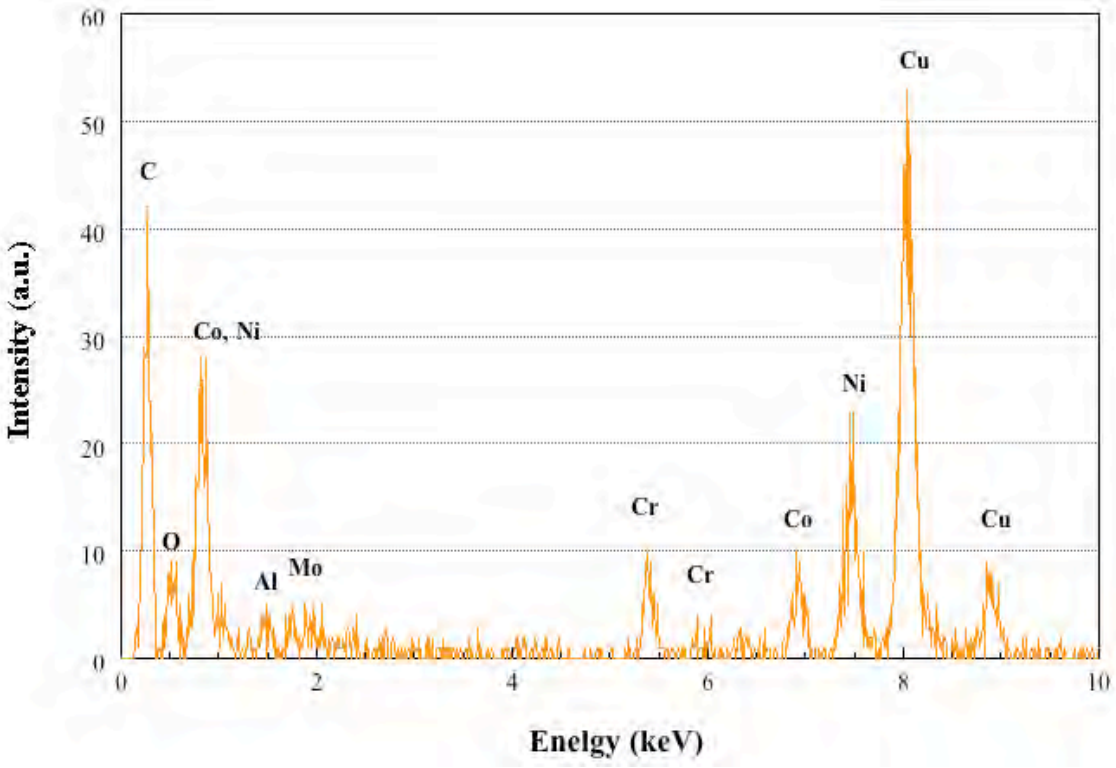

(e) Position "E" at Fig. 5-9

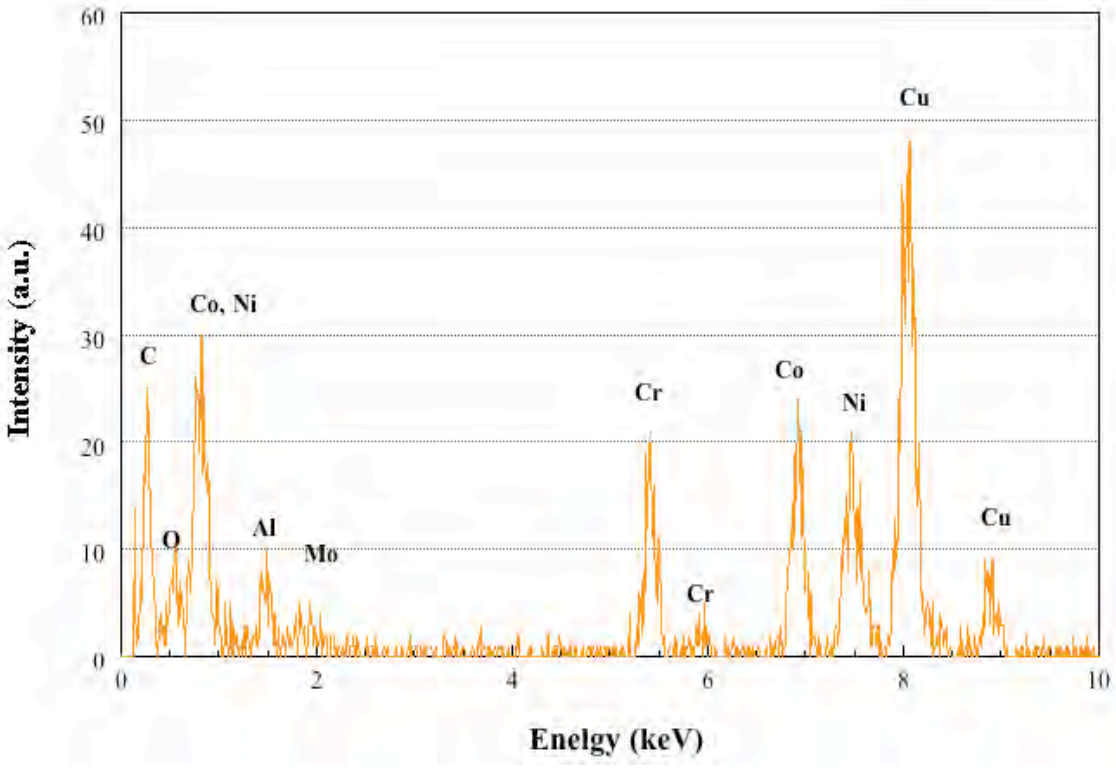

(f) Position "F" at Fig. 5-9

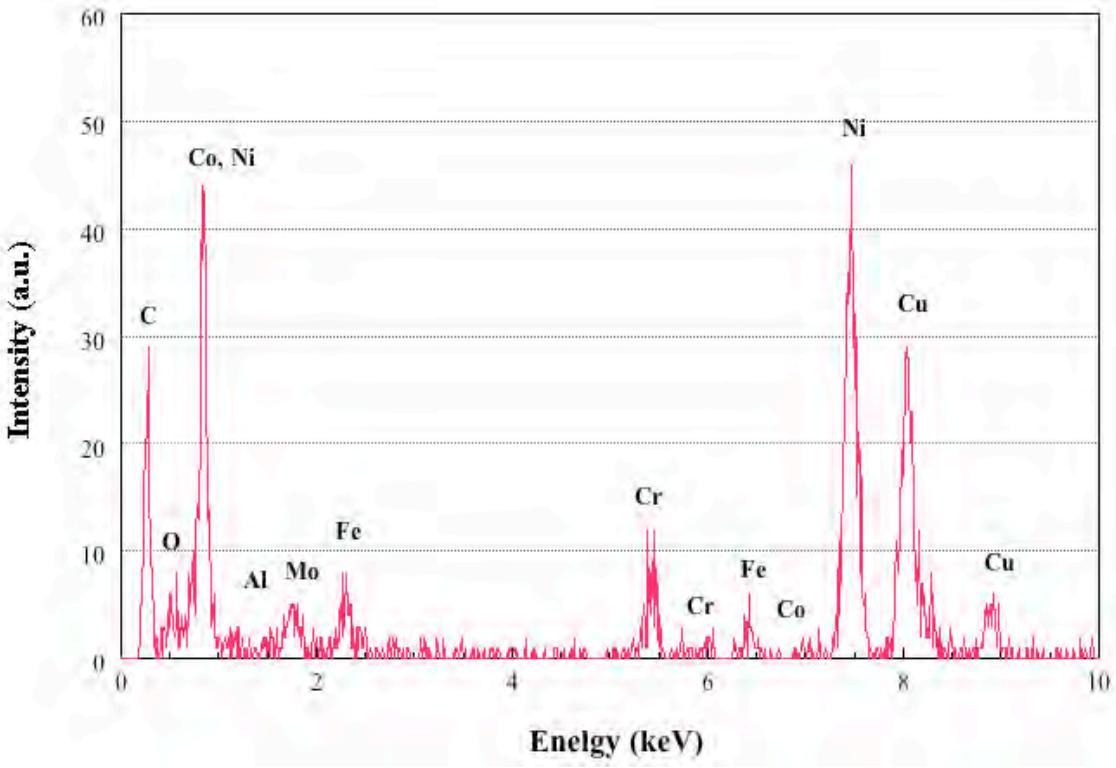

(g) Position "G" at Fig. 5-9

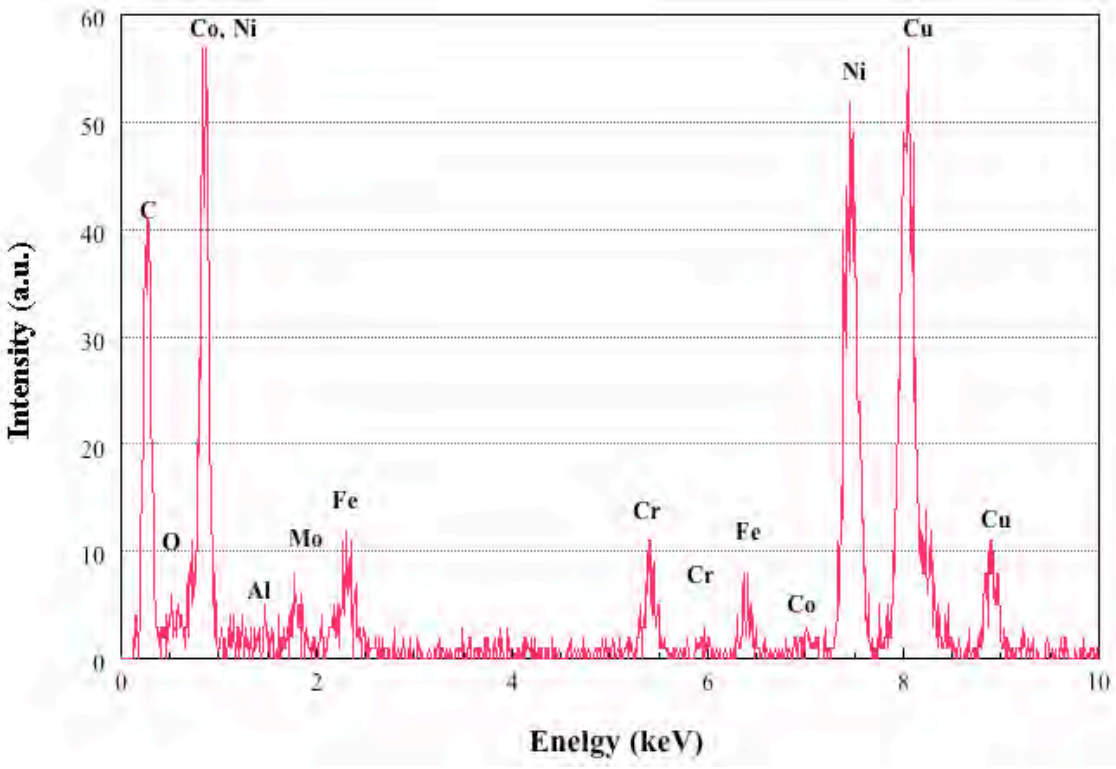

(h) Position "H" at Fig. 5-9

Fig. 5-10 EDX point elemental analyses results from region in the vicinity of the coating/substrate interface.

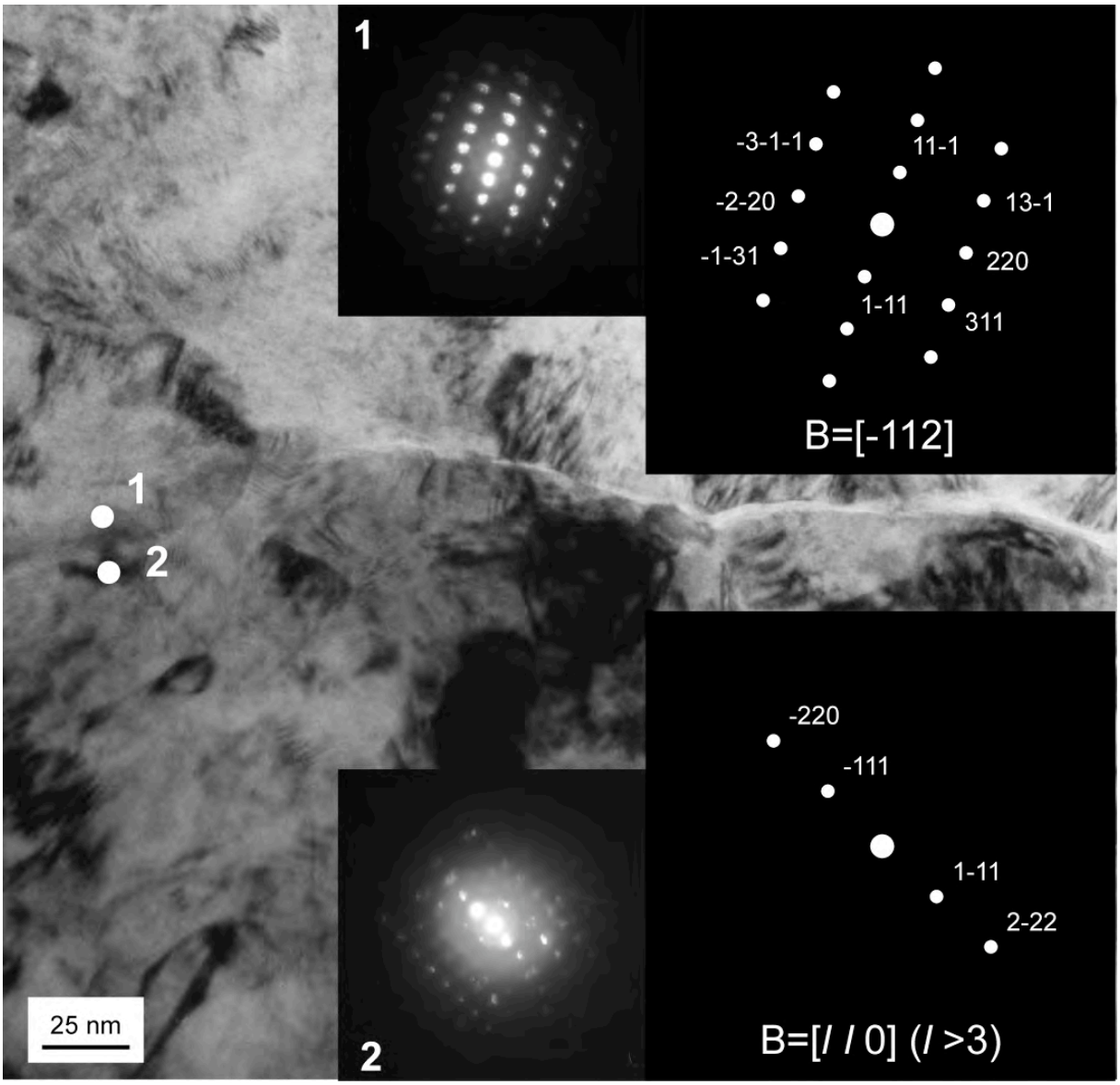

Fig. 5-11 TEM image and nano-beam diffraction patterns of contiguous crystals. 1: coating, 2: substrate.

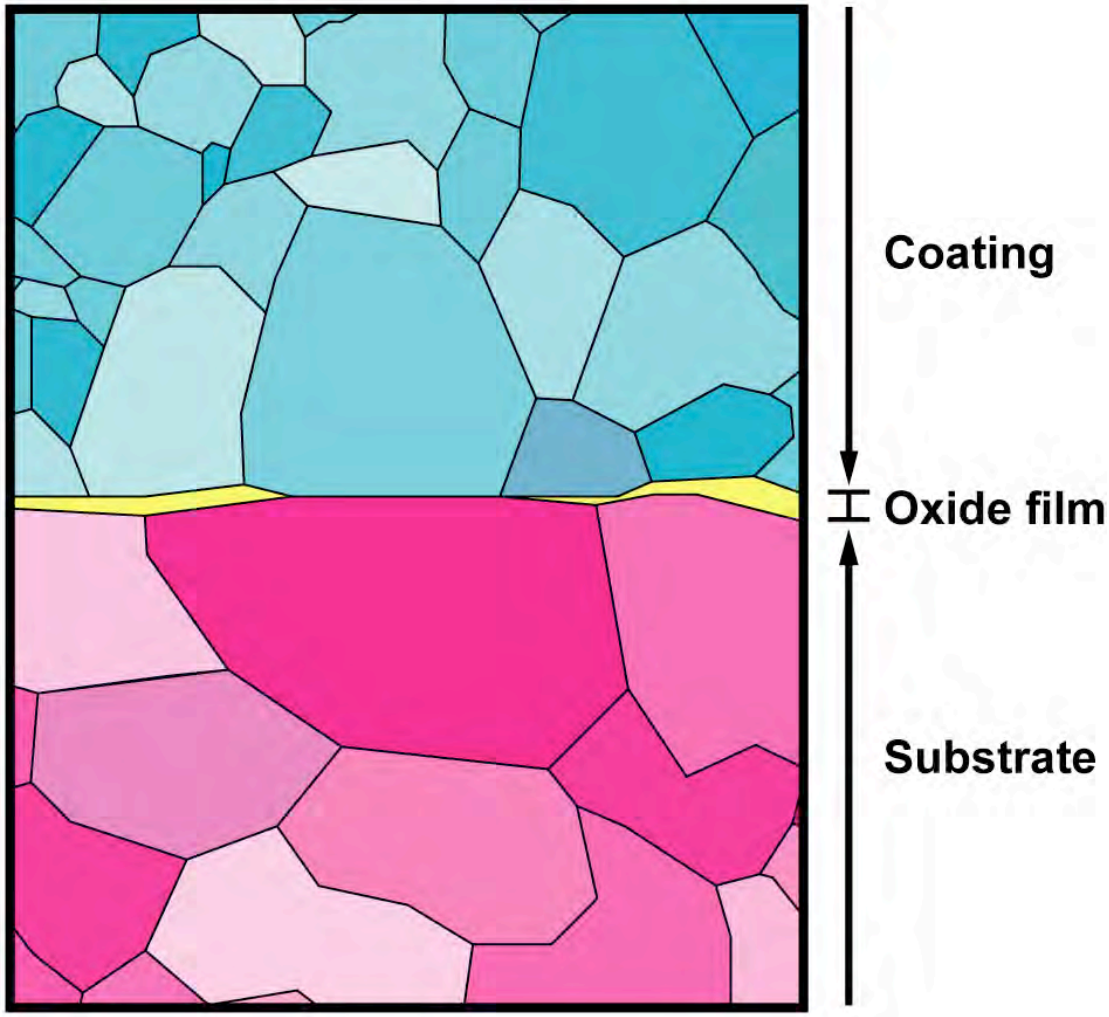

Fig. 5-12 Schematic illustration of coating/substrate interface structure of cold-sprayed CoNiCrAlY coating.

5.4 Summary

In order to elucidate the mechanisms of deposition by cold spraying, TEM and STEM observation and micro-EDX elementary analyses were carried out. In addition, nano-beam diffraction was used to analyze the orientation relationships between contacting grains of coating and substrate. The main results obtained from this chapter can be summarized as follows:

- From the STEM analysis results, a decrease in Al was observed at an earlier position compared to the decrease in Co. Thus, Al was depleted at the interface. The Al-depleted phase can be considered to be the γ/γ'-(Ni/Ni_3Al) phase of CoNiCrAlY. The decrease in this region may be attributed to the contact, which occurred in matrix of CoNiCrAlY during cold spraying.
- From the results of TEM analyses, a grain size miniaturization was observed. This was caused by high-speed plastic deformation during the cold-spraying process.
- There is an oxide film at the interface between the substrate and coating, as indicated by the results of TEM analyses. However, sometimes this oxide film cannot be observed, and usually the grains overlap the coating and substrate at these positions. More specifically, intermittent adhesion between coating and substrate occurred at these interfaces.
- From the TEM nano-beam diffraction (NBD) patterns, the two contacting grains have orientation relationships of (311) in Ni3Al and (1-11) in γ-Ni, which is not the best bonding condition. This combination has a good adhesion, similar to that of a grain boundary. Moreover, there is no evidence of melting of substrate or particles. Actual bonding of the cold-sprayed coating and substrate occurred at the contact area with nascent surfaces.

References

[5-1] T. Ohnishi, H. Koike, T. Ishitani, S. Tomimatsu, K. Umemura and T. Kamino. The Proc. of the 25th Inter. Symp. for Test. and Failure Analys., in Santa Clara, California (1999) pp. 449–453.

[5-2] Toshie Yaguchi, Takeo Kamino, Mitsumasa Sasaki, Gerard Barbezat, and Ryoichi Urao: Cross-sectional Specimen Preparation and Observation of a Plasma Sprayed Coating Using a Focused Ion Beam/Transmission Electron Microscopy System, Microsc. Microanal. 6, (2000) pp.218-223.

[5-3] Takeo Tanaka, Tsuyoshi Irisawa, Makoto Fujiwara, and Norio Gennai: Micrometer-scale fabrication and assembly using focused ion beam, Thin Solid Films 509 (2006) pp.113 – 117.

6 Simulation Tests of Cold Spraying Deposition Using LASER-FLEX Technique

6.1 Introduction

In order to investigate the adhesion mechanisms at the interfaces obtained by cold-spraying, impact conditions were simulated by high-velocity impacts of plates accelerated by a laser in an experiment called "LASER FLEX: laser shock flier impact experiments". Results of FEM simulation of the flier experiments are shown in Fig. 6-1. This experiment used a laser shock to fly a foil to a substrate and make a deposition [6-1].

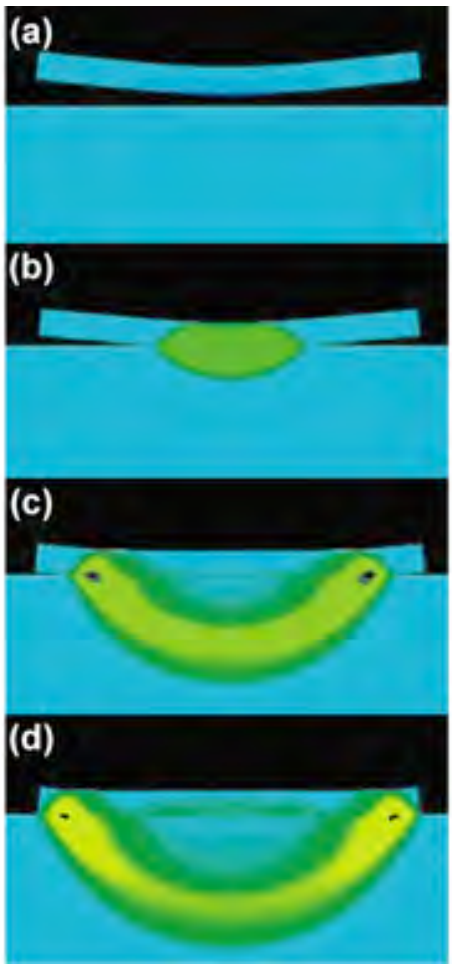

Fig. 6-1 FEM simulation results of laser shock flier impact experiments (Cu/Al) [6-2].

6.2 Experimental

The laser shock flier impact test is a simulation test for high-velocity impact in cold spraying, using a laser shock accelerated foil impact on a substrate. A schematic diagram of laser shock flier testing is shown in Fig. 6.2. In this study, two different experimental approaches were performed. One is a test using CoNiCrAlY foil, and the other is a test using CoNiCrAlY powder that is accelerated by an aluminum flier. Schematic illustrations of these experiments are shown in Fig. 6-3.

In the case of the CoNiCrAlY foil experiment, this test required a thin foil of coating material. However, it is difficult to find bulk CoNiCrAlY material. In this study, the hot isothermal pressing (HIP) technique was used to prepare the bulk CoNiCrAlY. A CoNiCrAlY cylinder was prepared from powders using the HIP technique. 30 mm-diameter and 80 mm-length cylinders were obtained. These were electro-discharge machined into 5 mm-diameter disks. The disks were subsequently polished to 50 μm-thickness foils as shown in Figs. 6-4 and 6.5. In the case of the test using CoNiCrAlY powder, aluminum foil was used for acceleration. A small amount of CoNiCrAlY (AMDRY 9951) powder was put on the aluminum foil.

A 20 J/ 20 ns pulsed Nd: YAG laser (Quantel PG-28) with a 1.064 μm wavelength was focused on a 3 mm-diameter spot and water-confined to generate shock waves in the samples of CoNiCrAlY foil or aluminum foil carrying CoNiCrAlY powder. They were accelerated and impacted on a mirror-polished INCONEL 625 substrate at high velocities. These laser flier impacts tests were performed at the Laboratoire de Combustion et Détonique, ENSMA, France.

Prior to the laser shock flier impact experiments, Velocity Interferometer System for Any Reflector (VISAR) using Doppler laser interferometry was applied to measure the velocity as a function of time and control the laser intensity to give a stable impact velocity of 700m/s in both tests.

Optical and scanning electron microscopy (SEM) was used to study the microstructures of the flier-substrate interface. SEM images were obtained using secondary electron (SE) and back-scattered electron (BSE) analysis. EDX point analysis was also carried out.

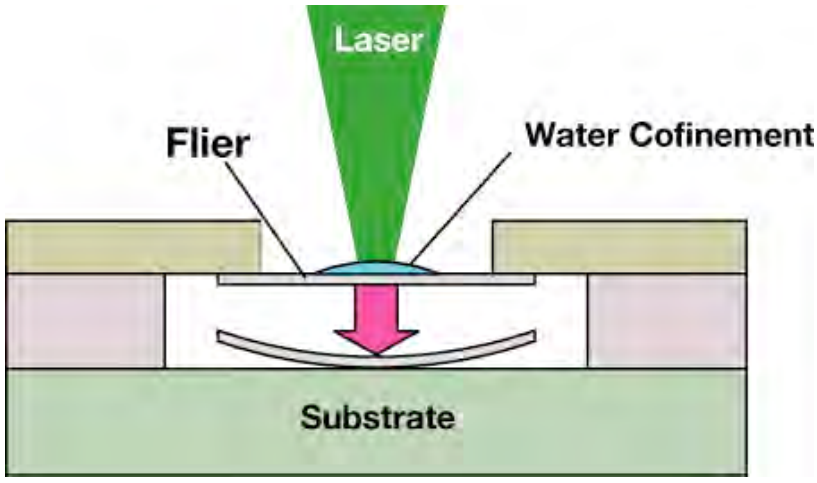

Fig. 6-2 Schematic illustration of experimental set-up for laser shock flier impact tests.

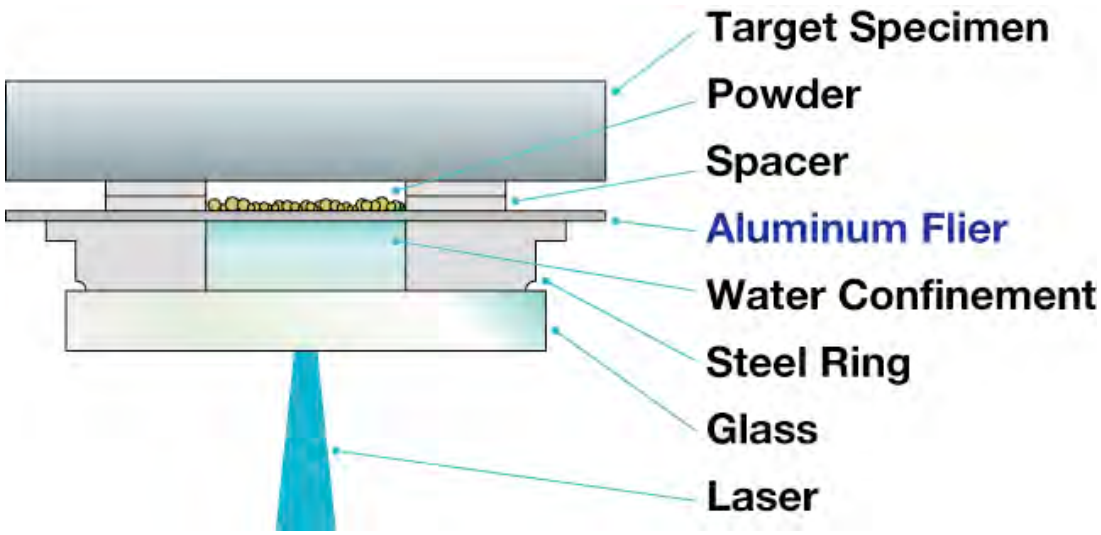

Fig. 6-3 Schematic illustration of experimental set-up for laser shock flier impact tests.

Fig. 6-4 HIPed MCrAlY (D:20mm L:50mm).

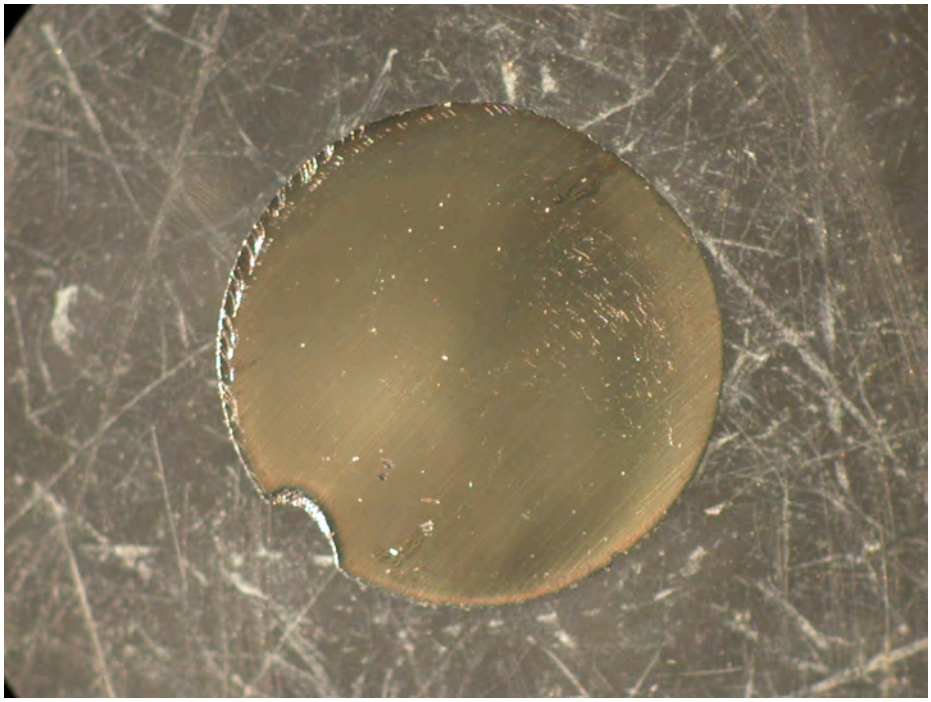

Fig. 6-5 MCrAlY Flier (D=5mm).

6.3 Results and Discussion

6.3.1 Evaluation of deposited MCrAlY Flier

Figure 6-6 (a) shows a cross-sectional SEM micrograph of the tested foil. The maximum surface velocity, which was measured by VISAR, was higher than 700 m/s. Laser shock acceleration succeeded in simulating the cold-spray impact phenomena. Fig. 6-6 (b) shows a typical cross-sectional SEM-BSE image of an as-received flier. A two-phase structure, similar to that in this image, was observed in most parts of the tested flier and the specimen. Therefore, it can be suggested that the laser irradiation has the influence on phase transformation during testing.

Figure 6-7 shows results of an EDX elemental investigation of the tested foil corresponding to the positions in Fig. 6-6 (b). Generally, MCrAlY type coatings consist mainly of γ/γ'-(Ni/Ni_3Al) γ-(Co, Al) matrix and β-(NiAl, CoAl), σ-(Co, Cr) precipitated phases [6-3]. From the EDX results, the Ni, Al and Cr contents in these phases are different. The EDX results suggest that the dark region in Fig. 6-6 (b) is the matrix, and the bright region is a precipitated phase.

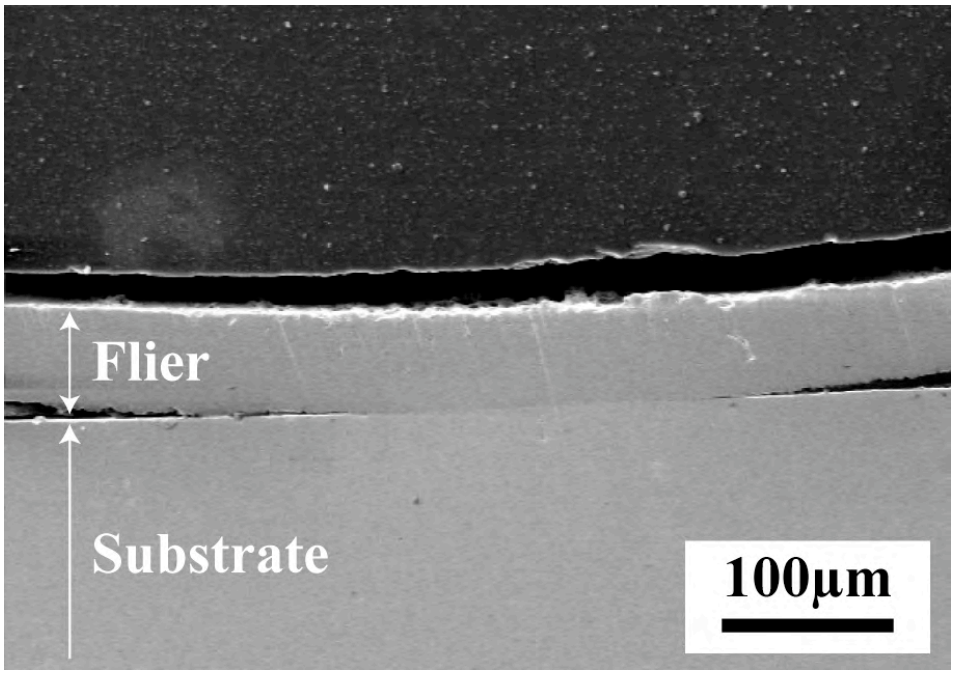

(a)

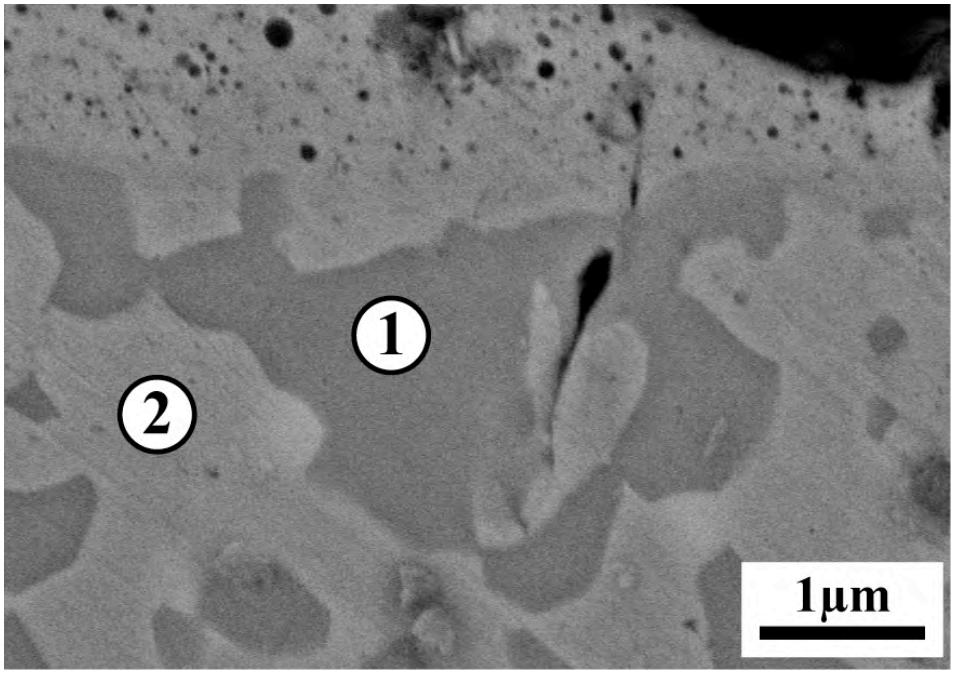

(b)

Fig. 6-6 *Typical cross-sectional SEM images of as-prepared CoNiCrAlY flier on INCONEL 625 substrate, (a) SE observation image of the attached region at low magnification (b) BSE observation image of CoNiCrAlY flier at high magnification. The numbers are marks corresponding to EDX analysis regions in Fig. 6-7.*

Figure 6-8 shows an SEM image from near the interface region observed at a high magnification. In this image, MCrAlY still has the dual phase such as γ/γ'-(Ni/Ni_3Al) γ-(Co, Al) matrix and β-(NiAl, CoAl), σ-(Co, Cr) precipitated phases. During the LASER-FLEX, there is a possibility of local temperature increase at the contact surface. However, the foil tested maintained a dual-phase structure with no melting. In other words, the local temperature increase does not affect the deposition mechanism.

The interface between the matrix region and the substrate is not clear, but the interface between the precipitated region and the substrate is clear in this image. The unclear interface between matrix phase and substrate may be attributed to local melting of the matrix phase. Adjacent phases have contacted with the INCONEL substrate, and the mechanical condition is similar. The melting temperature of the γ-Ni_{matrix} is 1728 K and that of β-NiAl is 1911 K. The local temperature perhaps increased to between 1728 and 1911 K, such that only the matrix phase melted. The input energy of LASER-FLEX is much larger than that of actual cold spraying, therefore excessive energy input may cause local melting at the interface.

Another difference in the interface appearance depends on the phase composition and crystal structure. INCONEL 625 mainly consists of γ-Ni phase and fine precipitate phases (of size from 10 to 20 nm) γ''-[Ni_3Nb], Ni_2(Cr, Mo). The CoNiCrAlY γ/γ'-(Ni/Ni_3Al) phase has an fcc crystal structure, and the matrix of MCrAlY and INCONEL 625 has almost the same lattice parameter and structure. Therefore, combinations of similar crystal structure, such as a MCrAlY matrix phase and INCONEL matrix phase, allows good adhesion. Therefore, different crystal structure may influence the deposition mechanisms.

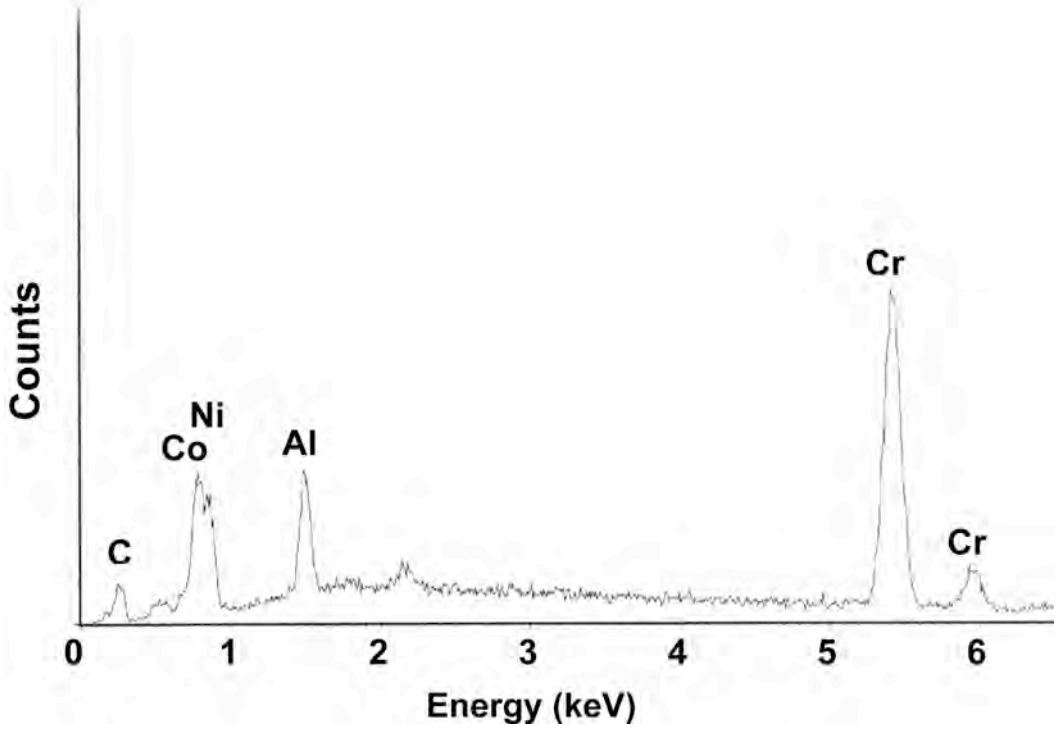

(1)

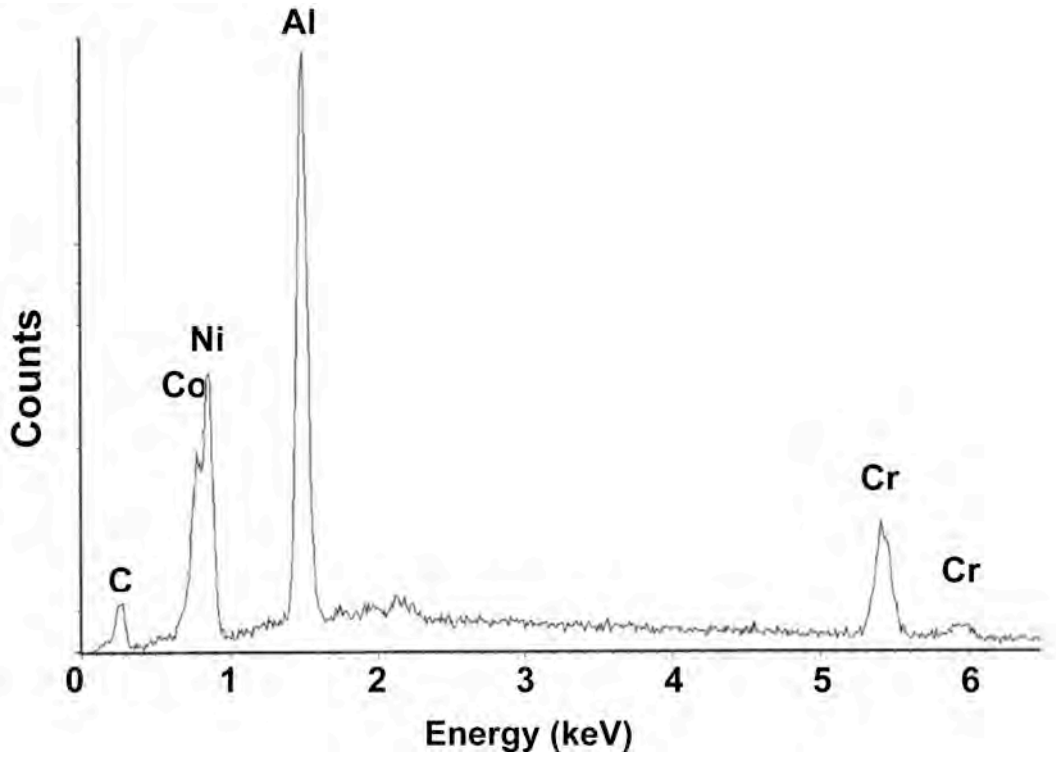

(2)

Fig. 6-7 SEM-EDX analysis results of CoNiCrAlY flier corresponding to Fig. 3.6, (1) dark region (2) bright region.

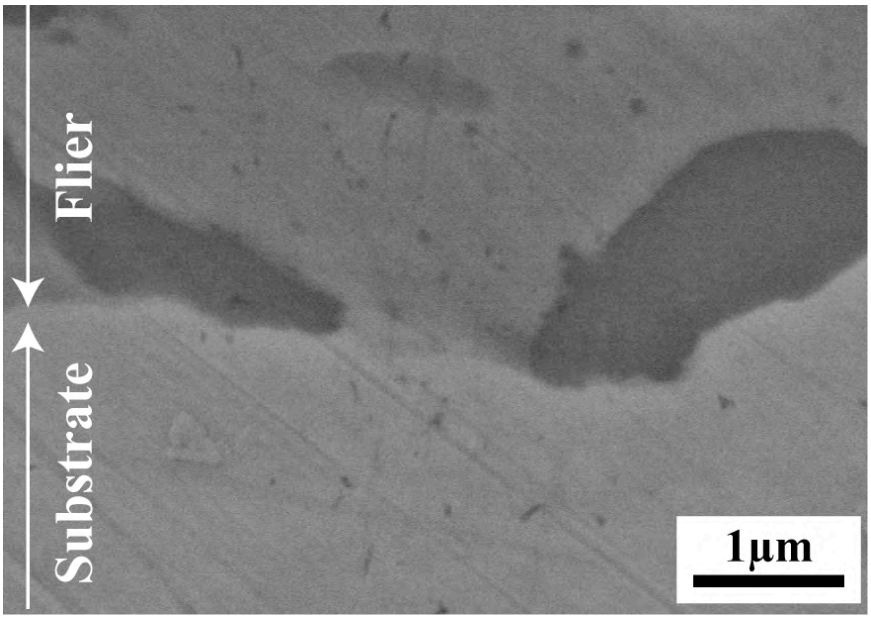

Fig. 6-8 Cross-sectional SEM-BSE images of interface between flier and substrate of as-prepared CoNiCrAlY flier on INCONEL 625 substrate.

.

6.3.2 Estimation of critical bonding condition

The deference between the LASER-FLEX and cold spray is the dynamic regime in the interface. The geometric relationship when the flier collides with the substrate is defined by Fig. 6-9. The flier collides at normal flier velocity V_F. At the same time the flier is deformed as shown in the simulation results. The relationship between V_F and V_N is defined as below:

$$V_N = V_F \cos\beta \tag{6-1}$$

where β is the collision angle.

The collision point velocity V_{PC} and V_N have the geometric relationship:

$$V_{PC} = \frac{V_N}{\sin\beta} \tag{6-2}$$

From these equations, the relationship between V_{PC} and V_F can be expressed as:

$$V_{PC} = \frac{V_F}{\tan\beta} \tag{6-3}$$

As mentioned before, the normal velocity of the flier was 700 m/s. The critical collision angle was determined from the specimen geometry as shown in Fig. 6-10. In this case, the angle is approximately 36 deg. Therefore the critical V_{PC} was estimated approximately 965 m/s. From these results, the critical collision point velocity such as the shear deformation velocity is extremely large.

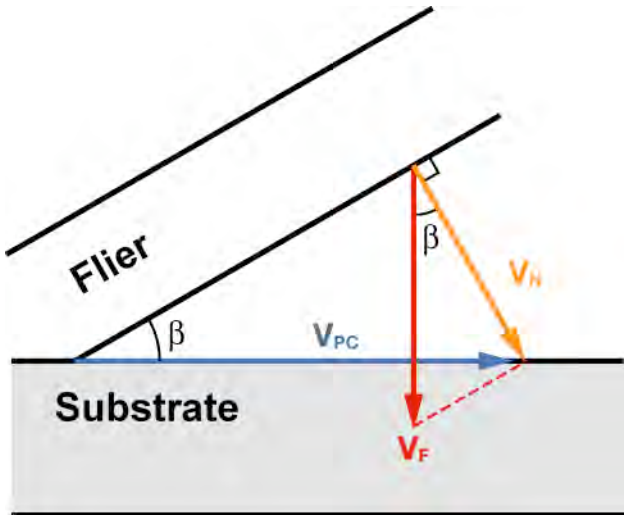

Fig. 6-9 Schematic illustration of force within the interface.

(a) Low magnified image of flier

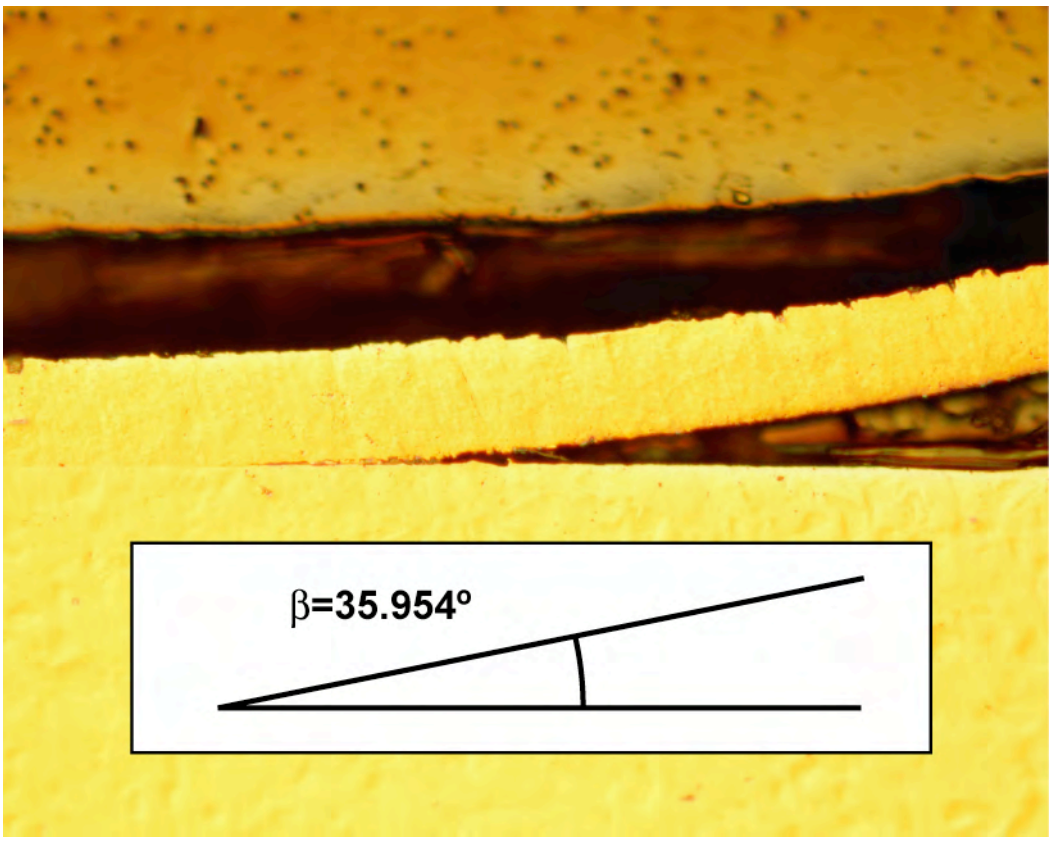

(b) Higher magnified image at the adhesion edge of flier

Fig. 6-10 Optical microscopic observation of critical collision angle of the tested flier.

6.3.3 Evaluation of impingement of deposited particle

Figure 6-12 shows a cross-sectional SEM image of an impinged particle, which was produced by LASER-FLEX. The measured collision velocity was approximately 700 m/s, the same as similar as the previous flier result. Even though the flier experiments obtained good adhesion, the particle is not completely deposited. The difference was caused by the impulse of the attached specimen. The

diameter of this particle is approximately 24 μm. The estimated impulse is 1.71×10^{-3} Nm/s, and this impulse is not enough for complete bonding an individual particle, despite a critical velocity of the individual 24 μm CoNiCrAlY powder of over 700 m/s. In the actual cold spray process, however, the next impinging particle assists in bonding the previous one, as mentioned in chapter 2, hence the actual impact velocity condition for cold-spray deposition may be below 700 m/s.

Fig. 6-11 Impulse of impinged particle in LASER FLEX

Impact velocity	700 m/s
Density	5.4
Dimension	Spherical (D=24 μm)
Weight	2.443 mg
Impulse	1.71 mN m/s

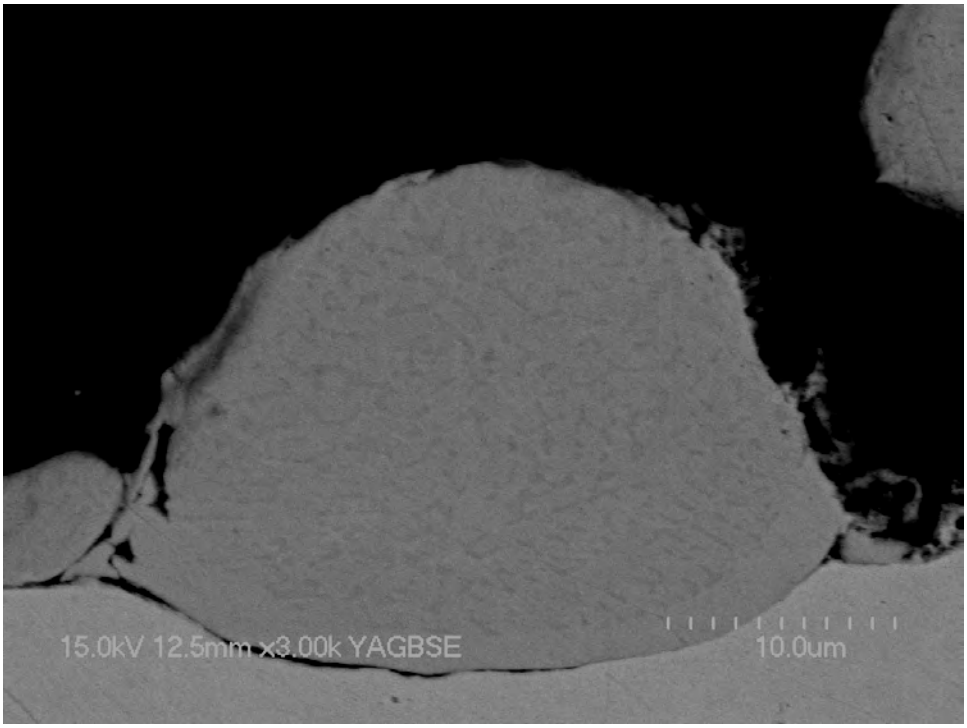

Fig. 6-12 Cross-sectional observation of impinged particle produced by LASER-FLEX.

6.4 Summary

This chapter considers an approach to simulating cold-spray phenomena. Different kinds of Laser Shock Flier Experiments (LASER-FLEX) were carried out. The main results obtained from this chapter can be summarized as follows:

- From the results of LASER-FLEX that used CoNiCrAlY foil, the deformation rates were extremely large. The interface between the matrix region and the substrate is not clear, but the interface between the precipitated region and substrate is clear in this image. The local temperature at the interface may be increased and hence the matrix phase be melted. However these phenomena were not observed in the actual cold spraying and LASER-FLEX tests using powder.
- Even though the flier and particle impinged at the same velocity, the adhesion behavior of the two were different therefore the impulse of the attached material must be an important aspect of deposition. The LASER-FLEX technique using powder appears to be a good way to simulate actual cold spray deposition.
- From the results of particles impinged at 700 m/s, the interface between particle and substrate does not have complete deposition. Therefore the critical velocity of 24 μm CoNiCrAlY powder on INCONEL substrate must be more than 700 m/s.

References

[6-1] Y. Ichikawa, K. Ogawa, M. Nivard, L. Berthe, M. Bostie, M. Ducos, S. Barradas, and M. Jeandin: Adhesion study of cold –sprayed CoNiCrAlY-Mo coating of INCONEL 625 using the Laser Shock Adhesion Test (LASAT), Materials Science Forum Vols. 539-543 (2007) pp. 1086-1091.

[6-2] S. Barradas: Etude, a l'aide du chock laser, des mecanismes d'sdherence aux interfaces cuivre / aluminium et cuivre / cuivre obtenues par projection thermique, Doctral thesis for Ecole des Minse de Paris, (2004) p. 158. (in French)

[6-3] D.R.G. Acha, R. Munoz-Arroyo, L. Singheiser, and W.J. Quadakkers: Modelling of phase equilibria in MCrAlY coating systems, Surface & Coatings Technology 187 (2004) pp. 272-283.

[6-4] D. Utu, W. Brandl, G. Marginean, I. Cartis and V.A. Serban: Morphology and phase modification of HVOF-sprayed MCrAlY-coatings remelted by electron beam irradiation, Vacuum 77 (2005) pp.451–455.

7 Suggestion of the Critical Conditions of Deposition

7.1 Introduction

As mentioned in Chapter 1, Assadi et al. [7-1] have tried to understand the critical velocity and bonding mechanism using experimental and computational approaches. When plastic deformation of the particle and substrate occur, high-speed friction induces shear stress and increases the temperature.

Assadi et al. assumed that the melting point was exceeded in a local area, due to high-speed impingement between a particle and the substrate. From this assumption, Assadi et al. suggested that the empirical equation for critical velocity is as below,

$$V_{critical} = 667 - 14\rho_P + 0.08T_{MP} + 0.1\sigma_u - 0.4T_{pi} \quad (7\text{-}1)$$

ρ_P : Density of particle (g/cm^3)

T_{MP} : Melting point of particle (ºC)

σ_u : Ultimate strength of particle (MPa)

T_{pi} : Initial temperature (ºC)

However, in fact, there is no local melting near the interface. The evidence for the lack of melting has been mentioned in previous chapters. The most important factor for deposition is considered to be the creation of nascent surfaces. Instead of the melting temperature, the maximum plastic strain was considered to be the dominant factor for deposition.

In this chapter, in order to discuss the critical deposition conditions, finite element method (FEM) calculations and measurements of the dimensions of deposited particles were carried out. By comparing these experimental and computational results, the cold-spray deposition mechanism was studied.

7.2 Experimental

7.2.1 Johnson-Cook model simulation of deposited particles

In order to estimate the stress and strain for a deposited particle and substrate, a Johnson-Cook (JC) simulation was carried out. The JC simulation required knowledge of the material constants, such as A, B, C and *m*in the following equation. However, it is difficult to obtain the actual material constants of INCONEL 625 and AMDRY 9951. Some researchers have studied the mechanical properties of the Ni base superalloy such as INCONEL 718 alloy [7-2, 3]. In this study, the mechanical properties obtained in those works were used. The mechanical properties of Ni- and Co-base alloys are shown in Table 7-1. From the table, it can be seen that the mechanical properties of these alloys do not differ greatly; therefore we use the material constants of INCONEL 718 for the impact simulation. The chemical compositions of these alloys are shown in Table 7-2 to 4Table 7-4. The Johnson–Cook model is an empirically based representation of the flow stress defined as:

$$\sigma = \left[A + B\varepsilon^{n}\right]\left[1 + C\ln\dot{\varepsilon}_{0}\right]\left[1 - \left(\frac{T - T_{R}}{T_{M} - T_{R}}\right)\right] \tag{7-1}$$

where s is the flow stress, e is the effective plastic strain, $\dot{\varepsilon}_0$ is the effective plastic strain rate, usually normalized to a strain rate of 1.0/s, *n* is the strain-hardening exponent and *A*, *B*, *C* and *m* are constants. The parameters used are shown in Table 7-5. These were obtained by R. Sievert et al. [7-2] The FEM model and conditions used are summarized in Fig. 7-1 and Table 7-6. This model was developed using examples from the reports of Gartner et al. [7-4 to 6].

Table 7-1 Mechanical properties of Ni- and Co-base alloys (under room-temperature conditions)

	Yield strength (MPa)	Tensile Strength (MPa)	Elongation (%)	Hardness
Co-base superalloy Udimet 188	446	963	55	--
Ni-base superalloy INCONEL 625	414	827	60	175-240 HB (185-250 Hv)
Ni-base superalloy INCONEL 718	448	896	54	95 Rb (220 Hv)

Table 7-2 Limiting Chemical Composition of UDIMET alloy 188 (wt. %)

Carbon	0.05-0.15
Manganese	1.25 max.
Silicon	0.20-0.50
Chromium	20.0-24.0
Nickel	20.0-24.0
Tungsten	13.0-16.0
Lanthanum	0.02-0.12
Boron	0.015 max.
Iron	3.0 max.
Cobalt	Balance*

*Reference to the 'balance' of a composition does not guarantee this is exclusively of the element mentioned but that it predominates and others are present only in minimal quantities.

Table 7-3 Limiting Chemical Composition of INCONEL alloy 625 (wt. %)

Nickel	58.0 min.
Chromium	20.0-23.0
Iron	5.0 max.
Molybdenum	8.0-10.0
Niobium (plus Tantalum)	3.15-4.15
Carbon	0.10 max.
Manganese	0.50 max.
Silicon	0.50 max.
Phosphorus	0.015max.
Sulfur	0.015 max.
Aluminum	0.40 max.
Titanium	0.40 max.
Cobalt**	1.0 max.

** If determined

*Table 7-4 Limiting Chemical Composition of INCONEL alloy 718*** (wt. %)*

Nickel (plus Cobalt)	50.00-55.00
Chromium	17.00-21.00
Iron	Balance****
Niobium (plus Tantalum)	4.75-5.50
Molybdenum	2.80-3.30
Titanium	0.65-1.15
Aluminum	0.20-0.80
Cobalt	1.00 max.
Carbon	0.08 max.
Manganese	0.35 max.
Silicon	0.35 max.
Phosphorus	0.015 max.
Sulfur	0.015 max.
Boron	0.006 max.
Copper	0.30 max.

*** Conforms to AMS specifications

**** Reference to the 'balance' of a composition does not guarantee this is exclusively of the element mentioned but that it predominates and others are present only in minimal quantities.

Table 7-5 Johnson-Cook parameters of INCONEL alloy 718 [7-2]

A (MPa)	B (MPa)	C	m	n	$\dot{\varepsilon}_0$ (1/s)	T_R (ºC)	T_M (ºC)
450	1700	0.017	1.3	0.65	10^{-3}	25	1297

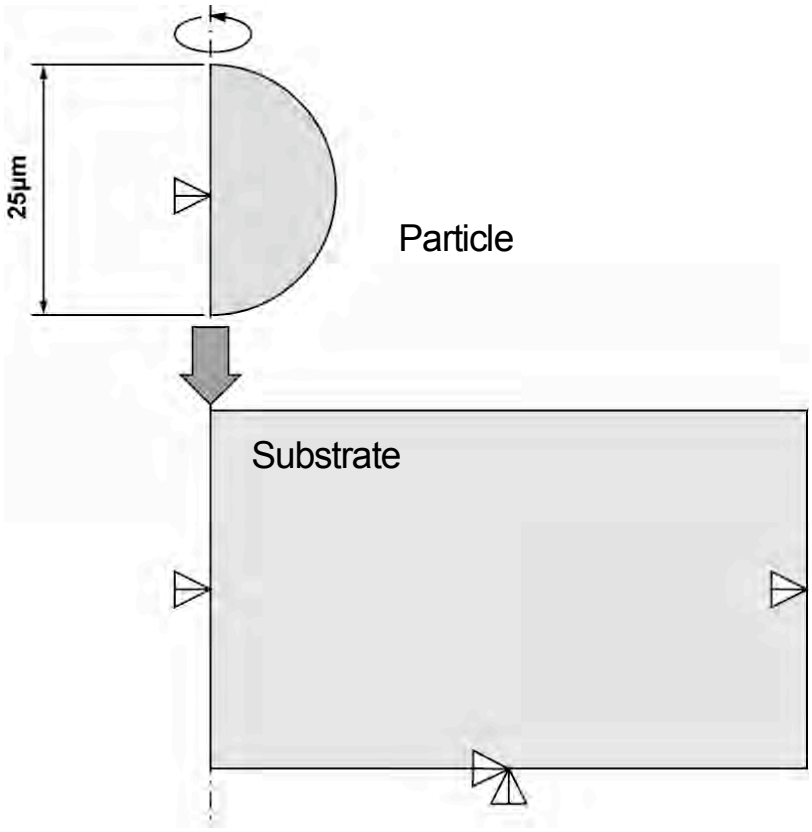

Fig. 7-1 Schematics of FEM simulation model.

Table 7-6 FEM simulation conditions

Software	ABAQUS / CAE Ver. 6.5-3
Modeling space	Axial symmetric model
Element type	Temperature displacement coupled CAX4RT
Particle diameter	25 μm
Mesh size	0.5 μm
Re-mesh	Adaptive mesh
Particle initial temperature	873 K
Substrate initial temperature	300K
Elastic deformation model	Young's modulus
Plastic deformation model	Johnson-cook
Inelastic fever heat	0.9

7.2.2 Measurements of dimensions of deposited particles

In order to understand the deformation of deposited particles and to make a comparison between the experimental results and FEM simulation, the dimensions of deposited particles were measured. In this measurement, the dimension parameters such as the width, height, and incursion depth in the substrate were defined as shown in Fig. 7-2. Note that the incursion depth was measured from the substrate deformation.

The specimen and observation technique were same as in Chapter 3. SEM images were obtained at an angle of 45º. Therefore the obtained SEM images were compressed in a perpendicular direction. Consequently, in order to measure the dimensional parameters, the image was expanded by square root 2 in the perpendicular direction.

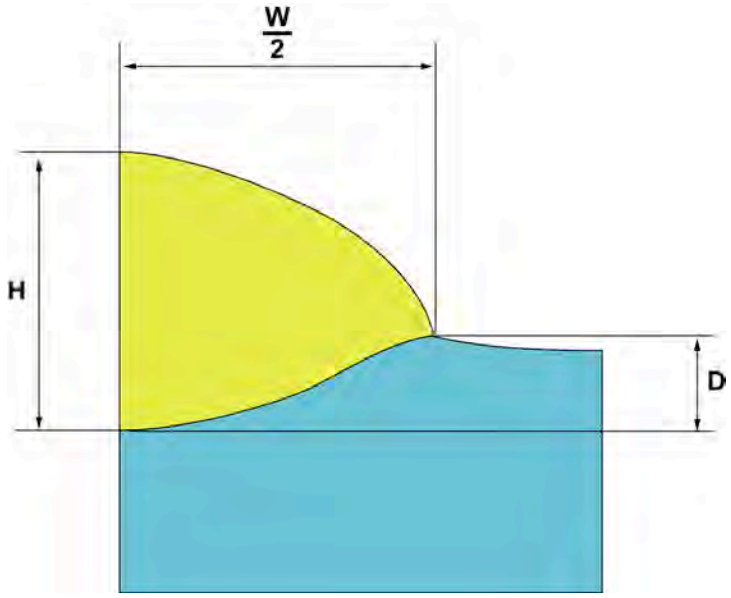

Fig. 7-2 Definition of the deposited particle geometry, W: width of the particle, H: height of the particle, D: intrusion depth of the substrate.

7.3 Results and Discussion

7.3.1 Results of FEM simulation

In this simulation, the particle size is 25 μm in diameter and the temperature is 600 ºC. Fig. 7-3 shows FEM simulation results for the strain and temperature distribution for a particle impinging at various velocities.

Under each velocity condition of impingement, the maximum strain was observed at the edge of the particle, and hence the temperature distribution as a function of the strain also shows a similar trend to the strain distribution.

The dependences of the maximum plastic strain and temperature on velocity during impingement are shown in Figs. 7-4 and 5, respectively. The maximum plastic strain had highest value at 500 m/s.

However, in the case of velocities over 600m/s, the maximum plastic strain decreased. From the simulation results of the deformed particle and substrate shown in Fig. 7-3 (e-1) to (f-2), in the case of 600 and 700 m/s, the edge shape after deformation had a much steeper angle. Moreover, a strong constraint condition caused a reduction in maximum strain values. Despite the low strain values, these particles have a very large deformation.

On the other hand, the maximum strain of the substrate increased with the velocity. Especially in the case of 500 m/s and 600 m/s, a rapid rise in maximum strain was observed. In the case of the particle, a similar rapid increase was observed from 300 to 500 m/s. These tendencies indicate that the substrate was more difficult to deform than the particles.

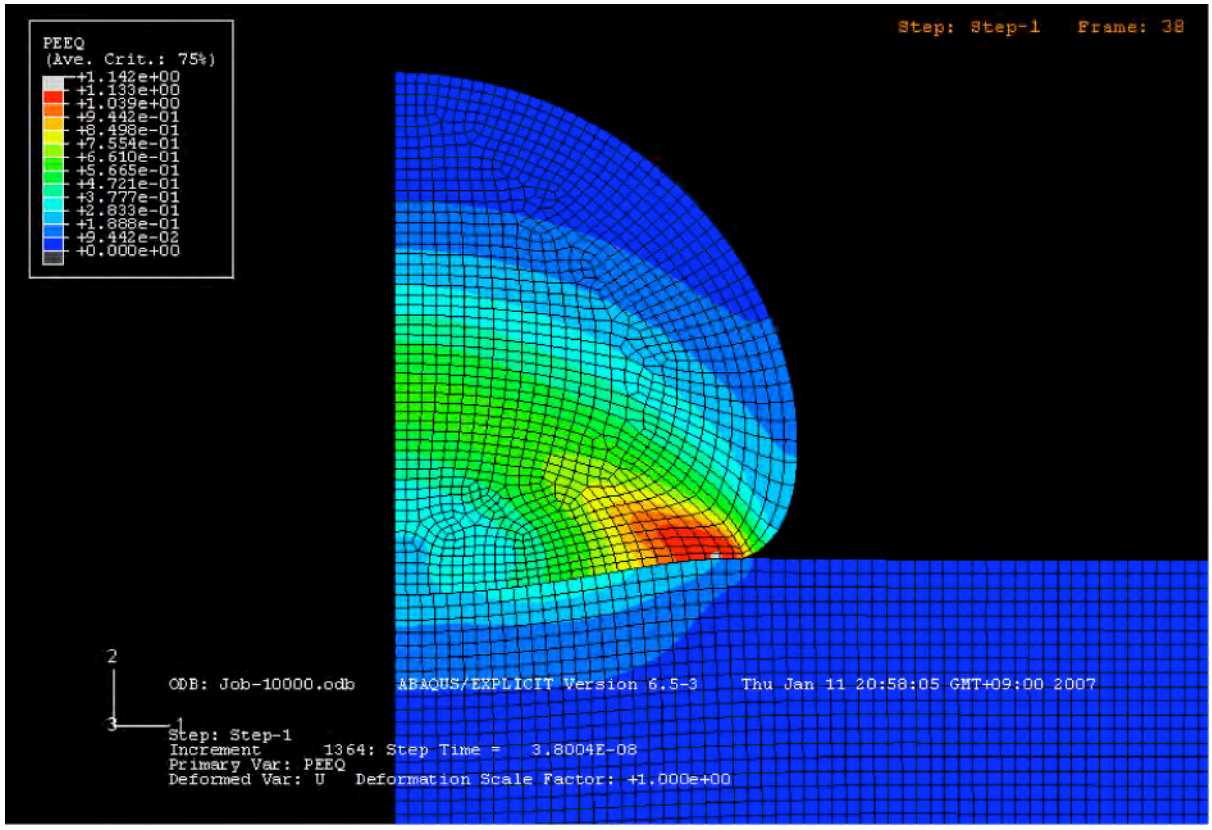

(a-1) Result of plastic strain (velocity 300 m/s)

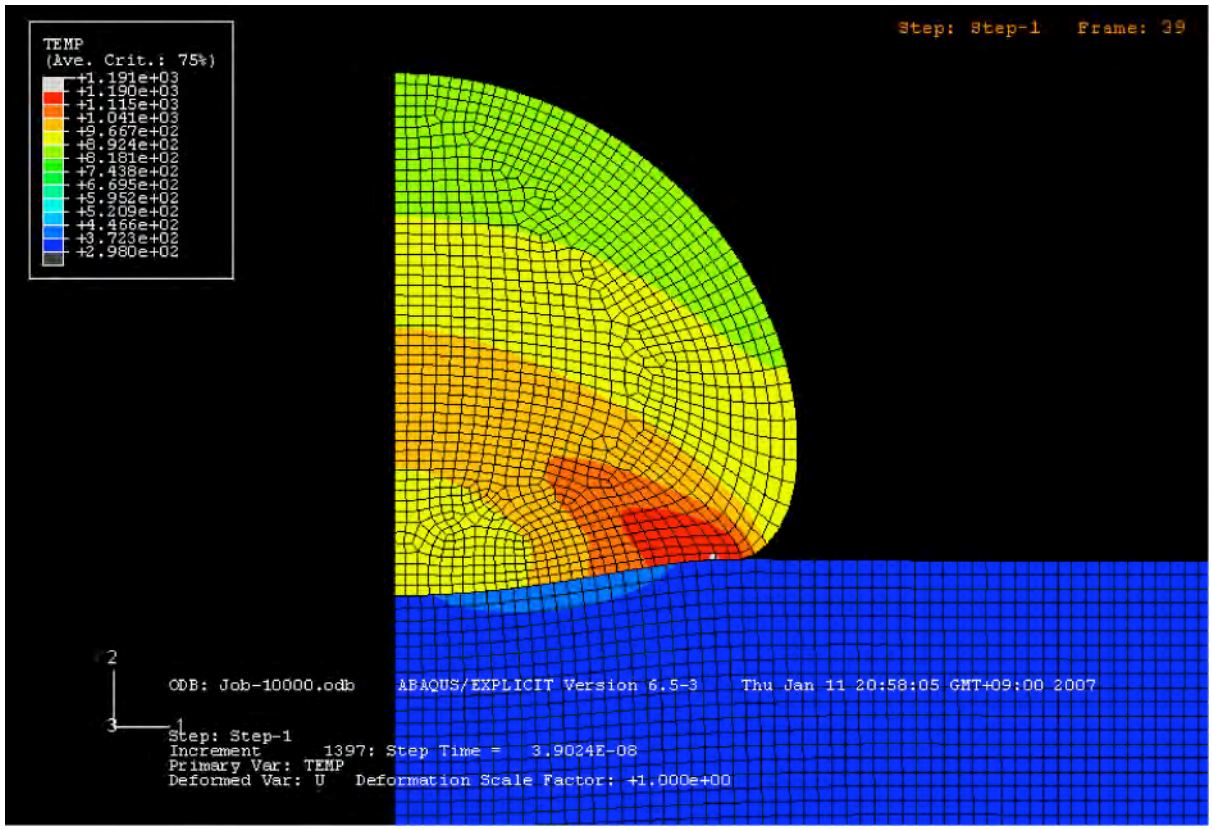

(a-2) Result of temperature distribution (velocity 300 m/s)

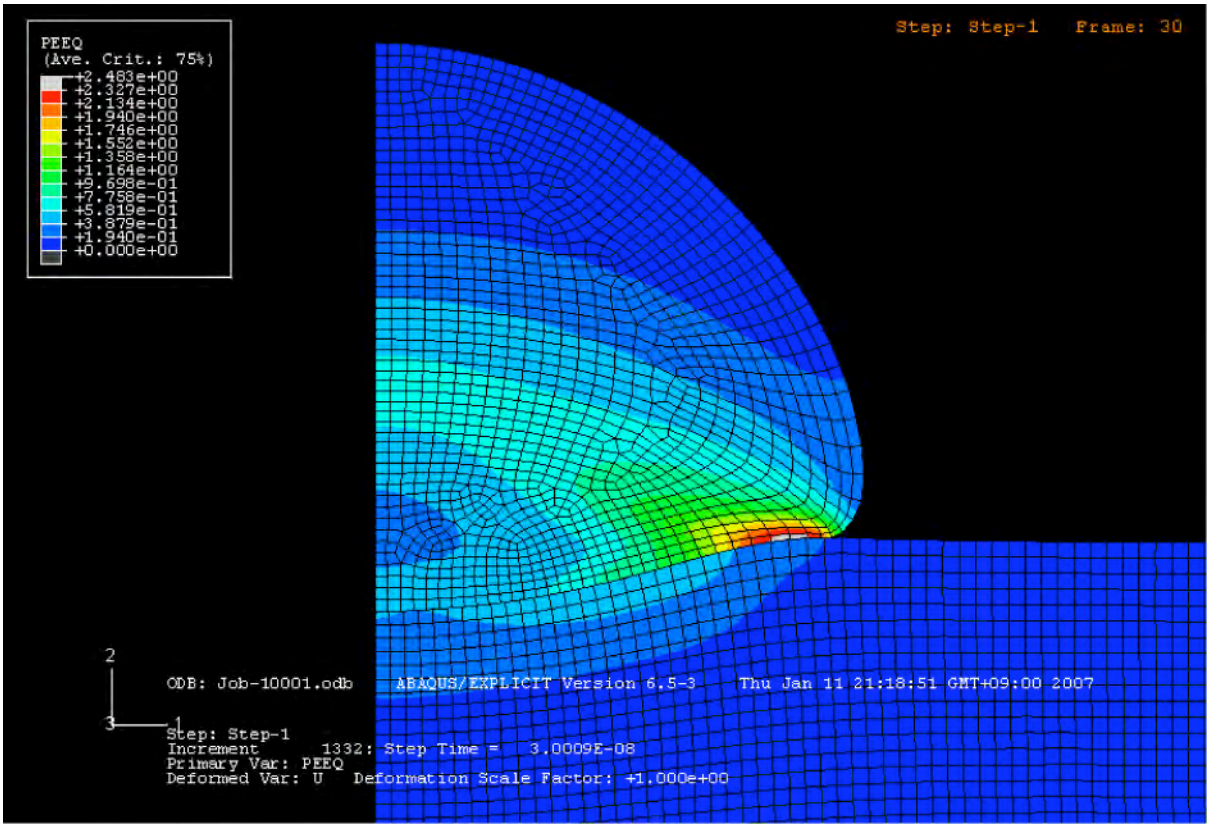

(b-1) Result of plastic strain (velocity 400 m/s)

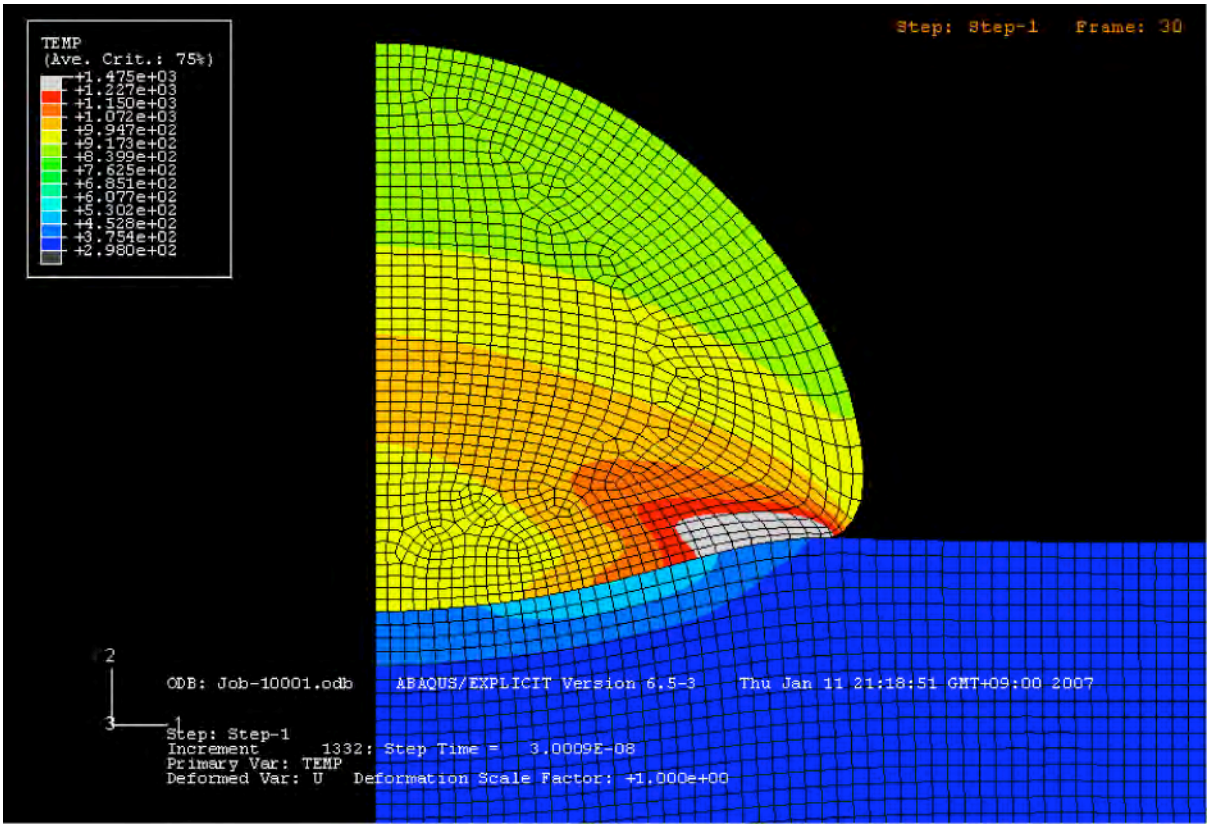

(b-2) Result of temperature distribution (velocity 400 m/s)

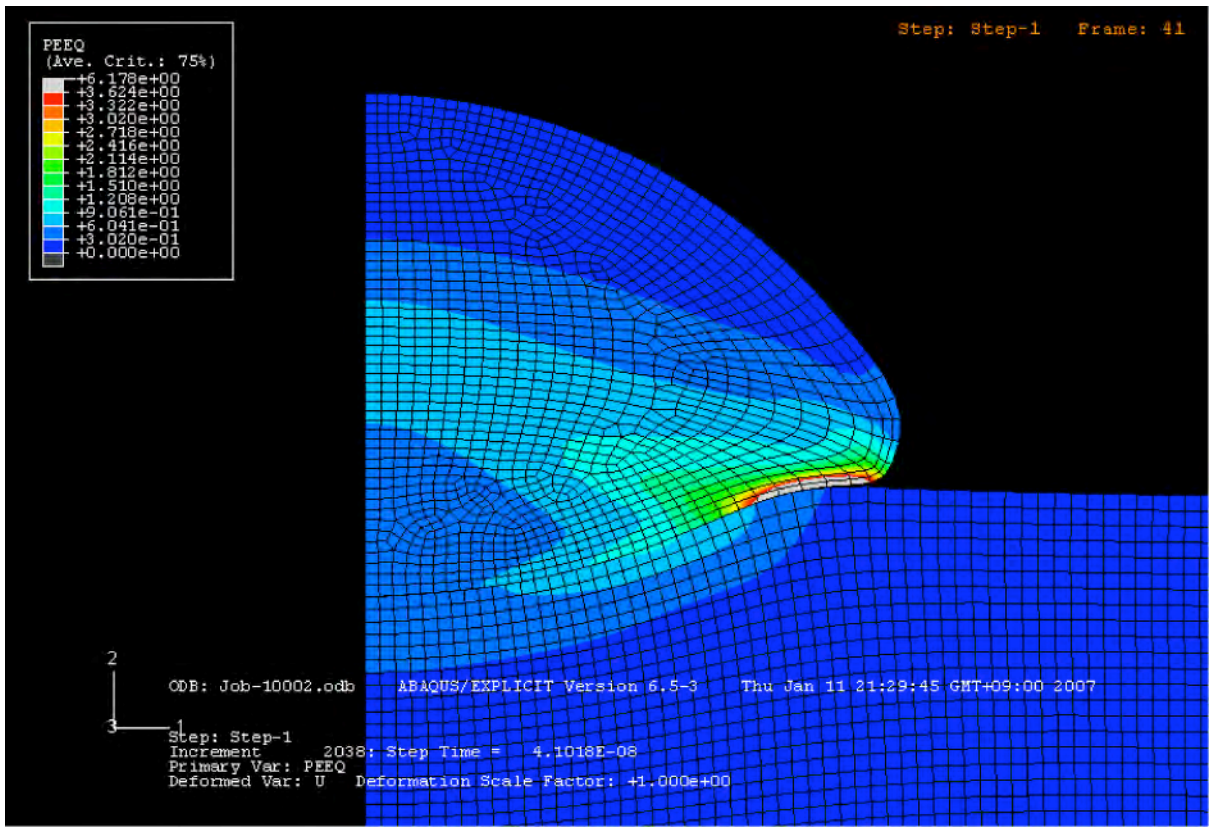

(c-1) Result of plastic strain (velocity 500 m/s)

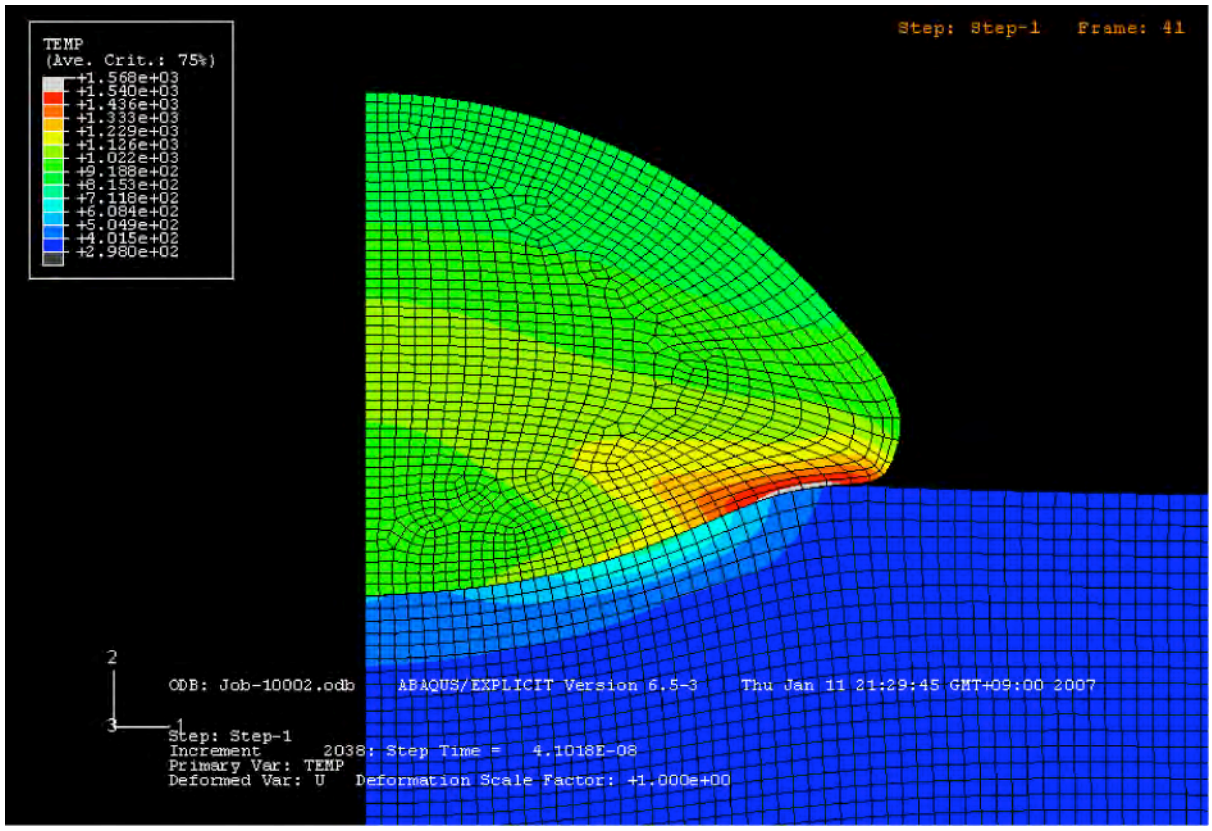

(c-2) Result of temperature distribution (velocity 500 m/s)

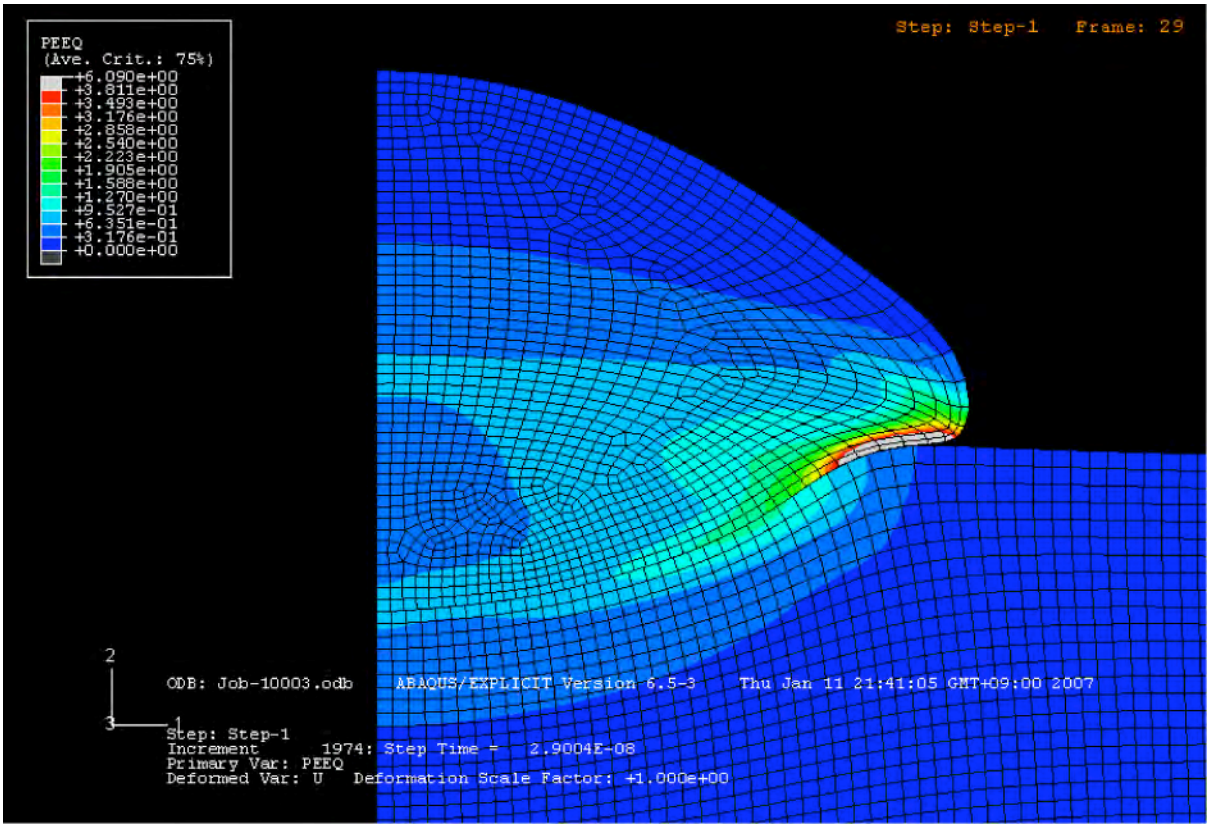

(d-1) Result of maximum plastic strain (velocity 600 m/s)

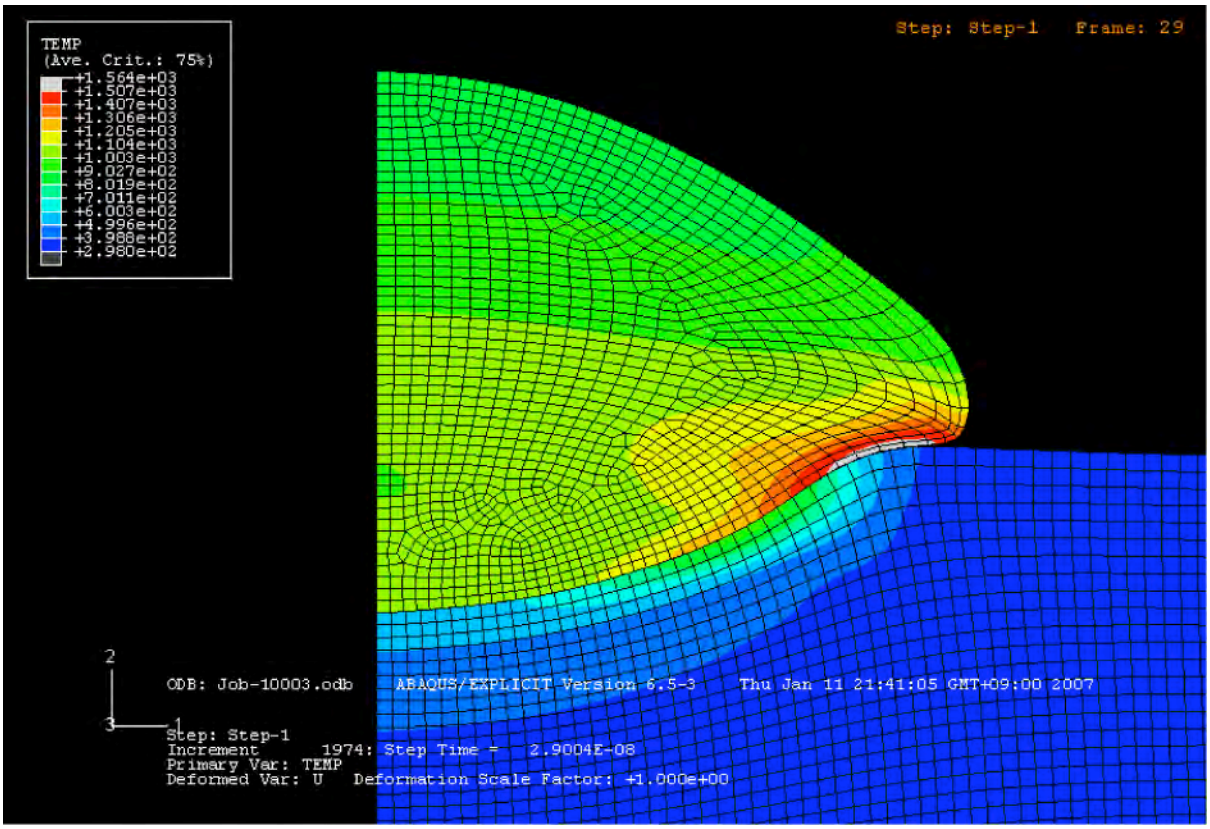

(d-2) Result of temperature distribution (velocity 600 m/s)

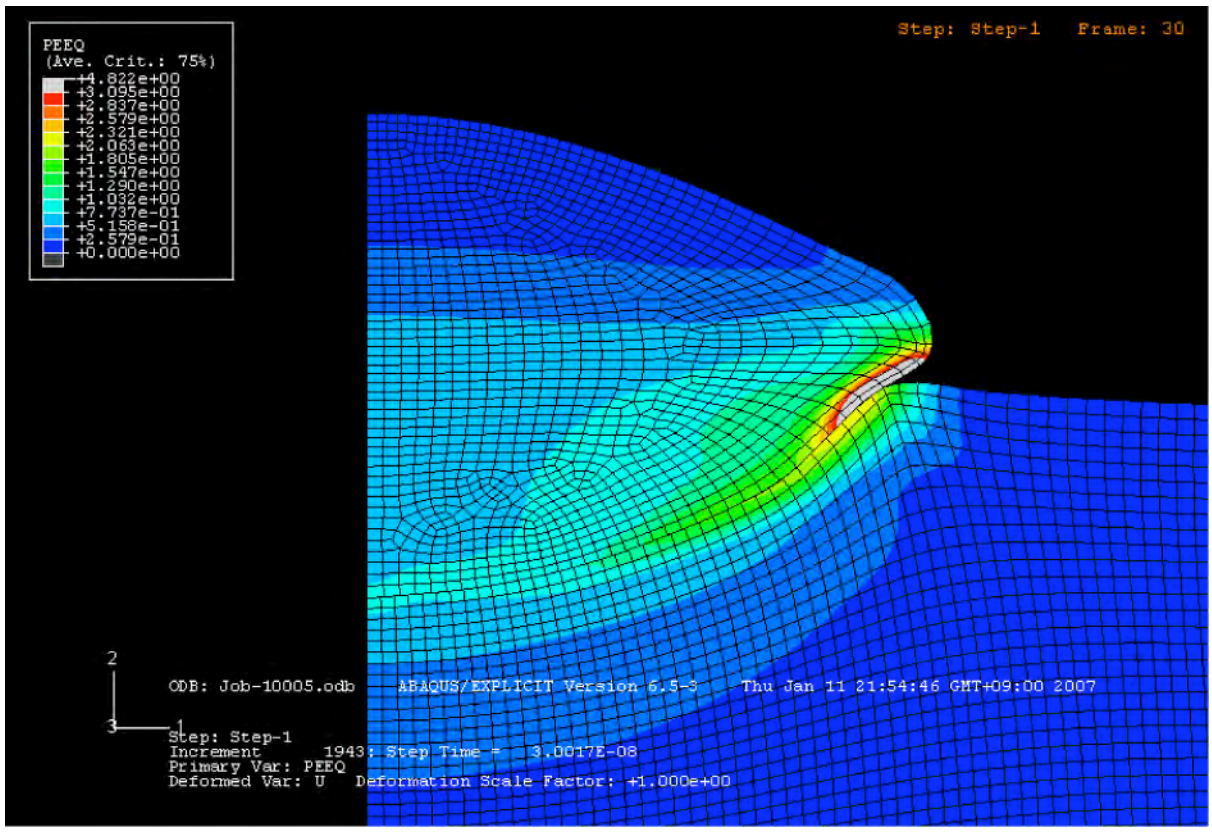

(e-1) Result of plastic strain (velocity 700 m/s)

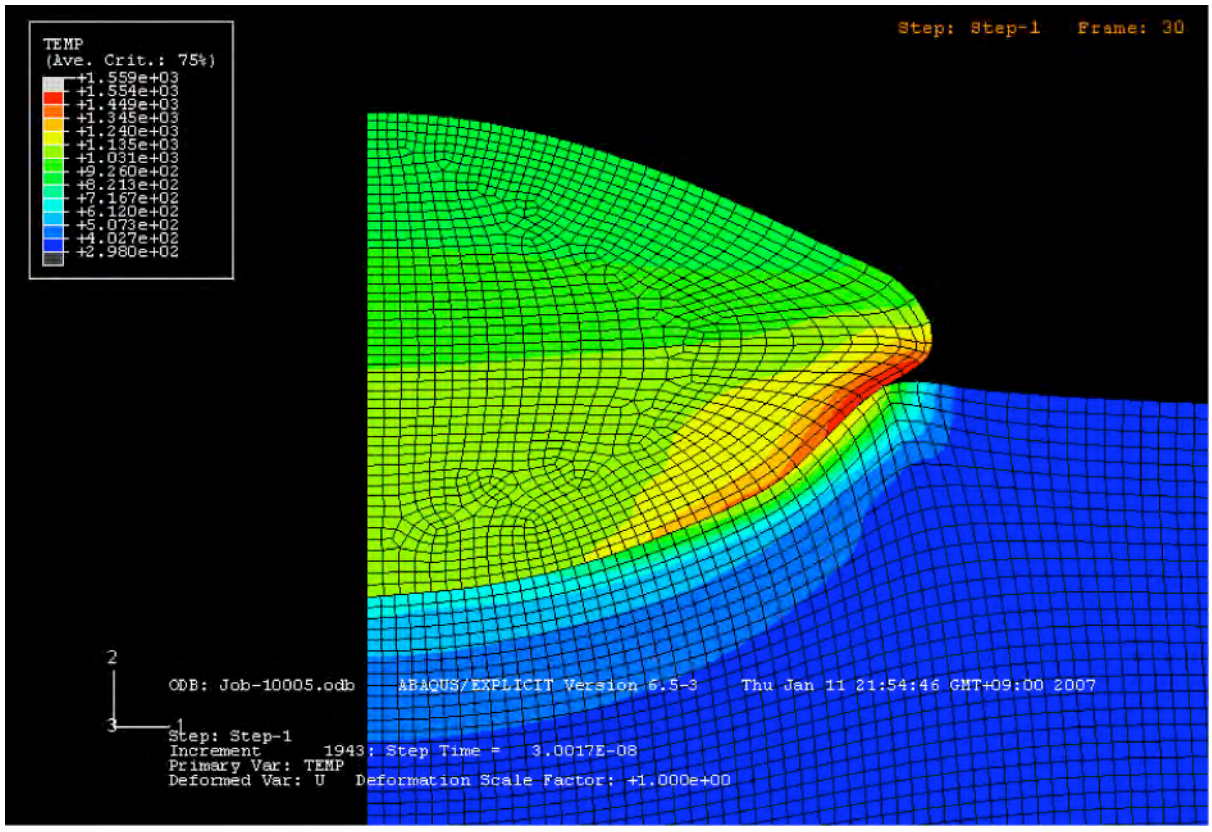

(e-2) Result of temperature distribution (velocity700 m/s)

Fig. 7-3 FEM results for particle impingement.

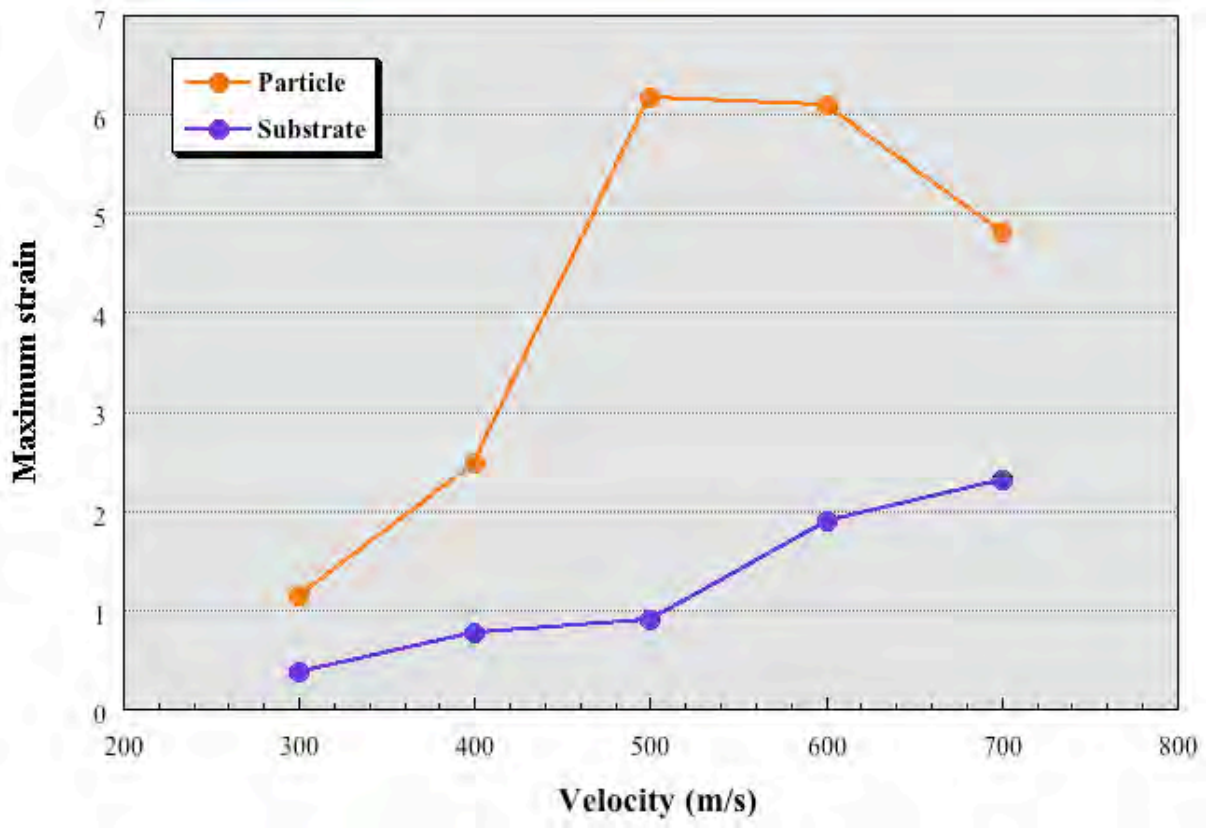

Fig. 7-4 Relationship between maximum strain and impact velocity.

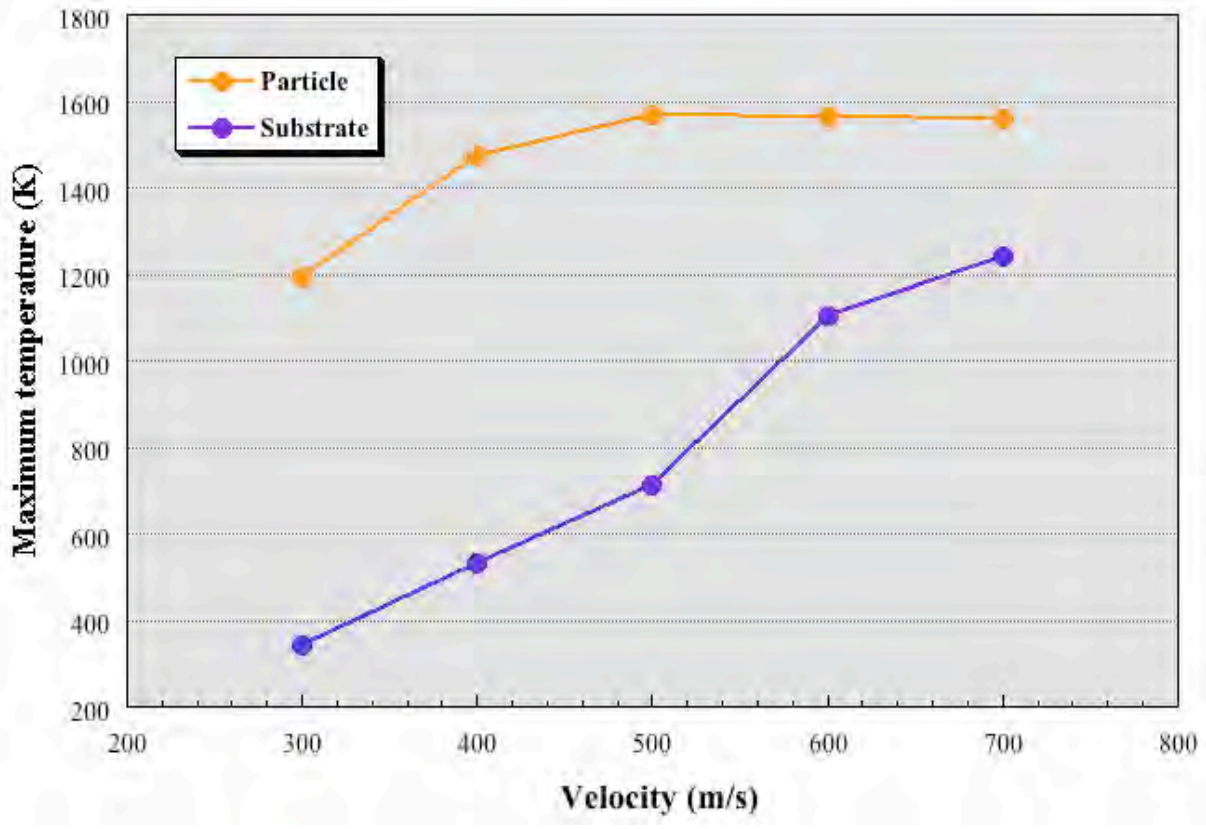

Fig. 7-5 Relationship between impact velocity and maximum temperature.

7.3.2 Estimation of critical velocity using local melting model

Using the initial FEM parameters of this material system (Table 7-5) in Eq. (6-1), the critical velocity was estimated using Assadi's model. The critical velocity obtained using this model was 411.4 m/s.

In this model the dominant condition is the maximum temperature, which exceeds the melting point of the particle. In the simulation, the melting point of the particle was set to 1570K. From Fig. 7-5, when the velocity is set to 411.4 m/s, the maximum temperature is approximately 1570K. Therefore this model equation indicates a good correlation between the melting temperature and impact velocity. However, this model does not mention the particle deformation behavior.

7.3.3 Simulation results of dimensions of deposited particle and substrate

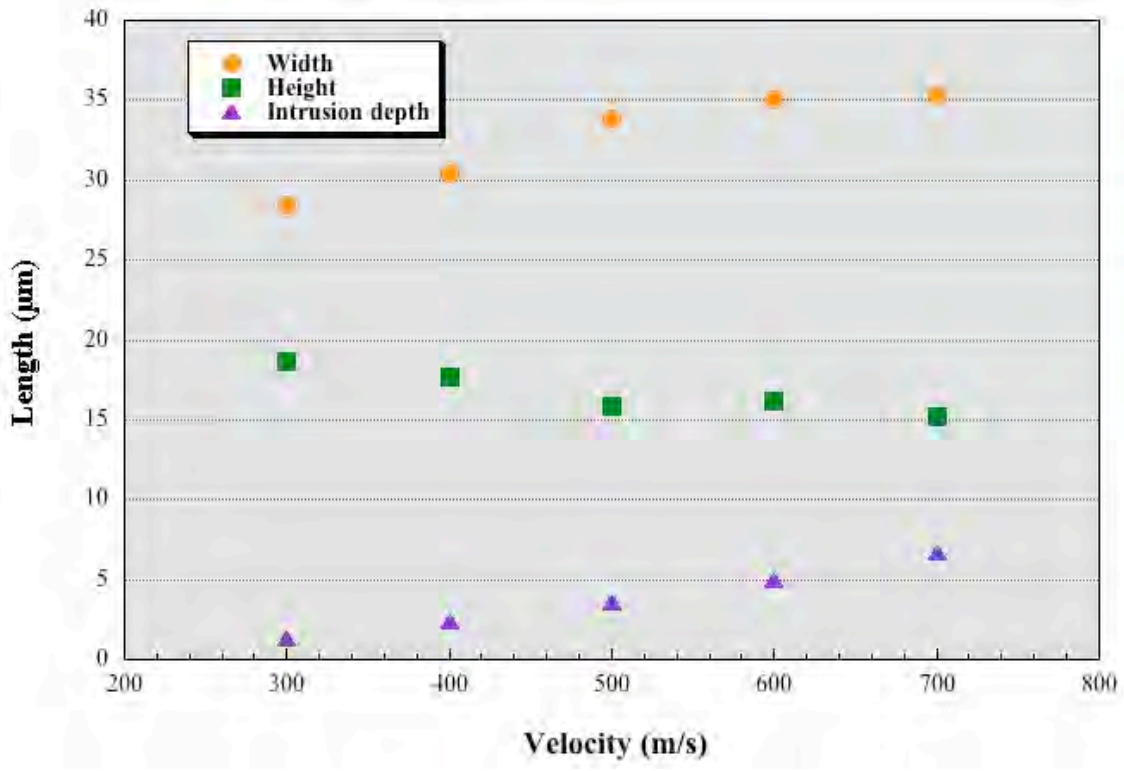

Fig. 7-6 The velocity dependence of deformation obtained from the FEM simulation.

Figure 7-6 shows the deformed particle geometries, which were described by the parameters defined above. These parameters change in proportion to the velocity. In particular, the increasing intrusion depth had a linear dependence on the velocity. This tendency indicates that the higher impingement velocity causes deeper particle intrusion into the substrate. It was difficult to estimate the initial dimensions of the particles from the deformed particle measurements. Consequently, a ratio of the intrusion depth and width, a ratio of intrusion depth and height, and a ratio of height and width were plotted in Fig. 7-7.

Figure 7-7 indicates that the ratio of intrusion depth and width, and ratio of intrusion depth and height increased linearly with the velocity. The approximate formulas are shown on this graph. In other words, using the dimensional ratio and these formulas allow estimation of the impact velocity as converted into values for a 25μm diameter particle.

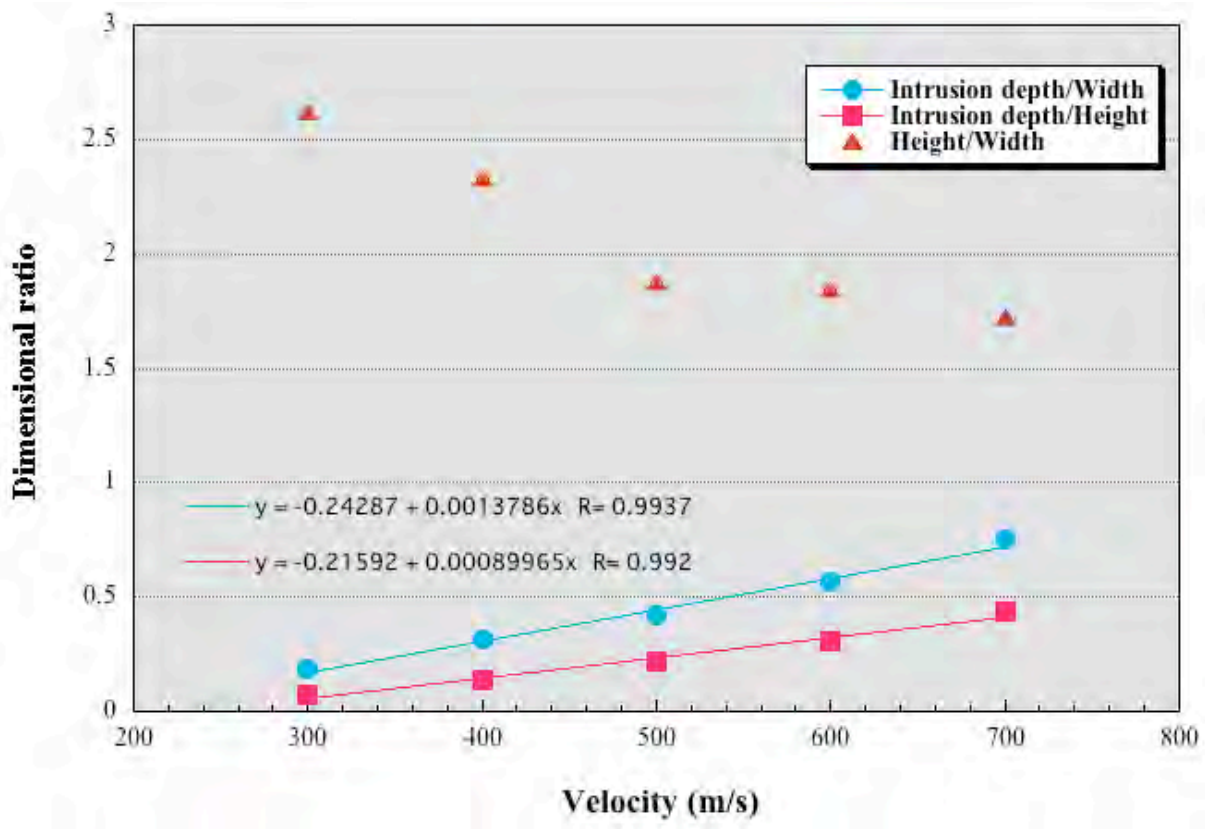

Fig. 7-7 Dimensional ratio and impact velocity.

7.3.4 Critical conditions of deposition

Figure 7-8 shows a measured particle and its geometry. The left-hand side of the particle has good deposition but the right side does not. The reason for this difference is that the particle has no impact in the perpendicular direction. As mentioned in Chapter 2, this particle has impinged from the upper right to the bottom left direction. Therefore, the impact deformation is not symmetrical and the left side has stronger deformation.

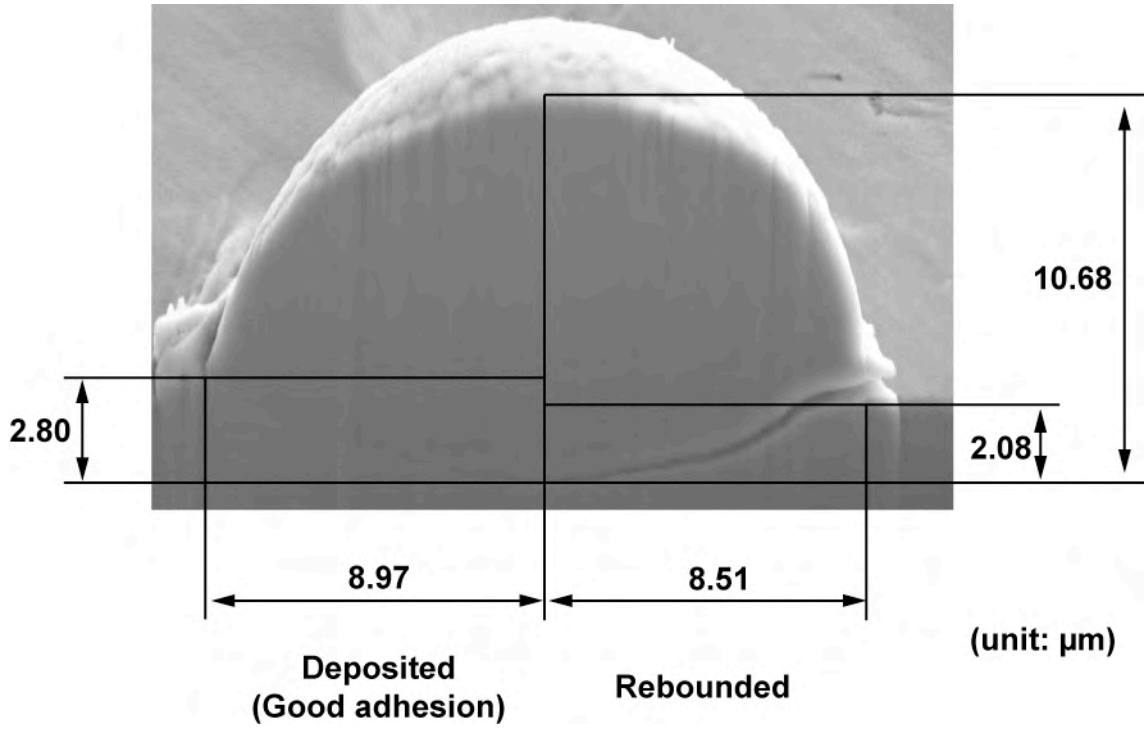

Fig. 7-8 Example of measurement of a deposited particle.

As mentioned above, from the dimensional parameters it is possible to estimate the impact velocity as converted to 25μm diameter particle. The dimensional parameters, such as the intrusion depth and width and intrusion depth /height, are important for studying the deposition threshold.

The measured dimensional ratio parameters of intrusion depth/width and intrusion depth/height were shown in Figs. 7-9 and 10 respectively. In these plots, the red marks indicate the ratio of the rebounded, i.e. non-deposited particles, and the blue marks indicate particles with good adhesion. In both plot, there is the threshold of the deposit and rebound ratio. The deposited particles are more severely deformed.

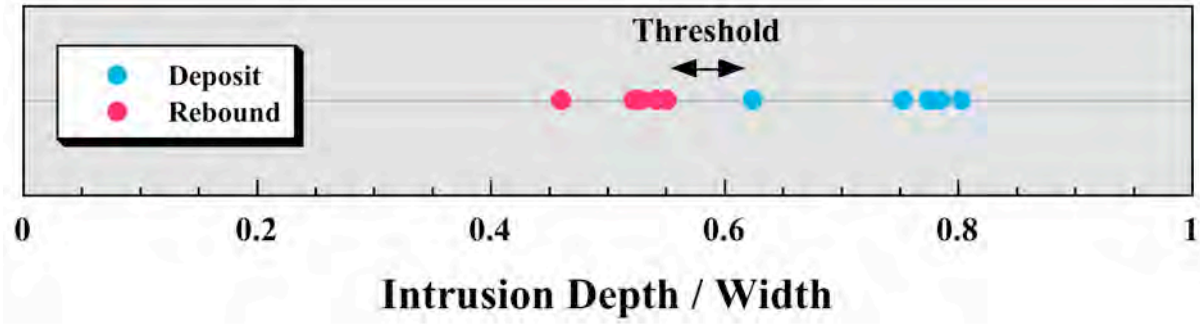

Fig. 7-9 Intrusion ratio of the depth and width tendency and deposition threshold.

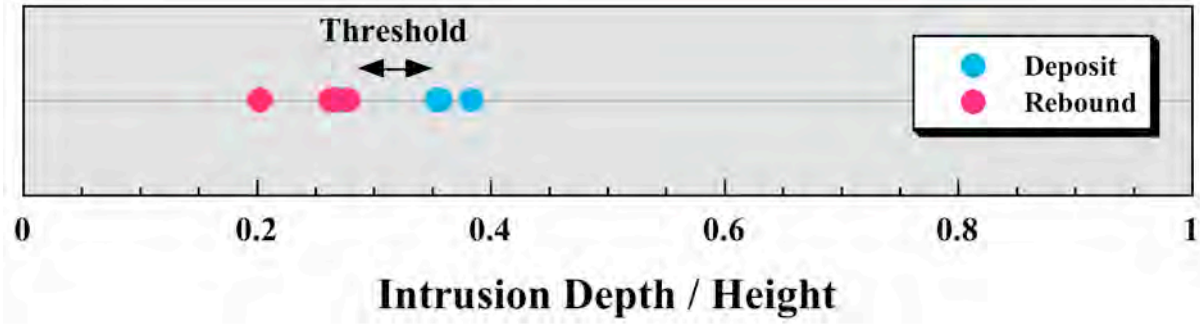

Fig. 7-10 Intrusion ratio of the depth and height tendency and deposition threshold.

There is a linear relation between these ratios and the estimated impact velocity. Using the approximation formulas in Fig. 7-7, the critical velocity condition was re-defined as follows:

$$v_{d25DW} = \frac{R_{DW} + 0.24287}{0.0013786} \tag{7-2}$$

$$v_{d25DH} = \frac{R_{DH} + 0.21592}{0.00089965} \tag{7-3}$$

V_{d25DW}: estimated velocity converted to d=25μm diameter particle calculated from the intrusion depth/width ratio

V_{d25DH}: estimated velocity converted to d=25μm diameter particle calculated from the intrusion depth/height ratio

R_{DW}: intrusion depth/width ratio

R_{DH}: intrusion depth/height ratio

The estimated results are shown in Table 7-7. From these results, the critical condition, which is indicated by the estimated impact velocity, was in the range of 549 to 633 m/s.

Table 7-7 Estimated results of threshold velocity conditions

	Minimum threshold	Maximum threshold
V_{d25DW}	549 m/s	633 m/s
V_{d25DH}	576 m/s	629 m/s

The estimated velocity threshold was re-indicated in the simulation strain and temperature results in Figs. 7-11 and 12, respectively. In the blue region, defined as the threshold condition, the strain and temperature of the substrate underwent a considerable change. This substrate deformation was the dominant factor of the deposition.

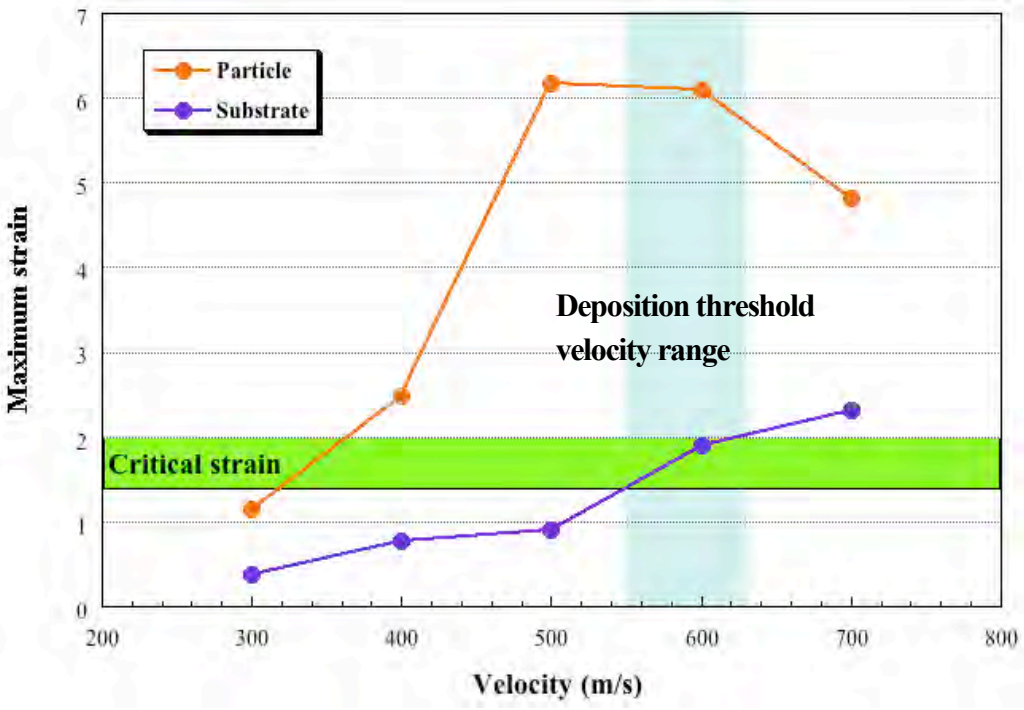

Fig. 7-11 Critical condition and maximum strain.

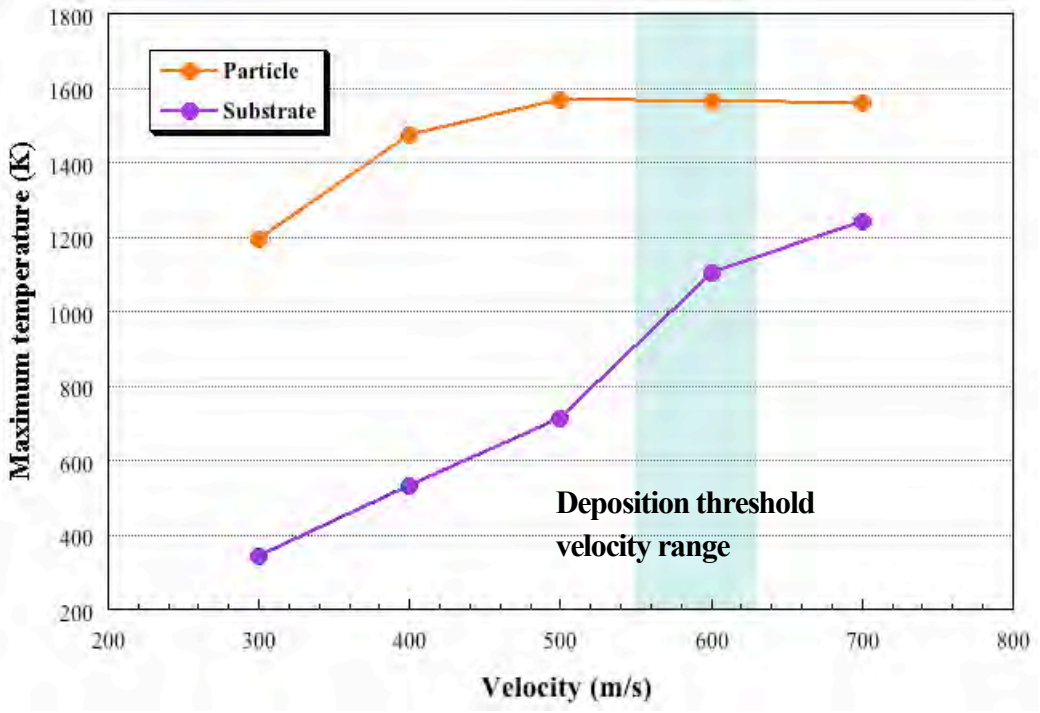

Fig. 7-12 Critical condition and maximum temperature.

7.4 Deposition Mechanisms of Cold-Sprayed Coating

From the results of TEM observations, the deposition mechanism of cold spraying was found to be the necessity to create nascent surfaces and high-pressure contact as shown in Fig. 7-13. In other words, the essential qualification is the creation of nascent surfaces of particle and substrate. From the simulation results, the maximum temperature and maximum strain have a good correlation. However, from the TEM results, melting of the particle at the interface cannot be observed. Therefore the dominant factor is not the maximum temperature. We suggest that the strain of particle and substrate are much more important.

From the results of Fig. 7-11, it is more difficult to deform the substrate than the particle. Therefore, the dominant factor is the maximum plastic strain of the substrate. In other words, when the substrate is deformed over and above the strain threshold, the particle has already deformed more than of the substrate and already created a sufficient nascent.

The strain threshold for nascent surface creation depends on the materials. In the case of this study, approximately 200% strain of the substrate is the threshold of creation of nascent surface.

Finally, the dominant factor of the deposition was the maximum plastic strain of the substrate. Some researchers have stated that the deposit threshold was related to critical velocity. However the critical velocity explains only the effect of particle temperature increasing. The cold spray deposition mechanism is fundamentally related to the strain of the substrate, so we should focus on the strain of substrate to discuss the cold spray deposition mechanism.

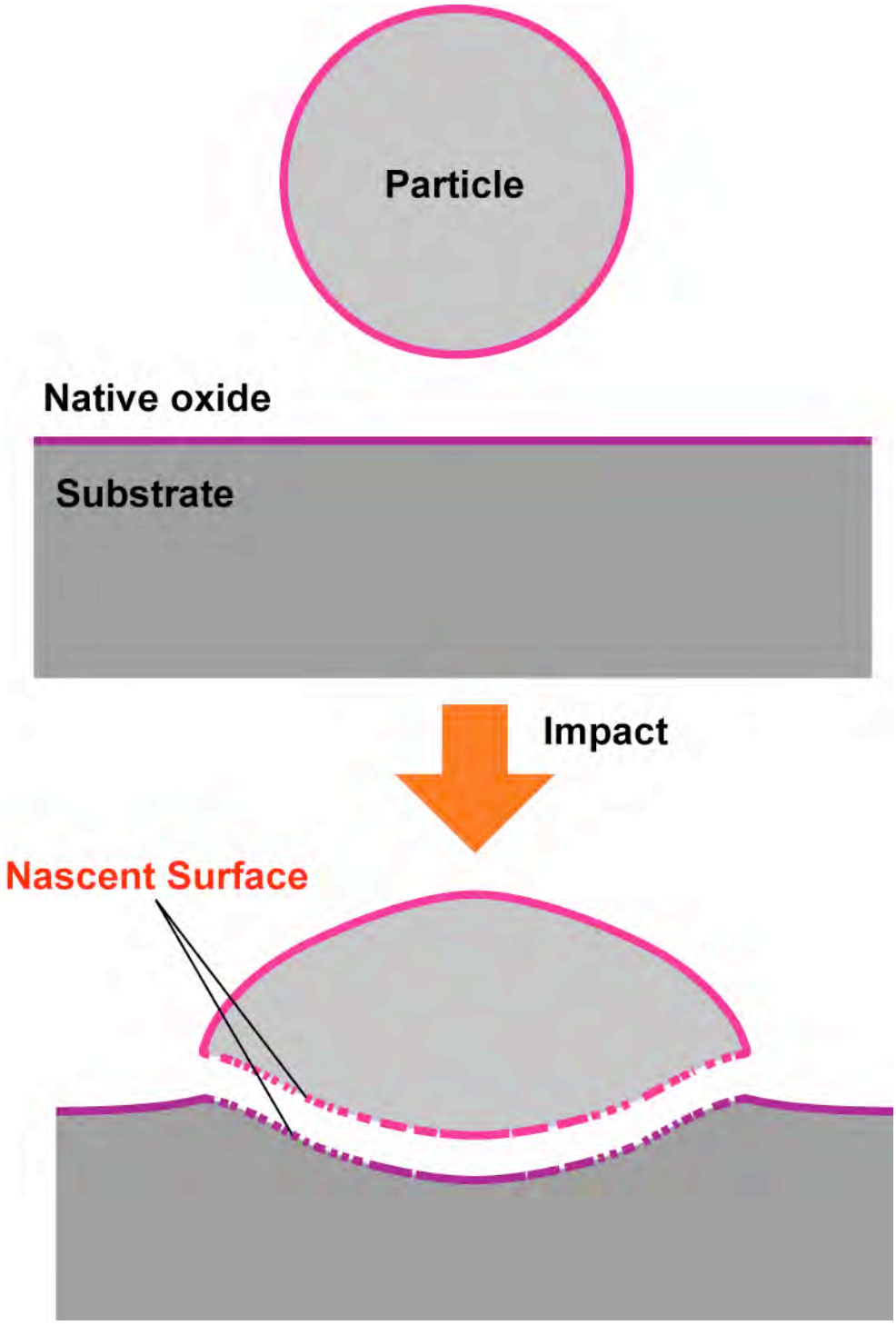

Fig. 7-13 Schematic illustrations of nascent surface creation during cold spray impact.

References

[7-1] H. Assadi, F. Gartner, T. Stoletenhoff, and H. Kreye: Bonding Mechnism inn Cold Gas Spraying, Acta Matelia, 51 (2003) pp.4379-4394.

[7-2] R. Sievert, H.-D. Noack, A. Hamann, P. Löwe, K.N. Singh, G. Künecke, R. Clos, U. Schreppel, P. Veit, E. Uhlmann, R. Zettier: Simulation der Spansegmentierung beim Hochgeschwindigkeits-Zerspanen unter Beru cksichtigung duktiler Schadigung, Technische Mechanik, Band 23, Heft 2-4, (2003) pp. 216-233. (in German)

[7-3] J. Michael Pereira, Bradley A. Lerch: Effects of heat treatment on the ballistic impact properties of INCONEL 718 for jet engine fan containment applications", International Journal of Impact Engineering 25, (2001) pp. 715–733.

[7-4] K. Yokoyama, M. Watanabe, S, Kuroda, Y. Gotoh, O, Schmidt and T. Gartner, Simulation of Solid Particle Impact Behavior for Spray Processes,Materials Transactions. V 47 2006 pp1697-1702.

[7-5] Hamid Assadi, Frank Gartner, Thorsten Stoltenhoff, and Heinrich Kreye: Bonding mechanism in cold gas spraying, Acta Materialia 51 (2003) pp.4379–4394.

[7-6] Tobias Schmidt, Frank Gartner, Hamid Assadi, and Heinrich Kreye: Development of a generalized parameter window for cold spray deposition, Acta Materialia 54 (2006) pp.729–742.

8 Conclusions

In order to elucidate the deposition mechanism of cold-sprayed MCrAlY coatings, this study focused on the nano-structure and several investigations were carried out.

From experimental approaches such as TEM analyses and LASER FLEX, the deposition interface was found to exhibit no evidence of melting. Instead, the nascent surface contact was found to be the most important factor influencing the deposition mechanism. Therefore, the dominant deposition parameter is considered to be the creation of the nascent surfaces of particle and substrate.

Using the FEM approach, the particle and substrate deformation was simulated. Comparing the FEM analysis results and particle cross-sectional observation, the deformation behavior, such as the maximum plastic strain, has a correlation with the impingement behavior. Creation of sufficient nascent surface is a necessary factor for deposition. In order to satisfy these conditions, particle and substrate should exceed the critical strain. In the case of this material system, particles and substrates have similar mechanical properties. Therefore, the plastic deformation behavior of both materials is similar. However, since the substrate is much larger than the particles, the maximum strain of the substrate is smaller than that of the particles. In other words, the substrate is more resistant to deformation. Therefore the dominant factor is whether the maximum plastic strain of the particle is higher than the critical strain necessary for sufficient nascent surface creation.

From this knowledge, the critical deposition parameter is considered to be the critical maximum plastic strain of the substrate. In this material system, approximately 200 % substrate strain is the critical condition of deposition. Therefore, the conventional critical velocity is explained only as a function of the strain. In summary, the strain is the most important factor in cold spraying.

The conclusions of the present work can be summarized as follows:

Chapter 2 considers the influence of several parameters, such as the powder feed rate tendency and gas temperature. In addition, the deposition efficiency of cold-sprayed coatings obtained using a sparsely particle deposited specimen was discussed. The following conclusions were drawn:

- From the results of the estimation of particle velocity, nitrogen was selected to be the working gas for CoNiCrAlY cold spraying.
- The cold spray system used (CGT, KINETIKS 3000) is capable of supplying the stabilized CoNiCrAlY powder

- Increasing the gas temperature results in enhancement of the spray efficiency.
- When using nitrogen gas at 600 ºC, the calculated particle deposition efficiency was 83.9 %. This condition allows a dense cold-sprayed CoNiCrAlY coating to be obtained.

In chapter 3, in order to determine the mechanical properties of coatings and characterize the cold spray coatings, porosity measurements and hardness tests were carried out. In addition, in order to obtain an understanding of high-temperature oxidation behavior of cold-sprayed CoNiCrAlY coatings, high-temperature exposure tests were carried out. The main results obtained from this chapter can be summarized as follows:

- From the results of the porosity measurements, the coating density of the cold-sprayed CoNiCrAlY coating is greater than that of the low-pressure plasma-sprayed coating.
- From the results of the hardness tests on the cold-sprayed coating, one can conclude that the hardness tendency is not influenced by the distance from the interface. The hardness distribution range of the cold-sprayed coating was narrower than that of the low-pressure plasma sprayed coatings.
- The results of EDX analyses on specimens exposed to high temperature showed that the spray method has negligible effects on the Co diffusion depth and tendency during high-temperature operation.
- From the results of EDX elemental mapping of the TGO layer of coatings exposed to high temperature for 100 hours, cold-sprayed MCrAlY coatings have a lower oxidation ratio rather than low-pressure plasma sprayed coating in this environment, as the cold-sprayed coating is denser than the low-pressure plasma sprayed coating. Therefore, the cold-sprayed coating technique improves the high temperature oxidation behavior of MCrAlY coatings.

Chapter 4 was an investigation of the particle deposition behavior. In order to understand the deposition conditions of an individual impinged particle, which is one of the most important approaches for elucidation of the cold spray mechanism, this chapter considers SEM cross-sectional analyses of deposited particles, which were fabricated by FIB. The main results obtained from this chapter can be summarized as follows:

- A single deposited particle does not have good adhesion but is only partly deposited.
- From the results of analysis of two or three overlapping particles, it is shown that the first particle will have better adhesion when it is attacked by the other particles than when it is not followed by any other particles. The impact of other particles on the first particle will result in closure of the open interface. Therefore, follow-on particles can improve the adhesion force at the interface.

- In actual cold spraying, particle-impingement phenomena such as the direction, velocity, particle size, etc. were much more complicated. In particular, multiple impingement can improve the adhesion force at the interface between particle and substrate. This complicated multiple impingement gives good adhesion in the cold spray coatings.

In chapter 5, in order to elucidate the mechanisms of deposition by cold spraying, TEM and STEM observation and micro-EDX elementary analyses were carried out. Nano-beam diffraction was used to analyze the orientation relationship between the contacting grains of coating and substrate. The main results obtained from this chapter can be summarized as follows:

- From the STEM analysis results, a decrease in Al content was observed at earlier position compared to the decrease in Co. Thus, it was concluded that Al was depleted at the interface. The Al-depleted phase is considered to be the γ/γ'-(Ni/Ni3Al) phase of CoNiCrAlY. The decrease in this region may be attributed to the contact, which occurred in matrix phase of CoNiCrAlY in this observation. From the results of TEM analyses, grain size miniaturization was observed. This was caused by the high-speed plastic deformation during the cold spraying process.
- There is an oxide film in between the substrate and the coating, as seen from the results of TEM analyses. However, this film is not always observed, and usually the coating and substrate grains overlap at these positions. More specifically, intermittent adhesion between coating and substrate occurred at these interfaces.
- From the TEM nano-beam diffraction (NBD) patterns, the two grains in contact have orientations relationship of (311) in Ni3Al and (1-11) in γ-Ni; this is not the best bonding condition. This combination, however, has as good an adhesion at grain boundaries. Moreover there is no evidence of melting of substrate and particles; the actual bonding of cold-sprayed coating and substrate occurred at the contact areas of nascent surfaces.

Chapter 6 discusses an approach to simulation of the cold spray phenomenon. Different kinds of Laser Shock Flier Experiments (LASER-FLEX) were carried out. The main results obtained from this chapter can be summarized as follows:

- From the results of LASER-FLEX that used CoNiCrAlY foil, the deformation rates were extremely large. The interface between the matrix region and the substrate is not clear, but the interface between the precipitated region and substrate is clear in this image. The local temperature at the interface may be increased and hence the matrix phase be melted. However these phenomena were not observed in the actual cold spraying and LASER-FLEX tests using powder.

- Even though the flier and particle impinged at the same velocity, the adhesion behavior of the two were different therefore the impulse of the attached material must be an important aspect of deposition. The LASER-FLEX technique using powder appears to be a good way to simulate actual cold spray deposition.
- From the results of particles impinged at 700 m/s, the interface between particle and substrate does not have complete deposition. Therefore the critical velocity of 24 μm CoNiCrAlY powder on INCONEL substrate must be more than 700 m/s.

From the results of TEM observation, the deposition mechanism of cold spray was found to require the creation of nascent surfaces and high-pressure contact. In other words, an essential qualification is the creation of nascent surfaces on particle and substrate. From the simulation results, the maximum temperature and maximum strain have a good correlation. However, from the TEM results, melting of the particle at the interface is not observed. Therefore the dominant factor is not the maximum temperature. We suggest that the strain of particle and substrate is much more important.

From the results of FEM simulation, it is more difficult to deform the substrate than the particle. Therefore, the dominant factor is the maximum plastic strain of substrate. In other words, if the substrate is deformed beyond the strain threshold, the particle has already deformed more than the substrate and already created sufficient nascent surface.

The strain threshold for nascent surface creation depends on the materials. In this study, approximately 200% strain of the substrate is the threshold for creation of nascent surface.

In summary, the dominant factor in deposition was the substrate strain. Some researchers have stated that the deposit threshold was dependent on critical velocity. However, the critical velocity can be explained as a function of strain and temperature, and the cold spray deposition mechanism can be more fundamentally considered as depending on the strain of the substrate. Therefore we should focus on the strain of substrate to discuss the mechanism of cold spray deposition.

ACKNOWLEDGEMENTS

The author would like to thank Associate Vice President of Tohoku University, Dr. Tetsuo Shoji for his support and guidance throughout this study and my research life.

I express my deep sense of gratitude to Associate Professor Kazuhiro Ogawa for his untiring support and enthusiastic guidance throughout this study. His patient care and encouragement have always been a source of inspiration.

The kind help and insightful advice of Professor Hideo Miura is also greatly appreciated. I would like to express my thanks to thesis adviser Professor Tsunemoto Kuriyagawa.

I would like to express my heartfelt thanks to Dr. Michel Jeandin, Director of C2P, Centre des Materiaux, Ecole des Mines de Paris. His irreplaceable technical advice and his scintillating character make my research life fruitful in France.

I would like to express my thanks to Professor Toshiyuki Hashida, Professor Akio Ohji, Visiting Professor Toshio Yonezawa and Dr. Tatsuo Kondo for continuous encouragement

I would like to express my appreciate to Dr. Sophie Barradas, Mr. François Borit, Ms. Nicole de Dave-Fabregue, Dr. Vincent Guipont, Dr. Michel Boustie, Mr. Kazuhiko Sakaguchi, Dr. Hiromichi Miyazaki, Mr. Kiyohiro Ito and Mr. Kenji Ichimura, Dr. Victoria Yardley and Mr. Sayar Medhi who supported the experiments and edit my thesis.

I am grateful for support of this work and for my graceful life in France by Ms. Mélissa Delqué, Mr. Olivier Amsellem, Mr. Dimitris Christoulis, Mr. Tolga Tavsanoglu and Ms. Yoko Inagaki,

I would like to express my heartfelt thanks to Associate Professor Zanpeng Lu, Research Associate Yo-ich Takeda, Mr. Masatoshi Suzuki, Dr. Jerome Isselin, Dr. Seo Dowon, Dr. Yasumoto Sato, Dr. He Xue, Dr. Yuzuru ITO, Mr. Masatoshi, Tanno, Mr. Ismail Tirtom, Mr. Takahiro Niki, and Mr. Nishith Kumar Das.

It is a pleasure to thank every member of the Fracture and Reliability Research Institute, Tohoku University and Centre des Materiaux, Ecole des Mines de Paris.

I wish to express my special gratitude to secretary Ms. Masayo Abe, Ms. Ayako Kitada, Ms. Tomoka Tsuda, Ms. Kuniko Tadaki, Ms. Hiroe Miyajima and Ms. Tomomi Shikoda for them hospitality and warm affection. Their affable management and abundant advice have greatly helped me in many areas.

Finally, I would love to thank my family, my Father and Mother. I would not be here at this moment without them. I would like to thank so many people who have supported and encouraged me during my work and in life on the whole.

16th January, 2006

Yuji Ichikawa